Flexible MEMS Skin Technology for Distributed Fluidic Sensing

Thesis by

Yong Xu

In Partial Fulfillment of the Requirements
for the Degree of Doctor of Philosophy

California Institute of Technology
Pasadena, California, USA
2002

To my parents,
my wife, and my son

Acknowledgements

First, I would like to thank my advisor, Dr. Yu-Chong Tai, for offering me the chance to explore the exciting and fantastic field of MEMS and giving me constant guidance and encouragement far beyond research.

I would also like to express my gratitude to Dr. Fukang Jiang, who taught me almost everything about micromachining when I first entered the clean room and gave me tremendous help in the past five years. My thanks also go to Dr. Chih-Ming Ho at UCLA for his guidance in my research. I thank Adam Huang at UCLA for his help in the wind tunnel test.

I am grateful to many previous members of our group, especially Dr. Tom Tsao, Dr. Shuyun Wu, Dr. Xing Yang, Dr. Wen Hsieh, Dr. Xuan-Qi Wang, Dr. Charles Grosjean, Mr. Ken Walsh, Mr. Tianxiang Weng, Dr. Nick Pornsinsirirak, and Dr. Qiao Lin. From them I received numerous help which is impossible to list here. In particular, I am grateful to Zhigang Han, not only for his help in research but also for his friendship, which was very important for me to get through the hard time when I first came to this country.

I am obligated to thank the current members in our group. My gratitude goes to Ellis Meng for her help in proofreading my papers and thesis. Same gratitude goes to Matthieu Liger, Justin Boland and his wife, and Ted Harder. I would like to thank Qing He and his wife for sharing their optimism and happiness with me. I am indebted to Jun Xie, who not only provides me assistance in research but also allows me to enjoy his cuisine skills. His kindness and encouragement are highly appreciated.

My thanks also go to our technician, Mr. Trevor Roper, who knows almost every trick about our equipment. Without his help my research can not be finished in time. I want to thank our secretary Tanya Owen for her assistance in lab administration. I would also like to thank Mr. Chen-Wei Chiu in Umachines, and Dr. Weilong Tang in IMMI, for their help in my research.

I will never forget the help and support I received from my friend, Hongyu Yu, during the most difficult moment in my life. Without the help from Hongyu Yu and Jun Xie, I can not imagine how I got through those dark days. They are willing to offer help whenever I need it.

Words can not describe my appreciation for my parents. Without their sacrifice, patience, and support, I would have never reached where I am now. Finally, I would like to thank my wife, who I am so lucky to be married to. Her support and encouragement are the constant source of power for me to face any challenge.

Flexible MEMS Skin Technology for Distributed Fluidic Sensing

Thesis by
Yong Xu

In Partial Fulfillment of the Requirements
for the Degree of
Doctor of Philosophy

Abstract

Inherently, most MEMS devices are fabricated on rigid substrates. However, for a wide variety of applications, it has long been desirable that sensors, actuators, or circuits can be fabricated on flexible substrates so as to be mounted on nonplanar surfaces or even on flexible objects such as a human body. A novel flexible skin technology, which is compatible with MEMS and ICs processes, was developed in the Caltech Micromachining Lab for the distributed fluidic sensing.

With this technology, a flexible shear-stress sensor skin was fabricated and successfully implemented on an Unmanned Aerial Vehicle (UAV). The flow separation detection along the leading edge of UAV was demonstrated in both wind tunnel and the real flight test. The complete UAV sensing/computing/controlling system, including microsensors, microelectronics, and microactuators, was also demonstrated in wind tunnel and ready for the flight test.

This technology was further explored by making an underwater shear-stress sensor skin for applications such as flow pattern measurement of radio controlled

submarines, and the study of the safety and arming mechanisms of next generation smart torpedoes. Underwater shear-stress sensor was developed, addressing the challenges of minimization of the pressure crosstalk and waterproof coating. A selective Parylene deposition method was investigated as well to achieve high shear-stress sensitivity and excellent waterproof simultaneously. With the skin structure, the packaging was significantly simplified and improved.

Additionally, MEMS-IC integration is highly desirable since this integration promises to bring very important benefits such as operational improvement, packaging simplification, and cost reduction. For the first time, an IC-integrated flexible shear-stress sensor skin, which has bias and signal conditioning circuitry on-chip, was developed by using post-CMOS MEMS processes. The fluidic sensing on a semi-cylindrical surface with the IC-integrated shear-stress sensor skin was demonstrated in the wind tunnel.

In addition to distributed fluidic sensing, the MEMS skin technology, with the demonstrated capability to be integrated with ICs, can enable many other important applications in biomedicine, wearable microsystems, RF systems, and robotics.

Table of Contents

List of Figures

List of Tables

Chapter 1

Introduction

1.1 Motivation

Numerous miniaturized sensors and actuators have been fabricated since the emergence of micromachining technology, also known as microelectromechanical systems (MEMS) [1, 2], using technologies originally developed for the integrated circuits industry such as photolithography, wet etching, plasma etching, chemical vapor deposition, and so on. Inherently, most MEMS devices are built on rigid substrates such as silicon and glass wafers. However, for a wide variety of applications, it has long been desirable that sensors, actuators, or circuits can be fabricated on flexible substrates so as to be mounted on nonplanar surfaces or even on flexible objects such as a human body.

The first example is the tactile sensor, which is needed for robotics, biomechanics research, clinical evaluations of hand function, and for hand rehabilitation devices [3]. The sensor must be flexible in order to be attached to curved shapes like fingers and arms.

Shown in Figure 1.1 is another example, which is the concept of an implantable visual prosthesis [4]. The visual images captured by the CMOS image sensor are first processed by the neural net and then transmitted into the interior of the eye. The

stimulator chip, which is an electrode array, has to exhibit sufficient planar flexibility to adapt and bend to the retina shape.

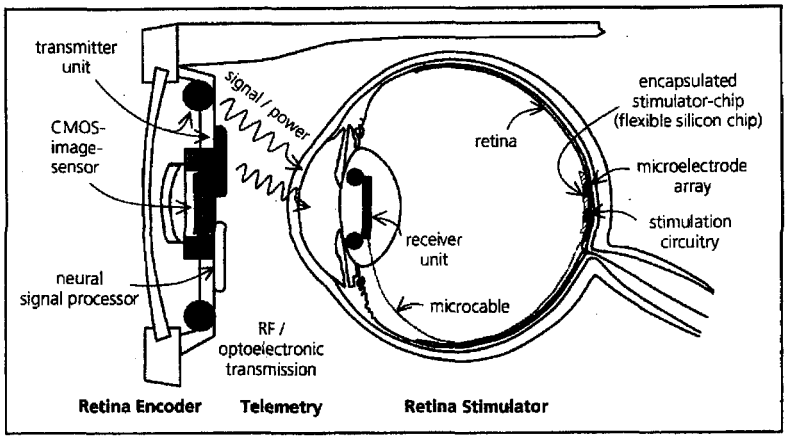

Figure 1.1 The concept of retinal prosthetics [4].

In the field of fluid monitoring and controlling, it is often of great interest to know the profile of certain physical parameters such as temperature, pressure, or shear stress on a nonplanar surface. This distributed fluidic sensing is what we will focus on in this thesis. One project we are working on is to develop an Unmanned Aerial Vehicle (UAV) which is controlled by microsensors, microactuators, and microelectronics (M^3 systems). In order to control the UAV effectively, we need to know the shear stress distribution along the wing's leading edge which is a semicylinder with only half-inch diameter. Therefore, flexible shear-stress sensor arrays are required.

To address the challenges arising from the above applications, we need to develop a technology which can enable the fabrication of micromachined sensors on flexible substrate, namely, a MEMS skin technology. Additionally, integration of circuits on the flexible substrate is highly desirable since this integration promises to bring very important benefits such as operational improvement, packaging simplification, and cost

reduction. Therefore, we need to develop a flexible skin technology which is compatible with both ICs and MEMS.

1.2 Review of flexible skin technology

There are many methods to fabricate flexible miniaturized transducers. The most straightforward one is to fabricate directly on flexible substrate. Actually, similar technology has existed for a long time in the electronics industry, for example, the widely used flexible printed circuitry technology [5] and the thin film transistor (TFT) technology on flexible substrates. It is natural that people adapt this method to fabricate flexible transducers.

In reference [6], a flexible, large area, thin film, position sensitive detector was developed by depositing α-Si:H on Kapton polyimide substrate. The schematic cross section is shown in Figure 1.2. A tin oxide (SnO_2) was first deposited by spray pyrolysis at a temperature of 323°C using a solution of $SnCl_4 \cdot 5H_2O$ dissolved in isopropilic alcohol. The α-Si:H layer was achieved by Plasma-Enhanced Chemical Vapor Deposition (PECVD). Finally the aluminum contacts were deposited by e-beam evaporation.

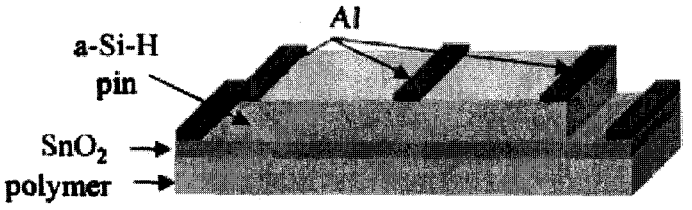

Figure 1.2 A flexible thin-film position-sensitive detector [6].

Most of the sensors made on flexible substrates by direct fabrication are photosensors based on amorphous silicon. Recently, simple MEMS devices on plastic substrates have been demonstrated. For example, in reference [7], the development of amorphous silicon air-gap resonators on plastic substrates were described. The fabrication process is illustrated in Figure 1.3. Photoresist is spin-coated and patterned as the sacrificial layer. Then, structure layers (α-Si:H and aluminum) are deposited and patterned. Finally, the air-gap is released by immersing in a commercial photoresist stripper.

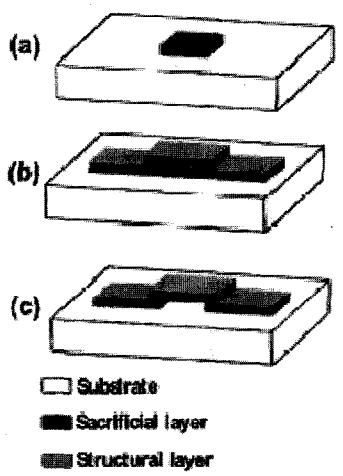

Figure 1.3 Schematic diagram illustrating the fabrication of a surface micromachined bridge structure [7].

Polach at el. [8] developed a matrix of light sensors addressed by α-Si:H TFTs on a flexible plastic substrate. Both the photoconductor and the channel of TFT are formed by hydrogenated amorphous silicon. The common technical challenges, such as the thermal mismatch of the thin films and the substrate, the irreversible shrinkage of the substrate after thermal cycle, the temperature limitation of the substrate during PECVD, are also addressed in this paper. Since the substrate is flexible, one drawback is that very

fine features can not be realized due to the stretch or compression of substrate during the process.

In reference [9], a flexible, light-weight multichannel sieve electrode with integrated cables for interfacing regenerating peripheral nerves was fabricated by a slightly different method. In this case, a silicon wafer is used as a support so that much better dimension control can be achieved. The process begins with polyimide spin coating and curing, followed by other thin film deposition and patterning. At the end of the process, the device is separated manually with forceps. By using a silicon wafer as a carrier, finer features can be achieved and the process can be carried out more conveniently. However, the drawback is also obvious–it is difficult to release the skin from the wafer at the end of the fabrication process.

In order to solve this problem, a sacrificial layer can be added between the polymer and support wafer. The most frequently used sacrificial material is photoresist since it can be readily dissolved by acetone. The process starts with coating photoresist on the wafer as a foundation layer. The drawback of this technology is that the process temperature is limited by the photoresist, e.g., 120°C. Therefore, Parylene is usually chosen as the structure material due to its room temperature deposition process while polyimide is ruled out because of its high curing temperature. Polysilicon can also be used as a sacrificial material with BrF_3 as the etchant. This method overcomes the temperature limit posed by photoresist. However, BrF_3 may attack the polymers such as Parylene if the releasing time is too long. For more details, please refer to Chapter 5 of Pornsinsirirak's thesis [10], where Pornsinsirirak described the advantages and disadvantages of using photoresist and polysilicon as sacrificial material. He concluded

that photoresist was more attractive for his application and described the development of a Parylene MEMS electrostatic actuator skin based on this method.

The direct fabrication on flexible substrates can be summarized in the Figure 1.4. For simplicity, only one device layer is drawn to illustrate the concept. For actual devices, multilayers can be used.

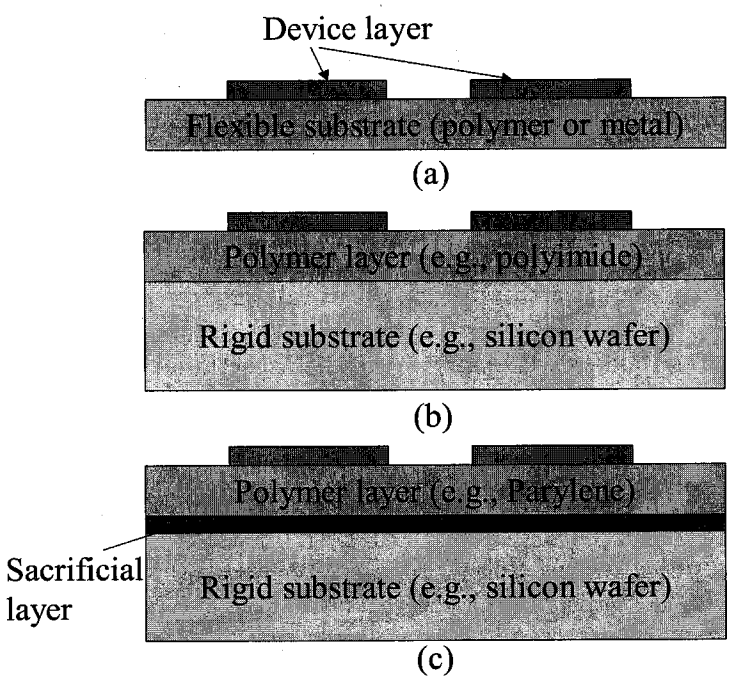

Figure 1.4 Summary of direct fabrications on flexible substrates: (a) simple flexible substrate; (b) use rigid substrate as a support; (c) use sacrificial layer between the polymer layer and rigid substrate.

The advantage of direct fabrication on flexible substrate is that the technology is relatively simple and cheap. Most importantly, large area flexible skin can be fabricated in this way. Sometimes it can even be batch manufactured by roll-to-roll method. For instance, United Solar Systems Corporation developed a unique system that allows photovoltaic solar panels to be manufactured by roll-to-roll process [11]. It operates

much like a newspaper press, speedily imprinting thin film semiconductor layers onto a web of stainless steel substrate. However, the disadvantage is also obvious. First, due to the flexible substrate, the process temperature is limited. A lot of high temperature processes are ruled out and the material properties are not optimized. Moreover, numerous transducers based on silicon and other rigid materials can hardly be transplanted to flexible substrate[1]. Some most frequently used microstructures, such as vacuum cavity, are difficult to realize. As a consequence, the structures which can be constructed are very limited. Most importantly, this method can rarely utilize the well-developed IC technology in which tremendous money and time have been invested. Circuits based on amorphous silicon are active research topics now. However, it will not catch up with the complexity and performance of circuits based on single crystalline silicon in the foreseeable future. In conclusion, the direct fabrication is a limited technology in terms of the devices which can be fabricated.

In the methods discussed above, the flexible substrate only serves as a mechanical support for the devices. There are some other novel technologies where the flexible substrate itself is the function material for sensors and circuits. IBM reported an electronic embroidery technology, which they call e-broidery (also known as e-textile now) [13]. Highly durable, flexible, and even washable multilayer electronic circuitry can be constructed on textile substrates, using conductive yarns and suitably packaged components. For example, Figure 1.5 shows a Firefly Dress. Its major part is a skirt, handmade from two layers of conducting organza (one supplying power and the other

---

[1] It is possible that arrays of discrete rigid devices can be mounted on flexible substrates [12]. However, as the device size scales down or fine spatial resolution is required, this method has many disadvantages.

ground) separated by a layer of nylon netting. Light emitting diodes with fuzzy conductive Velcro™ ends for electrical contacts are placed throughout the netting. When both ends of an LED brush against the power and ground planes, the circuit is complete and the LED lights.

Figure 1.5 Firefly dress based on e-broidery [13].

The Nobel Prize in chemistry in 2000 went to Alan Heeger, Alan MacDiarmid, and Hideki Shirakawa for the discovery and development of electrically conductive polymers. Figure 1.6 shows a bent flexible electronic circuit made of conductive polymers. Flexible sensor skin can also be developed based on conductive polymers.

Figure 1.6 A bent flexible electronic circuit made of conductive polymers (Courtesy of Philips Research).

A totally different approach was first reported by Barth et al. in 1985 [14]. A one-dimensional flexible Si-diode temperature sensor array was demonstrated. Figure 1.7 shows the top view and cross section view of the flexible array. The process begins with the fabrication of p-n diodes on the front side of silicon wafer. After finishing the Au/Cr/W metalization, a layer of polyimide is spun on with adhesion promoter. The polyimide is cured at 350°C and patterned to expose the contact pads. Then the wafer is masked and etched from the backside in a hydrofluoric acid/nitric acid mixture (HNA), forming separate silicon islands. The polyimide layer is not attacked by the acid mixture. Next, another layer polyimide is coated on the backside and cured at 350°C. Finally, the sensor arrays are cut out with a scalpel or scissors. The major leading failure mechanism is identified as the breakage of the thin silicon on the island periphery.

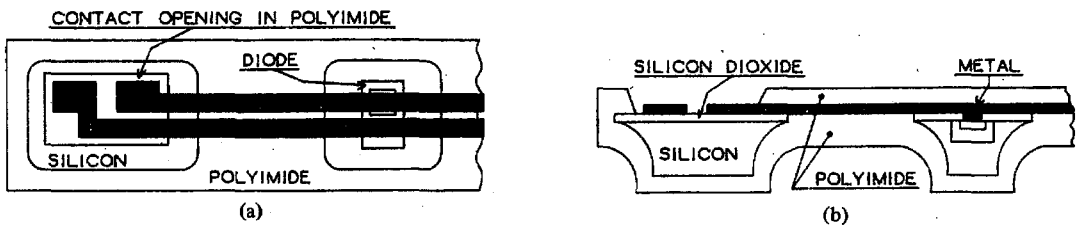

Figure 1.7 The top view and cross section view of the flexible Si-diode temperature sensor array [14].

This idea was further explored by Beebe and Denton in 1994 [15]. Figure 1.8 shows the simplified fabrication process. The silicon islands did not contain any actual sensors since the main purpose was to investigate the package durability. The wafer is cleaned and a thin chromium (Cr) adhesion layer is sputtered on both sides of the wafer. Next polyimide is spin-coated and cured at 400 °C on both sides. The lead metal (Al) is then sputtered and patterned. Another layer of polyimide is applied and vias are opened with O_2 plasma. To prepare the backside for the isotropic etch, the backside polyimide is also patterned in O2 plasma and the underlying Cr is removed. After the lead wires are attached using silver epoxy and protected by another insulating epoxy, the backside is isotropically etched in HNA. Compared with Barth's design, this one has a layer of polyimide between the lead and the silicon. Therefore the lead metal is protected from the sharp silicon edges. However, the durability test confirms that the silicon/polyimide region is still a vulnerable point.

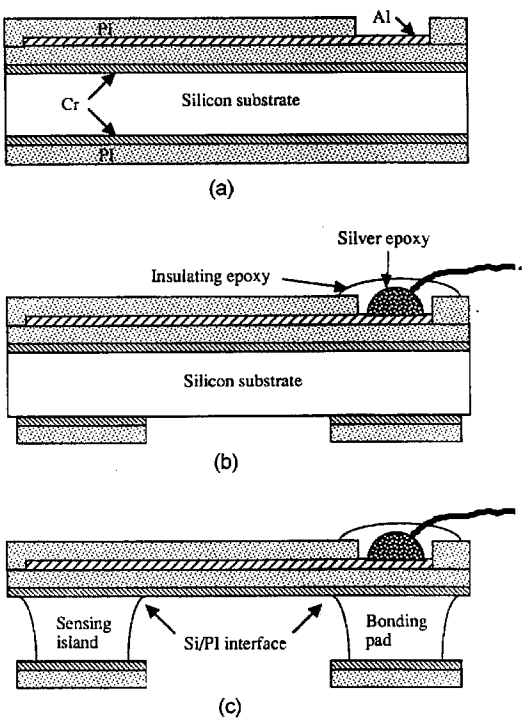

Figure 1.8 Cross sections throughout the fabrication process: (a) after deposition of all metal and polyimide (PI) layers; (b) after attachment of lead wires with silver epoxy and patterning of mask layers for isotropic etch; (c) after the isotropic etch removes unwanted silicon to realizing sensing islands and bonding pads [15].

Based on this process, Beebe et al. reported a flexible tactile sensor that can be mounted on fingers as shown in Figure 1.9 [3].

Figure 1.9 The thumb-mounted tactile sensor [3].

As mentioned above, the main lead failure mechanism on the flexible structures made by Barth and Beebe is the breakage of the thin peripheries on the silicon islands during squeezing and folding test. When examining their process flows, it is obvious that the thin and weak silicon island periphery is the natural result of isotropic HNA etching. The island would be more robust if it were formed by anisotropic etchants, such as TMAH or KOH, or Deep Reactive Ion Etching (DRIE). Based on this idea, a new flexible skin technology that is compatible with both IC and MEMS fabrications was developed in the Caltech Micromachining lab. The concept of this new technology is depicted in Figure 1.10. Assume the MEMS devices and ICs have already been fabricated on the silicon substrate. Then the first step is to spin and pattern polyimide on the front side of the wafer. After this, thin down and etch through the silicon wafer from backside to form the arrays of silicon islands by DRIE. Finally, spin-coat another layer of polyimide from backside to encapsulate the silicon islands. The skin made by this method is much more robust due to the elimination of the weak silicon periphery using anisotropic etching.

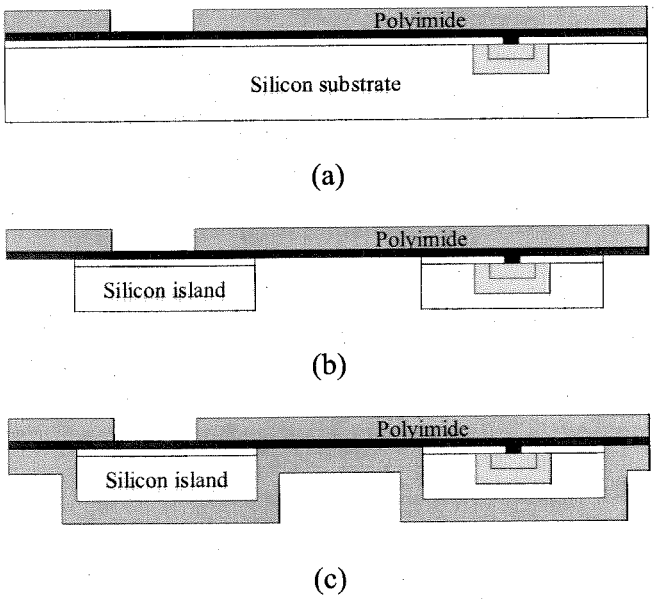

Figure 1.10 Simplified process flow of the new flexible skin technology: (a) spin-coat and pattern polyimide on front side; (b) thin down and etch through the wafer from back side anisotropically to form the silicon islands; (c) spin-coat another layer of polyimide on back side to encapsulate the silicon islands.

The basic structure of the smart skin is arrays of silicon islands sandwiched by two layers of polymer. The biggest advantage of this technology is its compatibility with MEMS and ICs since MEMS devices and ICs can be fabricated on the silicon islands before the formation of skin. However, we cannot take this compatibility as granted. The fabrication process has to be carefully designed to ensure the compatibility. In this thesis, it is demonstrated that fairly complicated MEMS devices can be integrated onto the skin [16]. Furthermore, the MEMS-IC integration on the skin was demonstrated as well [17]. So far the circuits integrated are only fundamental elements such as current mirror, multiplexer, and operational amplifier. However, there is no reason why circuits as

complex as CPU can not be integrated. This integration will ultimately lead to the authentic **smart skin** system.

It is also worth pointing out that the polymer is not limited to polyimide. It can be selected from a wealth of polymers based on the requirements of the specific applications. The rigid substrate is not limited to silicon either. For example, GaAs can also be used to develop flexible RF systems. In one word, this is a very versatile technology.

It is worth noting that the silicon-based flexible skin technology is not always the choice. For the transducers that have very simple structures, such as temperature sensors, electrodes, the direct fabrication on flexible substrate is usually advantageous. Besides those examples mentioned in the beginning of this section, another one is the bubble actuator arrays for the UAV project fabricated on a metal sheet using silicone as membrane material [18]. Figure 1.11 shows the simplified fabrication process and Figure 1.12 shows the actuator skin bonded to a tube. It is very interesting to note that two skin fabrication technologies are employed in the UAV project.

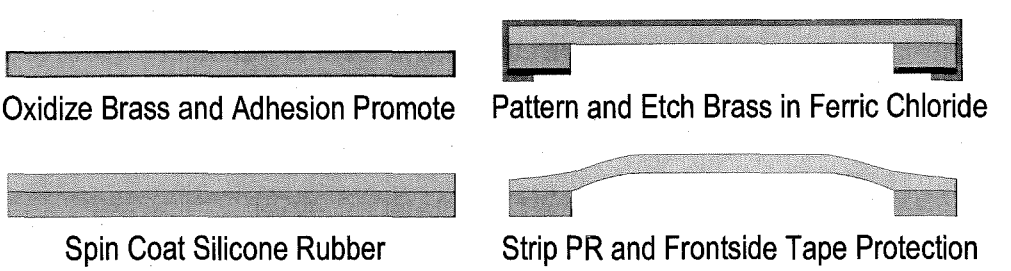

Figure 1.11 Simple process for metal substrate balloon actuators [18].

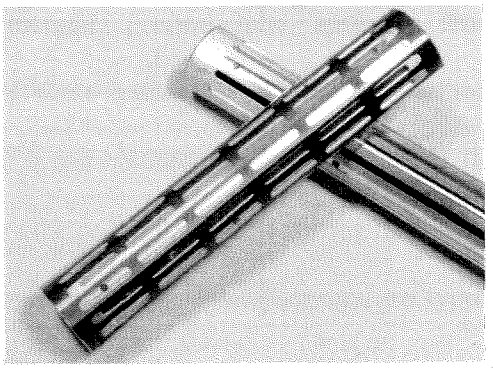

Figure 1.12 Metal substrate actuator skin bonded to a tube [18].

1.3 The micromachined thermal shear-stress sensor

This thesis will focus on distributed fluidic sensing, more specifically, the sensing of shear stress. Accordingly, an introduction on the micromachined thermal shear-stress sensor will be presented here.

When a fluid flows past a boundary, it experiences both normal and tangential stresses. Normal stresses or pressures are readily measured by connecting small holes on the surface to a pressure sensor. The measurement of the tangential or shear stresses is much more difficult. However, the wall shear-stress measurement is of crucial importance for a lot of fluid dynamic monitoring/diagnostics applications, such as flow separation detection for an unmanned aerial vehicle [16] and active drag reduction [19, 20]. Intuitively, the shear stress can be determined directly by measuring the force exerted on a small surface area. The micromachined versions of direct measurement have been realized by using floating elements [21, 22]. The wall shear stress can be determined from the displacement of the floating element or the force it experiences. Other indirect methods developed so far to measure the local wall shear stress include

Stanton tube, thermal method, Preston tube, sublayer fence, and electrochemical technique [23]. Among all these approaches, the thermal method is most often used since it has the advantages that it can be used in a wide variety of flows, it does not interfere with the flow, and it offers the possibility of measuring time-varying flows.

The conventional thermal shear-stress sensors are typically made by depositing thin metal film resistors, mostly platinum or nickel, on flat substrates. During operation, the resistor is electrically heated up, while the fluid flowing over cools it down. The input power of the resistor will change with the wall shear stress from the ambient flow field and this change can be readily detected electronically. The power is dissipated in two ways: conduction loss to substrate and convection loss to the fluid[2]. In order to increase the sensitivity and reduce the power consumption, we want most of the heat to be transferred to the fluid by convections. Namely, it is desirable to minimize the heat loss to substrate. With the emerging micromachining technology, a novel thermal shear-stress sensor has been developed in our group [24]. As shown in Figure 1.13, the basic structure of the sensor is a polysilicon resistor (sensing element) sitting on a nitride diaphragm with a vacuum cavity underneath, which provides excellent thermal isolation to reduce the heat loss to substrate.

[2] The radiation loss is negligible in typical operating temperature.

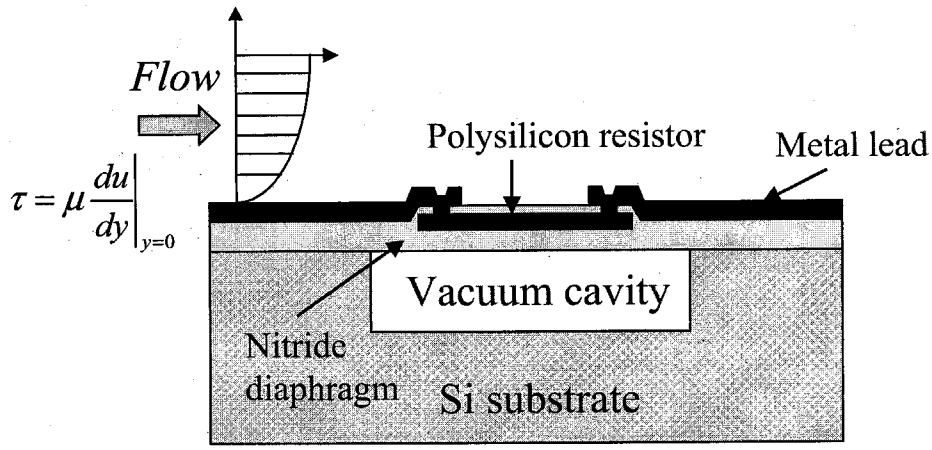

Figure 1.13 The cross section of the micromachined thermal shear-stress sensor.

The details about the design and the fabrication will be discussed in the following chapters. Here we focus on the operation of this thermal shear-stress sensor. The basic operation principle can also be illustrated by Figure 1.13. During operation, the polysilicon resistor is electronically heated up. The input power of the resistor is a function of the wall shear stress (τ) of the ambient fluid, which is defined by

$$\tau = \mu \left.\frac{dU}{dy}\right|_{y=0}, \tag{1.1}$$

where μ is the fluid's viscosity, U is the streamwise velocity, and y is normal to and originates at the sensor surface. The relationship between τ and the input power P to the sensor is typically described by [23]:

$$P = \frac{V^2}{R_S} = \Delta T(A(\rho\tau)^{1/3} + B), \tag{1.2}$$

where V and R_S are respectively the voltage and resistance of shear stress sensor, ΔT is the average temperature difference between the heated resistor and ambient, $A \propto C_p^{1/3} k_T^{2/3} / \mu^{1/3}$ (C_p and k_T are the heat capacity and thermal conductivity of the fluid,

respectively), ρ is the density of the fluid and term B represents the heat loss at zero shear stress. However, Eq.(1.2) is derived for conventional macro heating element and may not be valid for our micromachined shear-stress sensor [25]. In this case, we use the empirical formula

$$P = \frac{V^2}{R_S} = \Delta T(A_t(\rho\tau)^{1/n} + B_t) \tag{1.3}$$

where A_t, B_t and n are determined experimentally.

The shear-stress sensor can operate in either constant temperature (CT) mode or constant current (CC) mode. When operated in CT mode, the temperature of the sensor remains constant during operation as the name suggests. Figure 1.14 shows the simplified CT biasing circuits, where R_S is the shear-stress sensor, and R_1 is adjustable. R_S, R_1, R_2, and R_3, together with the operational amplifier, form a negative feedback loop which requires that $R_S / R_1 = R_3/R_2$ when steady state is reached. The sensing element, which is heavily boron doped polysilicon, has a positive temperature coefficient of resistance (TCR) α_T and the resistance can be expressed as

$$R_S = R_{S0}[1 + \alpha_T(T - T_0)], \tag{1.4}$$

where R_S is the resistance of the shear-stress sensor at the operating temperature T and R_{S0} is the resistance at a reference temperature T_0.

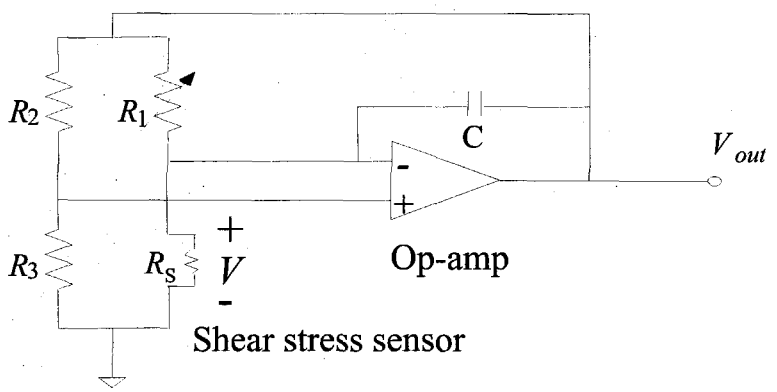

Figure 1.14 Simplified constant temperature circuit.

An important parameter for the operation of shear-stress sensor is the resistive over-heat ratio, which is defined as

$$A_R = (R_S - R_{S0}) / R_{S0} \tag{1.5}$$

For example, if an overheat ratio of 10% is desired, we then set R_1= (1+10%)R_{S0} (assume R_3=R_2). The current heats up the sensing element and increases the resistance while the fluid passing the surface, cools it down and decreases the resistance. When the steady state is reached, these two opposite processes balance with each other and R_S equals R_1. If we assume the TCR of polysilicon is 0.1%/°C, then the average temperature of the sensing element is 100°C above the ambient temperature. The shear stress can be indicated by the voltage across the sensing element. Figure 1.15 shows a typical sensor voltage output as a function of shear stress at CT mode.

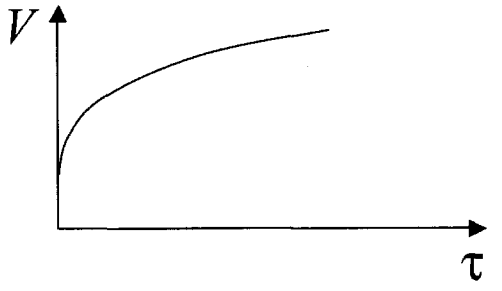

Figure 1.15 Typical voltage output of shear-stress sensor at CT mode.

In the case of CC mode, the sensor is biased by constant current source and the shear stress is monitored by measuring the voltage across the sensing element as shown in the following Figure 1.16. A typical voltage output at CC mode as a function of shear stress is shown in Figure 1.17.

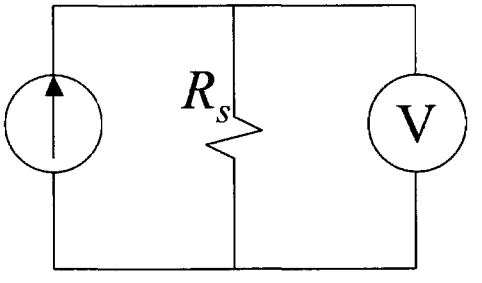

Figure 1.16 Constant Current (CC) mode of shear-stress sensor.

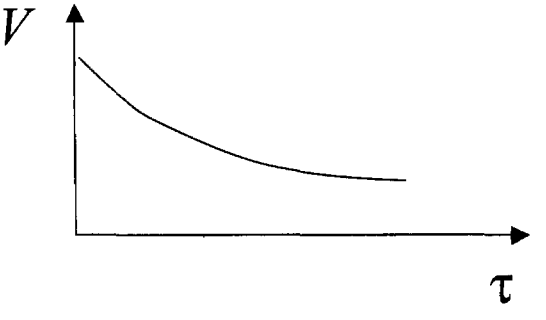

Figure 1.17 Typical voltage output of shear-stress sensor at CC mode.

Compared with CT mode, CC mode has small shear-stress sensitivity and slow dynamic response. However, due to its simplicity, it is still widely used, especially in the case of large arrays of shear-stress sensors.

With a vacuum cavity underneath the nitride diaphragm, the heat loss to substrate is significantly reduced. This reduces the power consumption, improves the sensitivity and frequency response. The micromachined thermal shear-stress sensor outperforms its conventional counterpart in almost every respect. However, it has one drawback, the pressure cross talk. Namely, the shear-stress sensor will also pick up the pressure signal of the fluid passing the surface. For aerial application, it is not a serious problem since the pressure usually does not change significantly and high operating temperature can be used to minimize the pressure sensitivity. However, for underwater applications, this issue has to be addressed. The detailed discussion is presented in Chapter 3.

1.4 Overview of the chapters

In Chapter 1, a brief introduction on the motivation and a review of the flexible skin technology is given first. Then, the basic principle, design, and operation of the micromachined thermal shear-stress sensor are described.

In Chapter 2, the development of a flexible shear-stress sensor skin for Unmanned Aerial Vehicle (UAV) project is described. The complete M^3 (microsensors, microactuators, and microelectronics) system for the control of UAV is also presented.

In Chapter 3, the development of an underwater shear-stress sensor skin for marine applications is presented. The emphasis is put on the two challenges, the waterproof coating and the minimization of the pressure crosstalk, of the underwater

shear-stress sensor. A selective Parylene deposition method and skin-based packaging are described as well.

MEMS-IC integration is not trivial at all. The integration of MEMS and ICs on flexible substrate represents a special challenge. In Chapter 4, the successful development of an IC-integrated shear-stress sensor skin is described. The deployment of the skin is significantly simplified and reliability is improved.

Finally in Chapter 5, the future applications of the MEMS skin technology, beyond the distributed fluidic sensing, are briefly discussed.

References

[1] R. S. Muller, R. T. Howe, S. D. Senturia, R. L. Smith, and R. M. White, *Microsensors*. New York: IEEE Press, 1991.

[2] G. T. A. Kovacs, *Micromachined Transducers Sourcebook*: McGraw-Hill, 2000.

[3] D. J. Beebe, D. D. Denton, R. G. Radwin, and J. G. Webster, "A silicon-based tactile sensor for finger-mounted applications," *IEEE Transactions on Biomedical Engineering*, vol. 45, pp. 151-159, 1998.

[4] H. K. Trieu, L. Ewe, W. Mokwa, M. Schwarz, and B. J. Hosticka, "Flexible silicon structures for a retina implant," presented at IEEE International Conference on Micro Electro Mechanical Systems (MEMS), Heidelberg, Germany, 1998.

[5] T. H. Stearns, *Flexible Printed Circuitry*: McGraw Hill, 1996.

[6] E. Fortunato, I. Ferreira, F. Giuliani, and R. Martins, "Flexible large area thin film position sensitive detectors," *Sensors and Actuators A-Physical*, vol. 86, pp. 182-186, 2000.

[7] M. Boucinha, P. Brogueira, V. Chu, and J. P. Conde, "Amorphous silicon air-gap resonators on large-area substrates," *Applied Physics Letters*, vol. 77, pp. 907-909, 2000.

[8] S. Polach, D. Horst, G. Maier, T. Kallfass, and E. Lueder, "Matrix of light sensors addressed by a-Si:H TFTs on a flexible plastic substrate," presented at SPIE - the International Society for Optical Engineering, San Jose, California, 1999.

[9] T. Stieglitz, H. Beutel, and J. U. Meyer, "A flexible, light-weight multichannel sieve electrode with integrated cables for interfacing regenerating peripheral nerves," *Sensors and Actuators A-Physical*, vol. 60, pp. 240-243, 1997.

[10] T. N. Pornsinsirirak, "Parylene MEMS technology for adaptive flow control of flapping flight," Ph. D. thesis, California Institute of Technology, Pasadena 2002

[11] http://www.ovonic.com.

[12] E. Cheung and V. Lumelsky, "Real time path planning procedure for a whole-sensitive robot arm manipulator," *Robotica*, vol. 10, 1992.

[13] E. R. Post, M. Orth, P. R. Russo, and N. Gershenfeld, "E-broidery: design and fabrication of textile-based computing," *IBM Systems Journal*, vol. 39, pp. 840-860, 2000.

[14] P. W. Barth, S. L. Bernard, and J. B. Angell, "Flexible circuit and sensor arrays fabricated by monolithic silicon technology," *IEEE Transactions on Electron Devices*, vol. 32, pp. 1202-1205, 1985.

[15] D. J. Beebe and D. D. Denton, "A Flexible Polyimide-Based Package for Silicon Sensors," *Sensors and Actuators A-Physical*, vol. 44, pp. 57-64, 1994.

[16] F. Jiang, Y. Xu, T. Weng, Z. Han, Y.-C. Tai, A. Huang, C.-M. Ho, and S. Newbern, "Flexible shear-stress sensor skin for aerodynamics applications," presented at IEEE International Conference on Micro Electro Mechanical Systems (MEMS), Miyazaki, Japan, 2000.

[17] Y. Xu, Y.-C. Tai, A. Huang, and C.-M. Ho, "IC-integrated flexible shear-stress sensor skin," presented at Solid-State Sensor, Actuator, and Microsystems Workshop, Hilton Head Island, South Carolina, 2002.

[18] C. Grosjean, "Silicone MEMS for fluidics," Ph. D. thesis, California Institute of Technology, Pasadena, CA 2001

[19] T. Tsao, F. Jiang, C. Liu, R. Miller, S. Tung, J.-B. Huang, B. Gupta, D. Babcock, C. Lee, Y.-C. Tai, C.-M. Ho, J. Kim, and R. Goodman, "MEMS-based active drag reduction in turbulent boundary layers," in *Microengineering Aerospace Systems*, H. Helvajian, Ed.: The Aerospace Press, 1999, pp. 553-580.

[20] X. Q. Wang, Z. Han, F. Jiang, T. Tsao, Q. Lin, Y. C. Tai, and C. M. Ho, "A fully integrated shear-stress sensor," presented at International Conference on Solid-State Sensors and Actuators (Transducer), 1999.

[21] M. A. Schmidt, R. T. Howe, S. D. Senturia, and J. H. Haritonidis, "Design and calibration of a microfabricated floating-element shear-stress sensor," *IEEE Transactions on Electron Devices*, vol. 35, pp. 750-757, 1988.

[22] T. Pan, D. Hyman, M. Mehregany, E. Reshotko, and B. Willis, "Characterization of microfabricated shear-stress sensors," presented at International Conference On Solid-State Sensors and Actuators (Transducer), Stockholm, Sweden, 1995.

[23] T. J. Hanratty and J. A. Campbell, "Measurement of wall shear stress," in *Fluid Mechanics Measurements*, R. J. Goldstein, Ed., 2nd ed: Taylor & Francis, 1996, pp. 575-648.

[24] C. Liu, Y. C. Tai, J. B. Huang, and C. M. Ho, "Surface micromachined thermal shear-stress sensor," presented at ASME International Mechanical Engineering Congress and Exposition, Chicago, IL, 1994.

[25] Q. Lin, F. Jiang, X. Wang, Z. Han, Y. C. Tai, J. Lew, and C. M. Ho, "MEMS thermal shear-stress sensors: experiments, theory and modeling," presented at Solid-State Sensor and Actuator Workshop, Hilton Head Island, South Carolina, 2000.

Chapter 2

Flexible Shear-Stress Skin and its Application to Unmanned Aerial Vehicle

2.1 Introduction–UAV controlled by M^3 systems

Recently, the Department of Defense (DOD) and the air force have shown great interest in Unmanned Aerial Vehicles (UAVs). UAVs promise to perform a wide variety of theater operations, such as surveillance, targeting, bomb damage assessment, or even strike operations. A project to develop an UAV for the future, having no tail, controlled by microsensors, microactuators, and microelectronics (M^3 systems), and with no traditional control surfaces, is underway at UCLA and Caltech. It does not look feasible at first glance to control a macrosystem by microdevices. However, for a delta wing at high angle of attack, a large fraction of the lift is contributed by the vortices originated from the boundary layers around the two leading edges [1]. The schematic of a delta wing, the leading edges vortices, and the angle of attack are illustrated in Figure 2.1. Of special interest is the separation point where the vortex detaches from the leading edge. It is known that the vortices are very sensitive to small perturbations at their origins [2,

3]. Therefore, we can employ MEMS actuators, whose off-plane displacement matches the boundary layer thickness before separation, to change the leading edge vortices. The ultimate result is the ability to create force imbalance of the high suction vortex pairs and provide independent flight control of pitching, rolling, and yawing. Figure 2.2 shows that both positive and negative moments can be generated due to MEMS flap actuation at different locations around the leading edge.

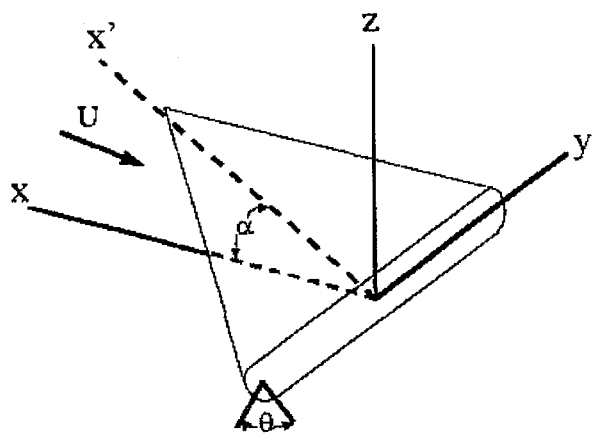

(a)

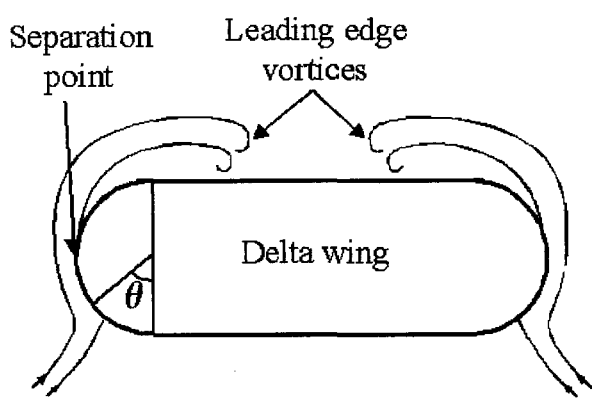

(b)

Figure 2.1 Delta wing model: (a) schematic representation of delta wing; (b) cross section of delta wing.

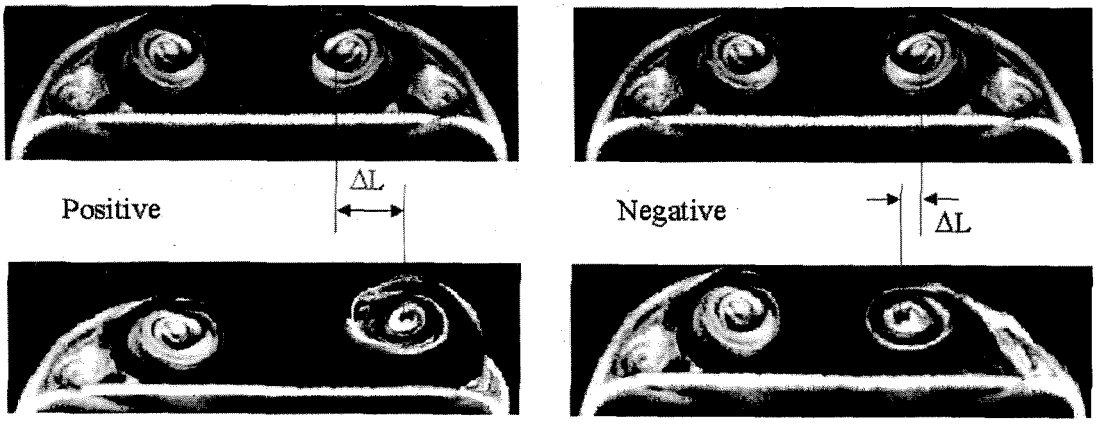

Figure 2.2 Positive and negative moments.

In order to change the vortices in an effective and controllable way, it is crucial to know the separation line along the leading edge. However, for round leading edges, the separation line is a function of multiple variables such as Reynolds number, angle of attack, roll angle, yaw angle, swept angle, and so on. The only reasonable way to detect the separation is to mount arrays of sensors around the leading edge to perform real-time detection. Since the emerging of MEMS technology, arrays of miniaturized sensors on rigid chip have been demonstrated [4]. Nevertheless, to mount arrays of sensors to nonplanar surfaces has long been a big challenge. A novel flexible skin technology was developed in the micromachining laboratory at Caltech to address this problem [5]. In terms of flow separation detection, the shear-stress measurement is an effective way. Therefore, flexible skins which contain arrays of shear-stress sensors are desirable to detect the separation line along the leading edge. At the same time, flexible actuator skins are also necessary, which will not be covered in this thesis. The reader can refer to [6] for the details of the balloon actuator skins developed for this UAV project.

The basic concept of the UAV controlled by M^3 system can be illustrated with the help of Figure 2.3. First, the flexible shear-stress sensor skin detects the separation line of the lead edge vortices. Then the microactuator, which has a displacement comparable to the boundary layer, is applied at the appropriate location to perturb the leading edge vortices, generating desirable macro control moment. In this process, microelectronics is necessary to collect and process the sensor data and control the actuators accordingly.

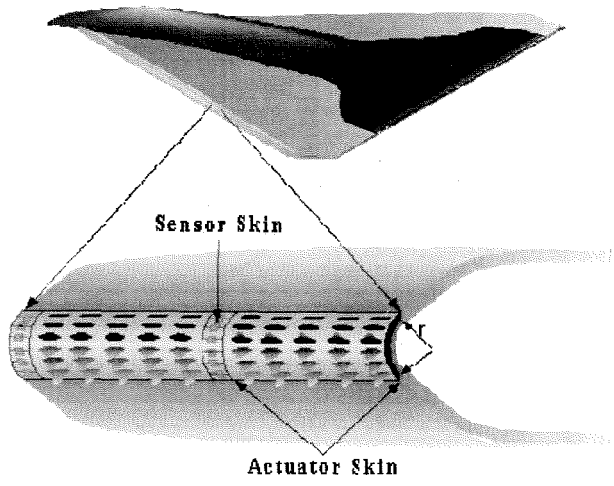

Figure 2.3 Concept of the UAV controlled by M^3 systems.

2.2 Design and fabrication

Measuring fluid parameters such as shear stress along nonplanar surfaces has long been a big challenge. We have previously reported the development of a flexible shear-stress sensor skin [5]. However, the packaging remains the bottleneck to install the sensor skin on the UAV. The traditional fine wire bonding and electrical wire soldering were used to connect the sensors out. As shown in Figure 2.4, this process was laborious

and unreliable. Continuing our previous research, we developed a new, improved skin technology. For example, the new skin technology employs DRIE to improve yield. Most importantly, the new skins can be solder-bonded to flexible Kapton PCBs, which significantly simplifies the packaging and improves the reliability. All these improvements will be discussed in detail in the following sections.

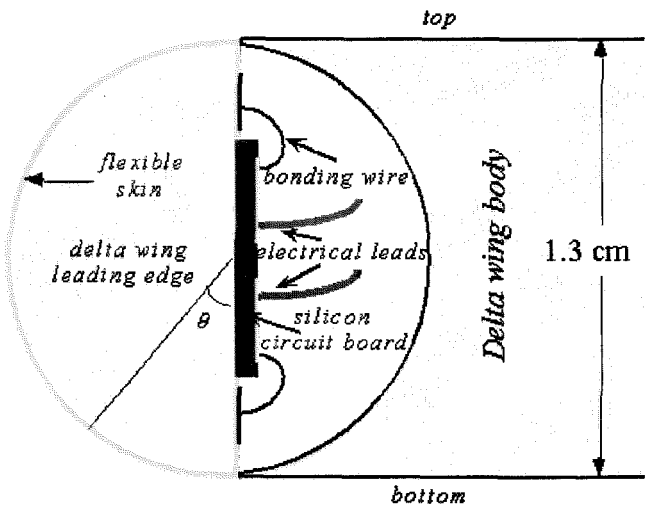

(a)

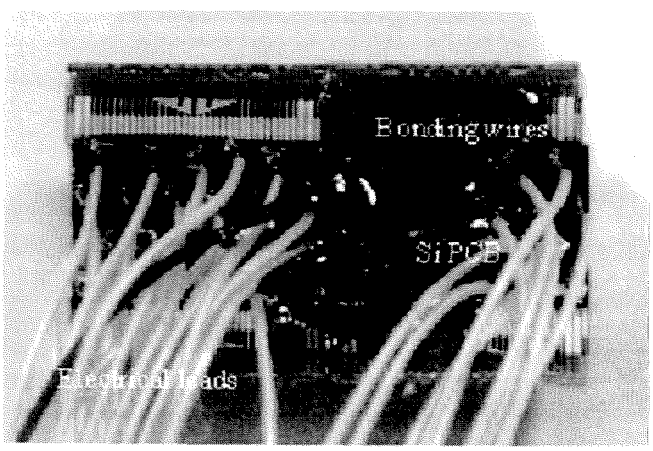

(b)

Figure 2.4 (a) Schematic of the packaging scheme based on wire-bonding and electrical lead soldering; (b) Picture of a packaged sensor skin on a semicylindrical block [7].

The new shear-stress sensor skins are designed for flow separation detection on the leading edges of a delta-wing airplane through shear-stress distribution measurement. There are 36 shear-stress sensors on the skin, spanning the distance of 19.6 mm which can cover the 180° surface of a half-inch diameter semicylindrical leading edge with 5° resolution.

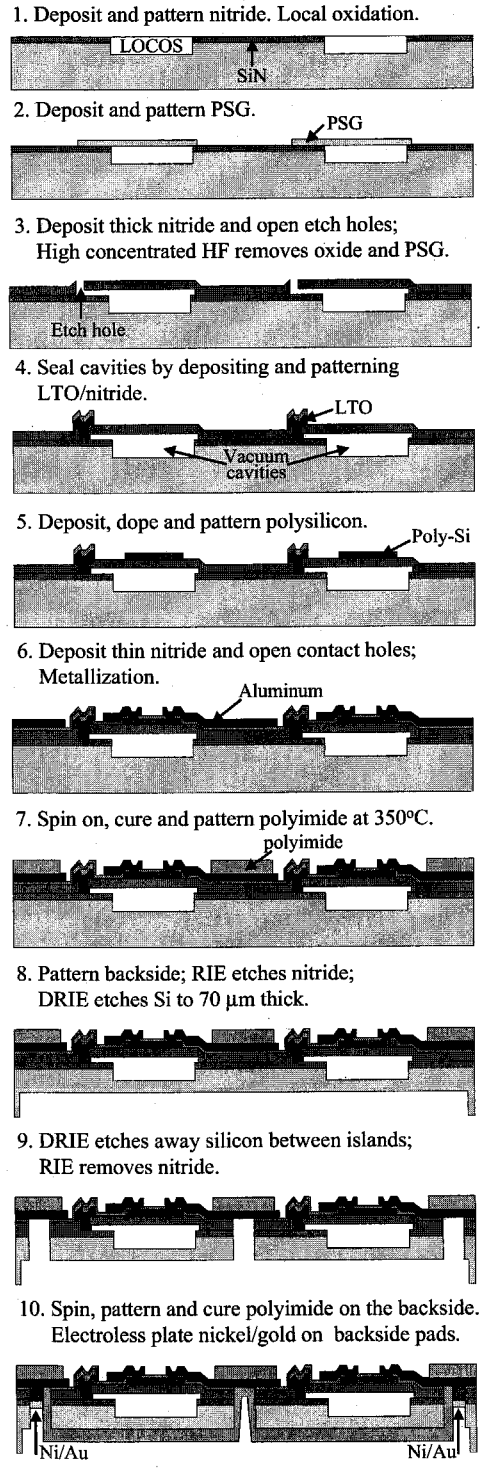

Figure 2.5 The simplified fabrication process.

The fabrication process of the sensor skin is illustrated in Figure 2.5. From one perspective, this was a complicated process since it consisted of nearly 20 masks and took almost one year to finish. But from another perspective, this fabrication process is straightforward. The first six steps is the fabrication of shear-stress sensors on rigid substrate. The next four steps is the fabrication of the skin structure. Therefore, this is a *modular process.*

The process starts with making double-side alignment marks on double-side polished 4" silicon wafers. Then 0.6 μm low stress silicon nitride, which serves as oxidation mask, is deposited by low pressure chemical vapor deposition (LPCVD). After patterning the silicon nitride with O_2/CF_4 plasma, O_2/SF_6 plasma is used to further etch into silicon substrate to form cavities 1.2 μm deep. During the O_2 and CF_4 plasma etching, micrograss may appear at the nitride/silicon interface. To prevent this, HF dip is necessary before nitride deposition to ensure there is no native oxide. With local oxidation (LOCOS), these cavities are filled with silicon dioxide. The purpose of this LOCOS process is to planarize the cavities. Usually the oxide is grown to be a little higher than the nitride (the oxide is about 2.5 μm thick), then the wafer is dipped in Buffer HF (BHF) to etch back oxide to planarize the surface.

Next, 0.5 μm phosphosilicate glass (PSG) is deposited, densified and patterned to form the etching channels. It is worth noting that the densification step is not optional. Otherwise the etching front of PSG will be irregular in BHF. This layer of PSG is only 0.5 μm thick to make the sealing of the cavity relatively easy. After patterning, the PSG is reflowed at 1050°C to round sharp angles. Then 1.6 μm low stress nitride is deposited to form the diaphragm and etching holes are opened with RIE. The oxide and PSG are

etched away by concentrated HF (48%). Note that the etching rate of silicon nitride in concentrated HF is 5 nm/min. Low temperature oxide (LTO) is deposited to seal the cavity in vacuum. The deposition pressure of the LTO is about 200 mtorr. But this is the pressure at 450°C and the remaining gases (SiH_4 and O_2) in the cavity will continue to react. The real pressure in the cavity will be much less than 200 mtorr which is virtually vacuum in terms of thermal isolation. LTO is actually not very good with respect to sealing quality [8]. Therefore another layer of nitride is deposited to ensure better sealing. To reduce the heat loss to substrate, this layer of nitride is etched away by RIE on the diaphragm using the LTO as the etching stop. Afterwards, this LTO layer is also removed by BHF.

The next step is the polysilicon process to form the sensing element. The polysilicon is deposited at 560°C. At such low temperature, what we actually obtain is amorphous silicon. After boron ion implantation, the amorphous silicon is converted to polysilicon with high temperature annealing (1050°C). The reason for doing this is that polysilicon, deposited in an amorphous state at low temperature and subsequently crystallized at high temperature, has more controllable qualities than as-deposited polysilicon deposited at 620°C [9]. The doping concentration is chosen as 2×10^{20} cm^{-3} to achieve a positive TCR of 0.1%/K. This doping concentration is sufficient to form good ohmic contact between polysilicon and aluminum. Therefore, no extra doping is required in the contact areas.

Another 0.2 μm nitride is deposited for passivation after patterning the polysilicon with DRIE. Contact holes are then opened by PE II plasma etcher using O_2 and CF_4. Since there is no etch stop underneath the 0.2 μm nitride, the etch process has to be

carefully monitored. The reason to use CF_4 instead of SF_6 is that CF_4 plasma etches polysilicon at a rate slower than that of SF_6. A thin layer of LTO can also be deposited as etch stop, which makes this step much more controllable. Then aluminum is evaporated, patterned and sintered at 450 °C to form good ohmic contact. Now the fabrication of shear-stress sensors on rigid substrate is finished.

The fabrication of the skin structure starts with spin-coating polyimide (Du Pont PYRALIN® PI2808) on the front side of the wafer. The polyimide is cured in N_2 environment at 350 °C and patterned by RIE using O_2 plasma to expose the shear-stress sensors for a high sensitivity as shown in Figure 2.6. Since this layer of polyimide is 10 μm thick, to safely pattern it, the mask material (photoresist) should be as thick as 20 μm. When dealing with such thick photoresist, caution must be taken to avoid cracking.

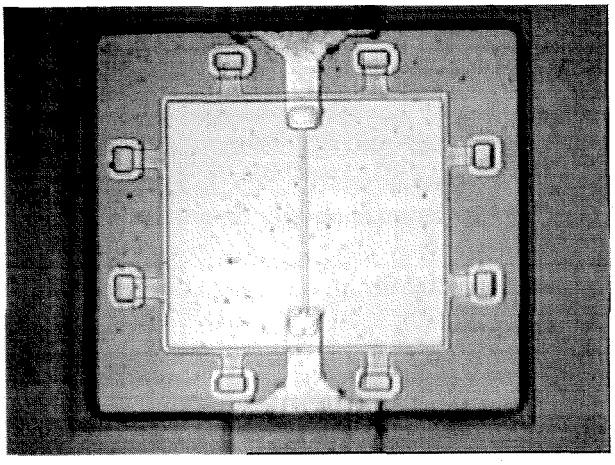

Figure 2.6 The polyimide is patterned to expose the shear-stress sensor.

The nitride and LTO layers on backside are patterned and the wafer is thinned down to 70 μm by DRIE. Note that only the skin areas are thinned down. The silicon between the skins is left to provide adequate mechanical support.

Next, silicon islands are formed by etching away silicon in between using DRIE again. It is worth noting that when photoresist is spin-coated on the cavity, it ends up with highly nonuniform photoresist. More conformal coating methods, such as spray-coating or vapor phase coating, are preferred. After etching away the silicon by DRIE, further etching in RIE is carried out to remove the nitride deposited on front side. Otherwise, this nitride layer will easily crack and break the aluminum wires when the skin undergoes bending.

Another layer of polyimide is spin-coated on the backside to encapsulate silicon islands. To open the pads on the backside, we need to pattern the polyimide. However, due to the nonuniform photoresist coating on the cavity, it is impossible to pattern polyimide by dry etching (O_2 plasma). Fortunately, the uncured backside polyimide can be patterned by wet etchant, namely, photoresist developer (AZ 351, diluted with DI water), at the same time as the photoresist is developed. Note that AZ 351 contains TMAH which attacks aluminum. After removing the photoresist by butyl acetate, a solvent more gentle than acetone, the polyimide is cured at 350 °C.

Since solder does not stick to aluminum directly, to employ the solder bonding, nickel is first electrolessly plated on aluminum pads and then gold is plated on nickel. Note that during electroless plating, the front side needs to be protected by photoresist. The method of electroless plating nickel/gold on top of aluminum was developed by Stapleton Technologies Inc. [10] and is widely used in making solder bump for flip-chip bonding. The electroless plating of nickel/gold is the last step of the skin fabrication.

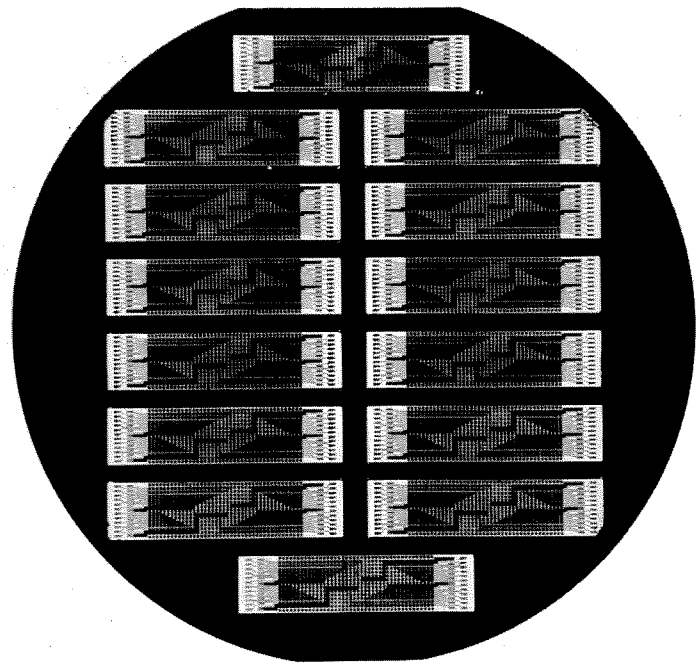

Figure 2.7 Sensor skin wafer with white light illuminated from backside.

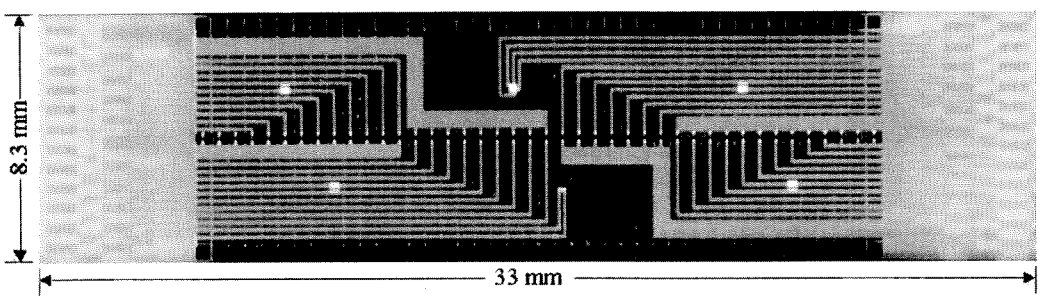

Figure 2.8 Fabricated shear-stress sensor skin cut from the wafer.

When the skin fabrication is finished, the wafer is almost transparent as shown in Figure 2.7. There are 14 sensor skins on one 4" wafer. The arrays of silicon islands and aluminum wires can be clearly observed with the help of the light illuminated from backside of the wafer. Figure 2.8 shows one fabricated shear-stress sensor skin cut from the wafer. The dimension of skin is 8.3×33 mm^2. Therefore, the skin is composed of

five dies since one die is only 10 × 10 mm^2. Due to the symmetry, three masks are enough for one single photolithography. There are 36 shear-stress sensors, and one temperature sensor integrated on skin. On each end of the skin, there are two columns of aluminum pads with openings on the backside. Note that nickel/gold are plated on the aluminum pads for solder-bonding.

2.3 Packaging of the sensor skin

To connect the sensor out, a special flexible PCB, as illustrated schematically in Figure 2.9, is designed. On the narrow end, there are two columns of small solder-bonding pads which correspond to the pads on the skin. On the other end of the flexible PCB, there is one column of large soldering pads which are compatible with the standard connector.

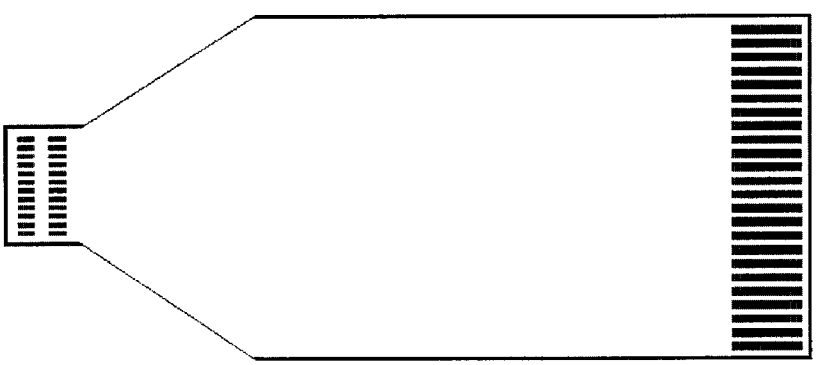

Figure 2.9 Schematic of the flexible PCB. The wires connecting the left small pads and right big pads are not shown.

The soldering bonding between sensor skin and flexible PCB is illustrated in Figure 2.10. First, solder is applied on the pads of the sensor skin. Then the flexible PCB is aligned to the sensor skin under a stereo microscope and fixed with the help of some

glue (RTV). After the glue is dry, the attached sensor skin and flexible PCB are laid on the top of a hotplate and a uniform pressure is applied on the pads area. Finally, the hotplate is heated up to 200°C, which exceeds the melting temperature of solder. After cooling down, the sensor skin is bonded to the flexible PCB. Figure 2.11 shows a sensor skin solder-bonded to a flexible PCB.

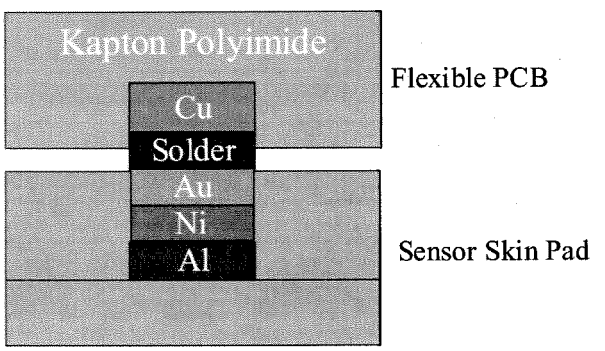

Figure 2.10 Solder bonding between flexible skin and flexible PCB.

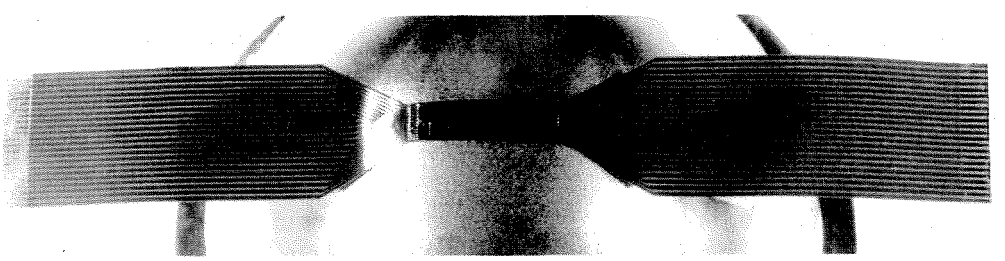

Figure 2.11 A sensor skin solder-bonded to a flexible PCB with a dome underneath.

To measure the shear-stress distribution along a round leading edge, the sensor skin is wrapped around an aluminum block and fixed with epoxy as shown in Figure 2.12. The diameter of the aluminum block is 0.5 inch. As we mentioned before, the 36 shear-stress sensors can cover 180° of it. Then the aluminum block can be installed on a delta-wing model for wind tunnel test or an UAV for real flight test.

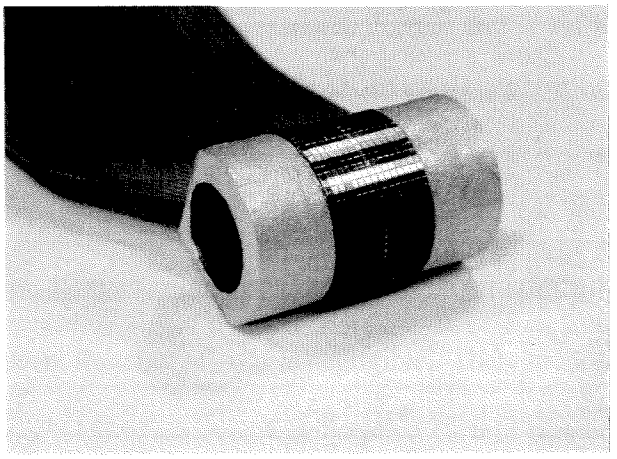

Figure 2.12 A sensor skin packaged on an aluminum block with a diameter of 0.5 inch.

2.4 Bias circuits and data acquisition, signal processing and control board

As mentioned in Chapter 1, the thermal shear-stress sensors can be biased in either constant current (CC) or constant temperature (CT) modes. CT mode is more commonly used due to its faster frequency response (up to 10 KHz with the current shear-stress sensors) and higher sensitivity, which are crucial to many fluid mechanics measurements. However, the CT circuits are complicated, and they are impractical to implement for large amounts of sensors. Fortunately, to determine a flow separation point, we only need a bandwidth in the order of 1 KHz, which can be achieved by CC mode. Therefore, the simple CC mode is chosen for this application to greatly reduce the system complexity. A constant current mirrors chip is fabricated using the 2 μm MOSIS CMOS foundry. Figs. 2.13 and 2.14 are the circuit diagram and the chip micrograph (2 × 2 mm^2). The cascode current mirror is for high output impedance and the large transistor is for minimizing V_{GS} as well as for good uniformity. The output current in

each channel is $I_{ref}/2$, where I_{ref} is the reference current and is set by an external three-terminal adjustable voltage regulator LM317L and a resistor R_r. I_{ref} can be estimated by

$$I_{ref} = \frac{1.25}{R_r}$$

since the voltage between the output (OUT) and adjustment terminals (ADJ) of LM317L is 1.25 V and the current flow out of ADJ is negligible. There are totally 36 channels and a current uniformity of ±1% is achieved. A constant current bias board, which contains 3 MOSIS constant current chips, was fabricated as shown in Figure 2.20.

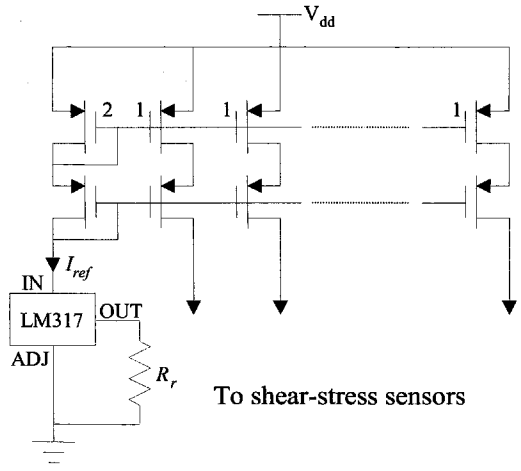

Figure 2.13 Constant current bias circuits consisting of MOSIS current mirrors and a three terminal adjustable voltage regulator LM317.

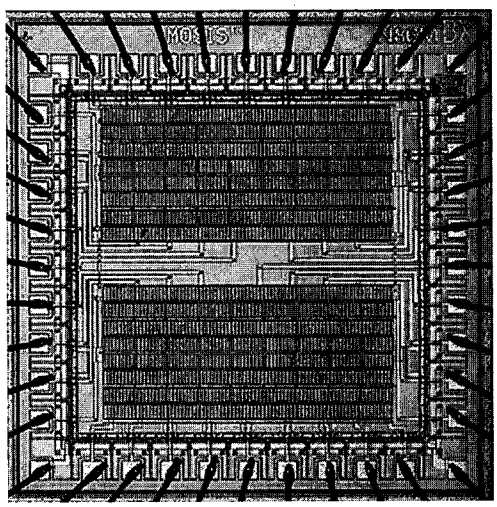

Figure 2.14 Picture of a MOSIS constant current bias chip.

In order to acquire the data from the sensor skins, then process the data and accordingly send out actuation signals to the balloon actuators at the appropriate position, a data acquisition, signal processing, and control board is required. The block diagram of such a board was depicted by the parts inside the dashed rectangular in Figure 2.15, which illustrates the complete M^3 system for UAV. Up to 200 sensor outputs can be multiplexed into a 14-bit A/D converter through a high input impedance JFET buffer stage. Each sensor is sampled at 1 kHz and every 100 digitized data points from each sensor are then processed by a DSP (TI C50) to generate the mean and RMS (or standard deviation) values at a rate of 10 Hz. The flow separation point can be determined based on these values. The microballoon actuator is then activated accordingly. With the help of this flight CPU, we can establish wireless communication with the data acquisition, signal processing, and control board. A picture of the data acquisition, signal processing, and control board is shown in Figure 2.20.

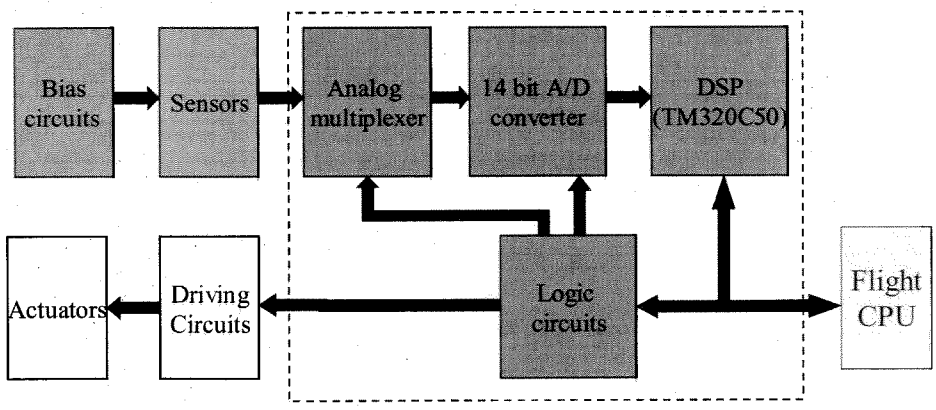

Figure 2.15 Block diagram of the M^3 UAV control system. The red dashed rectangle illustrates the data acquisition, signal processing, and control system.

2.5 Wind tunnel test of sensor skin

The sensor skin is first installed on the leading edge of a delta-wing model and tested in the wind tunnel. The delta wing model has a swept angle of 56.5° and chord length of 30 cm as shown in Figure 2.16. Figure 2.17 shows a sensor skin, which is pre-mounted on a semicylindrical aluminum block, installed on the leading edge of a delta-wing model. The packaging scheme is illustrated in Figure 2.18.

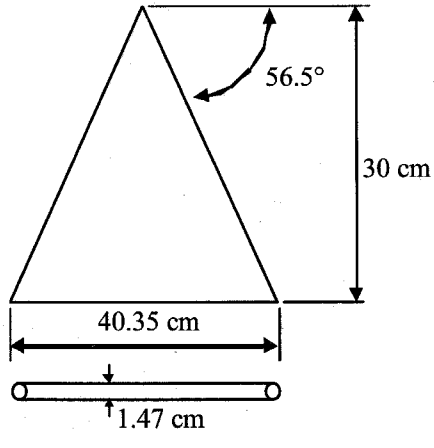

Figure 2.16 Schematic of the delta wing model.

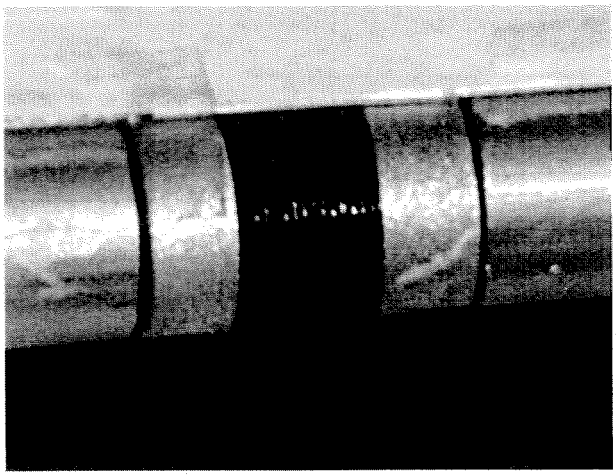

Figure 2.17 Flexible shear-stress sensor skin installed on the leading edge of a delta-wing model.

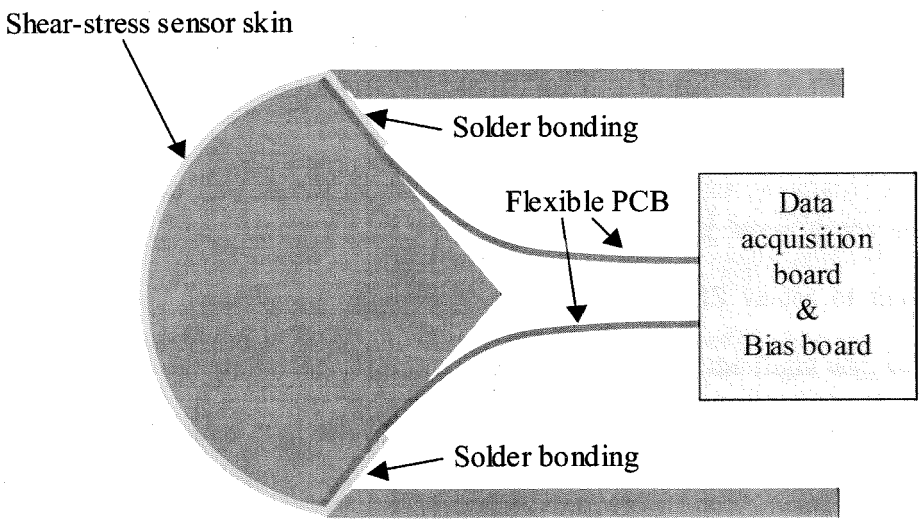

Figure 2.18 The packaging scheme of the sensor skin on the leading edge.

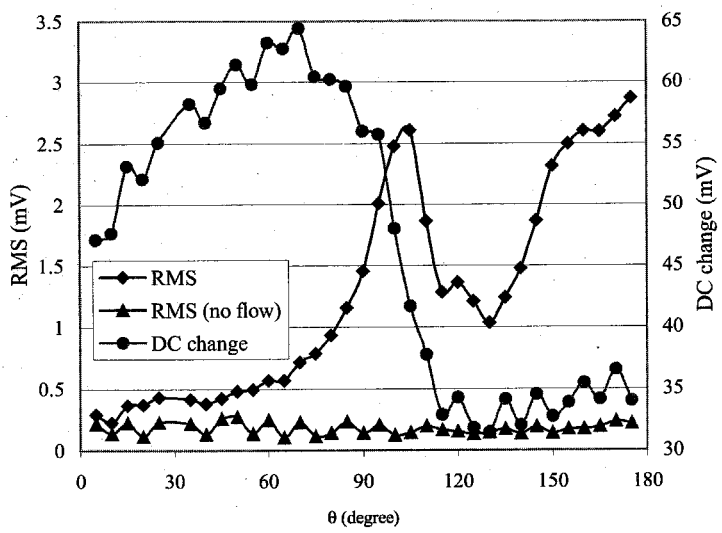

Figure 2.19 RMS and DC change measured by a sensor skin biased in constant current mode at an over-heat ratio of 20% in wind tunnel.

The DC voltage changes and the RMS voltages of all sensors are plotted in Figure 2.18 for an airflow speed of 10 m/s and angle of attack (AOA) of 25°. It is known that after flow separates from leading edge surface, the mean shear stress drops while its fluctuation increases dramatically. Therefore either DC or RMS values of the sensor array can be used to determine the separation point. Later on, in the flight test, we found that the RMS data from the flight test is not as clean as those from wind tunnel test (Fig. 2.19) and the separation point is not so obvious. On the other hand, the DC values show a clear valley after flow separation for all situations.

2.6 Flight test of the sensor skin

The flow separation detection system consists of the packaged sensor skin, bias board and data acquisition board as illustrated in the Figure 2.20. Note that the interconnect cables are not shown in the figure. Since the purpose of this flight test was to

demonstrate the flow separation point detection by the sensor skin, the signal processing and control function mentioned in section 2.4 were not used. This system was installed on an Unmanned Aerial Vehicle (UAV) named Gryphon, which has a wing span of 71.6 in, a root chord of 53.3 in, and a weight of 22 lbs. In order to maintain appropriate weight and balance, the bias board and DAQ board were installed on opposite sides of the aircraft. Gryphon is powered by an internal combustion engine that drives a ducted fan and is remotely piloted. The flight computer and sensor suite include a full set of transducers that measure aircraft motion and performance parameters.

The flight-test was performed on November 16, 1999, at El Mirage Dry Lake in San Bernardino County, California. Flight maneuvers generally consisted of a range of maneuvers at high and slow speed. Most emphasis was placed on obtaining high-speed and high angle-of-attack data that was similar to wind-tunnel tests conditions. This was achieved by performing high-speed, high-g loops and turns at relatively constant angle of attack. While this is a dynamic flight condition, speed and angle of attack can be maintained throughout the maneuver. Additionally roll maneuvers were performed that caused a local angle-of-attack change at the sensor array position.

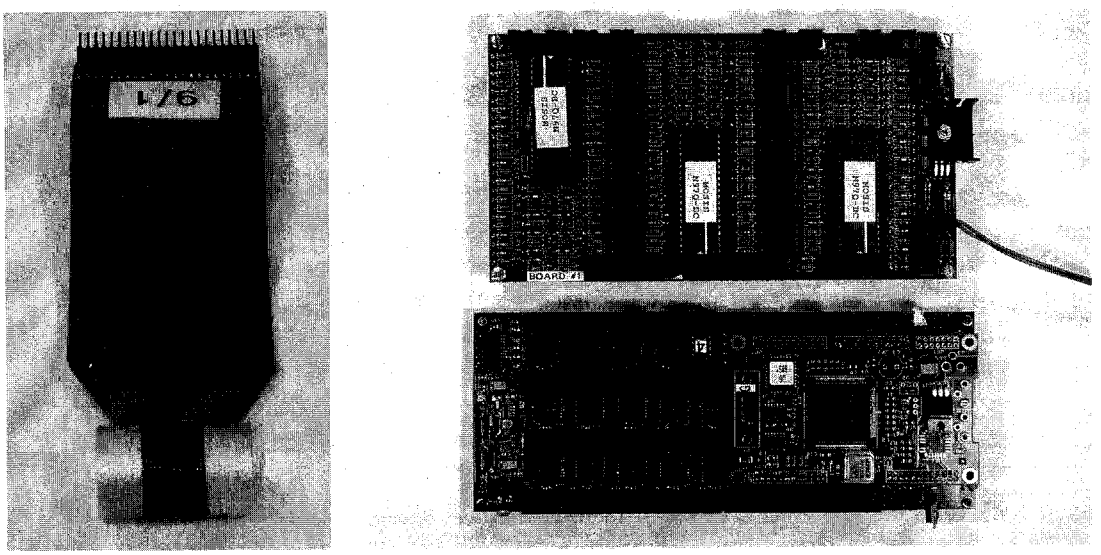

Figure 2.20 The flow detection separation system consisting of a packaged sensor skin, a constant current bias board and a data acquisition board.

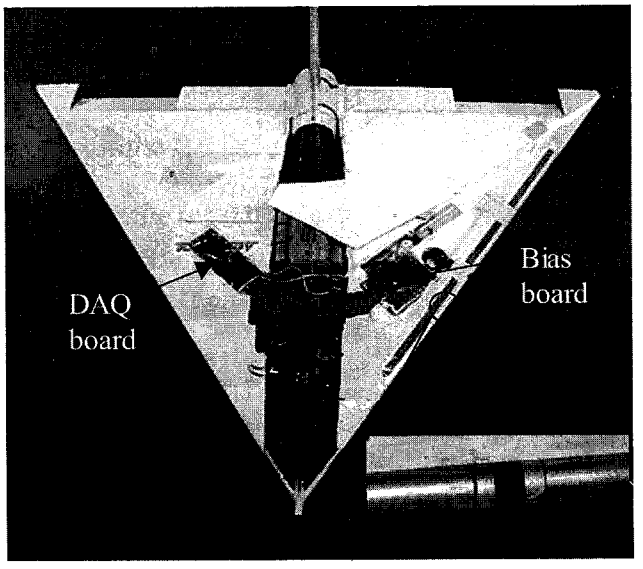

Figure 2.21 The UAV installed with the flow separation detection system.

Data were downloaded from the data acquisition board after landing and the shear-stress data were synchronized with flight parameters recorded by instrumentation system on Gryphon. Fig. 2.22 shows the flight speed and angle-of-attack data together

with the output from sensors #5 and #34, which are located near the bottom and the upper surfaces of the wing, respectively. As we expect, sensor #5 is in the laminar flow region and #34 is in turbulent flow (vortex) region at most flight conditions. The spikes on the RMS data of sensor #5 correspond to the roll of the aircraft which is reflected on the AOA oscillations around 237 s and 335 s. Figure 2.23 shows the sensor array outputs at certain moments when the flight speed and AOA are in steady state. We can see that the separation points move from upper surface of the wing (with large θ) towards the bottom surface of the wing (small θ) when AOA increases. We also notice that the RMS values from the few sensors in the very beginning (small θ) are unexpectedly large. This may be due to the nonideal factors, such as the cross flow traveling along the leading edges and the slight yawing of the aircraft during flight. More flight tests are needed to find out the exact causes. It is found that the RMS data from the flight test do not always show an obvious separation point, while the DC values show a clear valley after flow separation for all situations. Therefore, the separation determination method should use the sensors' DC changes instead of using RMS values. This also greatly simplifies the algorithm for real-time separation point identification.

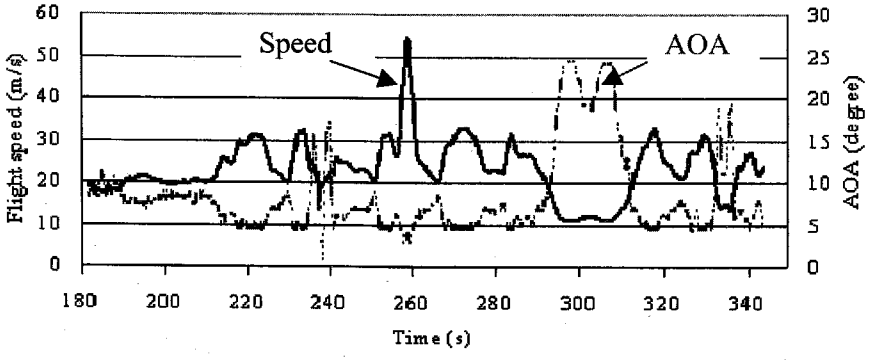

(a) Flight speed and angle of attack.

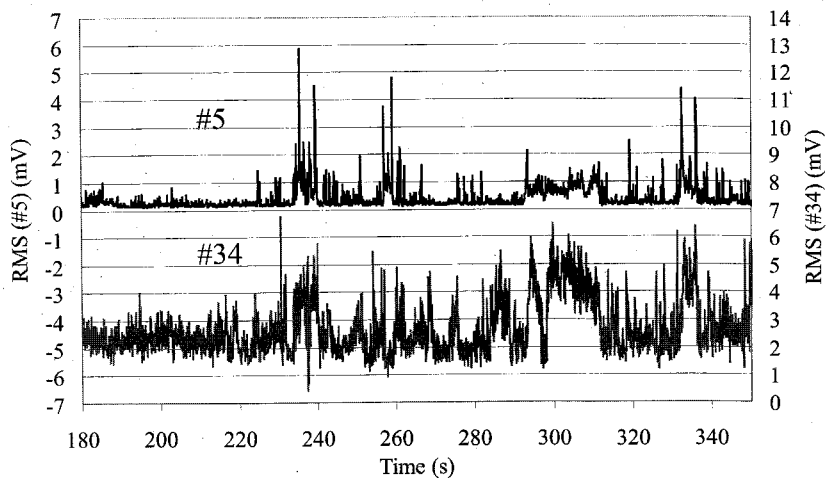

(b) Selected shear-stress sensor data from sensor #5 and #34.

Figure 2.22 Flight data and RMS data of selected sensors (#5 and #34) from one flight (from take-off to landing).

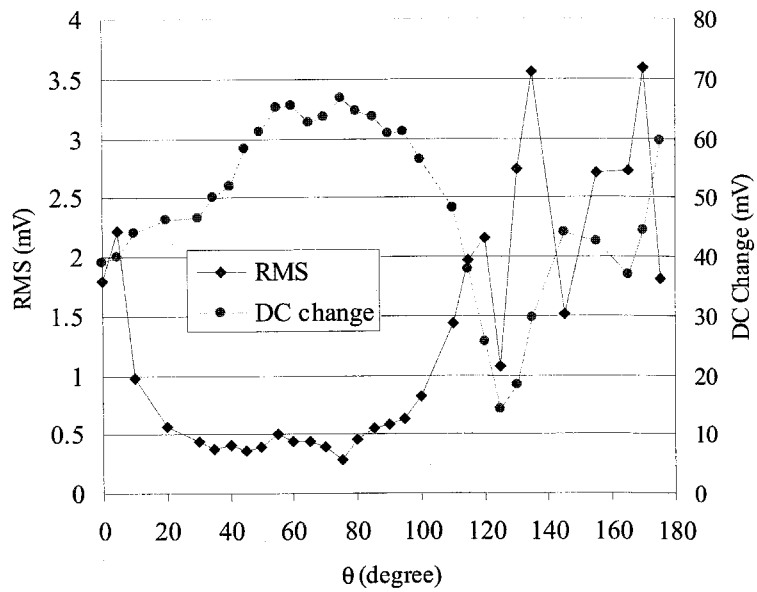

(a) AOA: 10°; speed: 17.5 m/s; separation point: 125°.

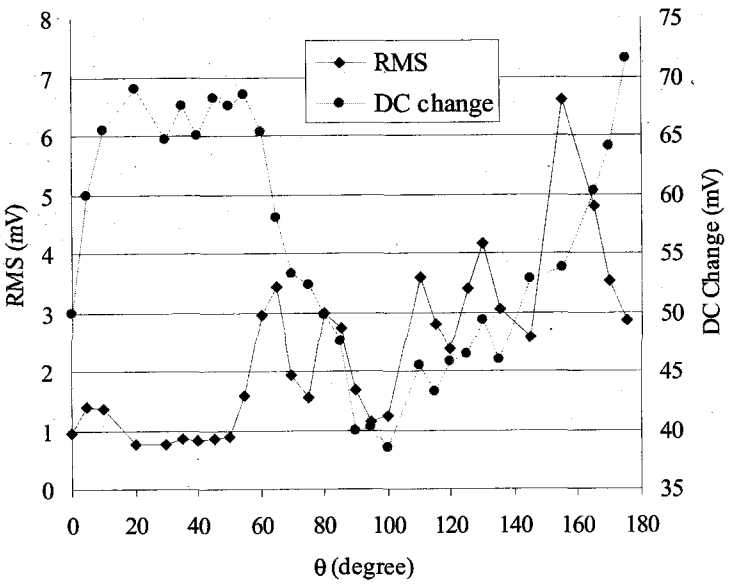

(b) AOA: 24°; speed: 11 m/s; separation point: 100°.

Figure 2.23 RMS and DC values measured by the sensor skin at different flight conditions.

2.7 The M^3 system

In order to maneuver the flight of the UAV, we also need actuator skins mounted on the leading edge to perturb the vortex based on the information collected by the sensor skin. The displacement of these actuators is comparable to the boundary layer thickness, which is in the order of millimeters, around the leading edge. Figure 2.24 shows two balloon actuators based on copper substrate and silicone rubber [6]. In addition, microelectronics is required to collect data, perform signal processing, and deliver actuation signals. Therefore, the UAV is controlled by M^3 system (microsensors, microactuators, and microelectronics). The block diagram of this system is depicted in Figure 2.15. In a sensing-computing-actuating loop, the sensor skins first measure the

shear-stress distribution around the leading edge; the DSP processes the data collected, and calculates the flow separation points; the actuators are then driven accordingly at the appropriate locations to change the leading edge vortices. In this way, we can achieve the control of a macroscale system via microdevices. The M^3 system was first tested in the wind tunnel. As shown in Figure 2.25, two sensor skins and two segments of actuator skins are mounted on one of the leading edges of the delta wing model. The bias board and data acquisition/control board were placed outside the wind tunnel. The rolling of the delta wing via close-loop control was successfully observed.

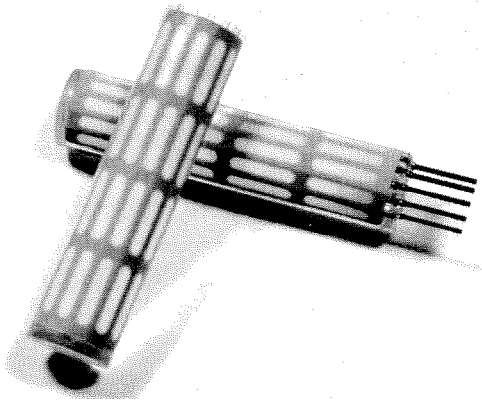

Figure 2.24 Two leading edge balloon actuator assemblies on acrylic rods [6].

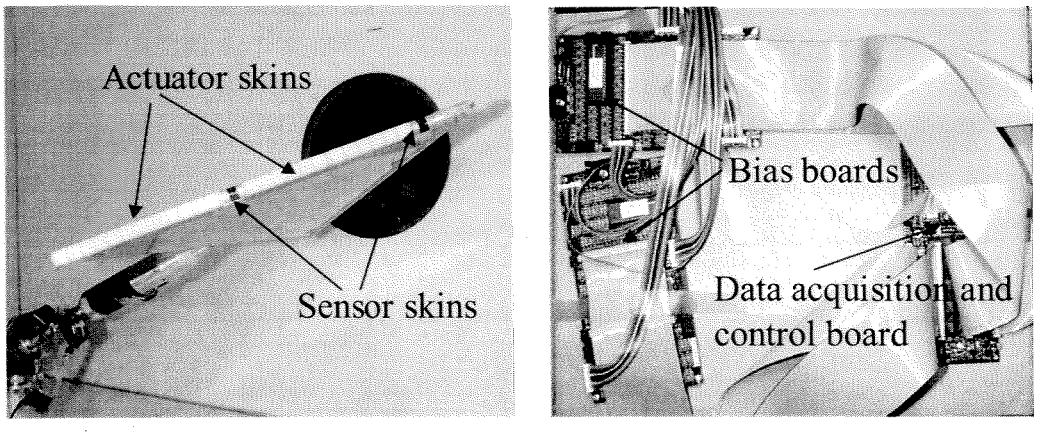

Figure 2.25 The close-loop control testing setup in wind tunnel.

A new UAV, called Super Gryphon, was built by AeroVironment. The Super Gryphon is a large improvement over the Gryphon aircraft with respect to manufacturing and durability. The key feature is a modular leading edge that allows replacement leading edges with various devices while maintaining a smooth surface transition around the leading edges. The Super Gryphon is slightly larger than the Gryphon and is much stronger and has a higher thrust-to-weight ratio. This allows testing at higher wing-loadings and therefore higher speeds for a given angle of attack. Operating at these conditions is more representative of a fighter application and should improve the effectiveness of leading edge actuators. Figure 2.26 shows the outside and the instrumentation inside of the newly built Super Gryphon. The M^3 system installed on Super Gryphon consists of five sensor skins, four segments of actuator skins (Figure 2.27), two bias boards, one data acquisition/control board, and a lot of interconnection cables. The ground tests have been finished and the flight test is ready.

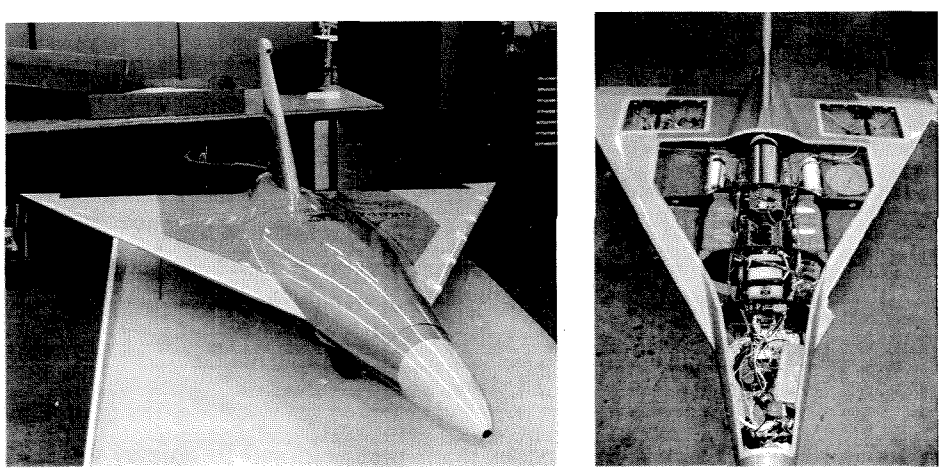

Figure 2.26 The exterior and inside instrumentation of Super Gryphon.

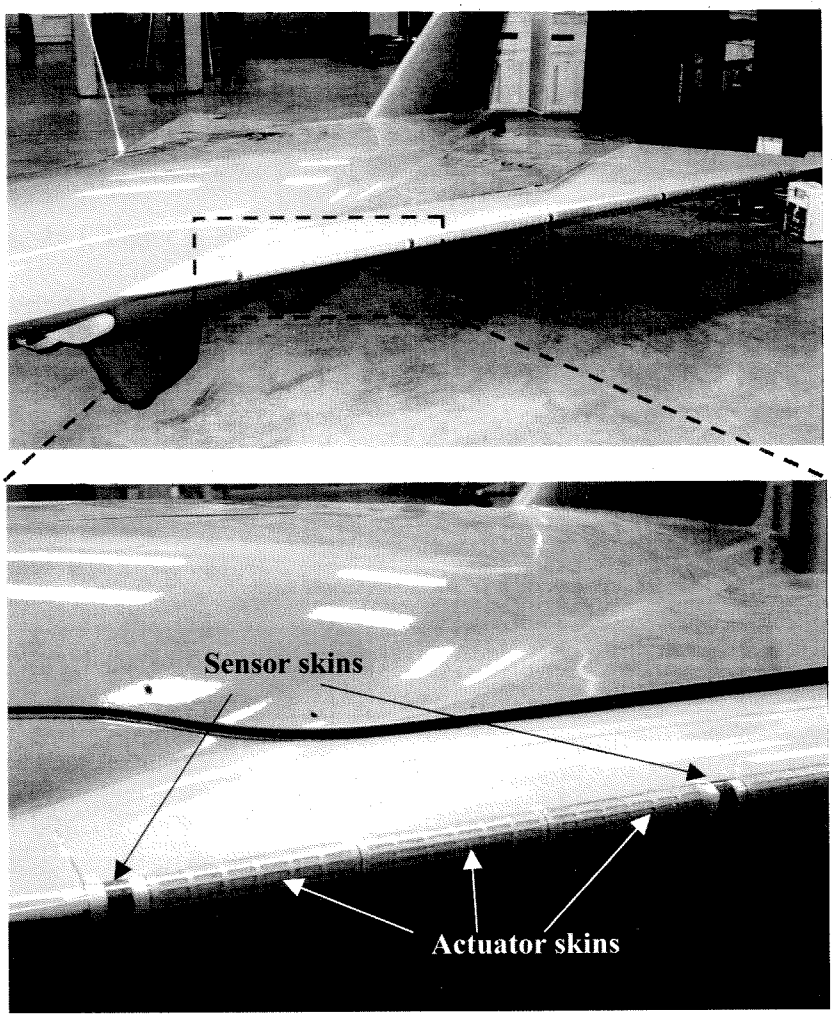

Figure 2.27 The leading edge of Super Gryphon mounted with balloon actuator skins and shear-stress sensor skins.

2.8 Summary

A new version of flexible shear-shear sensor skin was successfully fabricated and tested on an Unmanned Aerial Vehicle. The yield and packaging were improved. Flow separation point detection was demonstrated in both wind tunnel and real flight test. The complete UAV system is an M^3 system, which contains microsensors, microactuators,

and microelectronics. This system was demonstrated in wind tunnel and we are ready for the flight test. Ideally, we want this M^3 system to be integrated onto one single skin to simplify the packaging and improve the reliability. But so far they are separate components. In Chapter 4, the development of an IC-integrated shear-stress sensor skin will be described, which represents an important milestone towards a totally integrated smart skin system.

References

[1] C. M. Ho and Y. C. Tai, "Review: MEMS and its applications for flow control," *Journal of Fluids Engineering-Transactions of the Asme*, vol. 118, pp. 437-447, 1996.

[2] C. M. Ho and L. S. Huang, "Subharmonics and vortex merging in mixing layers," *Journal of Fluid Mechanics*, vol. 119, pp. 443-473, 1982.

[3] C. M. Ho and P. Huerre, "Perturbed free shear layers," *Annual Review of Fluid Mechanics*, vol. 16, pp. 365-424, 1984.

[4] G. T. A. Kovacs, *Micromachined Transducers Sourcebook*: McGraw-Hill, 2000.

[5] F. Jiang, Y.-C. Tai, K. Walsh, T. Tsao, G.-B. Lee, and C.-M. Ho, "Flexible MEMS technology and its first application to shear stress sensor skin," presented at IEEE International Conference on Micro Electro Mechanical Systems (MEMS), Nagoya, Japan, 1997.

[6] C. Grosjean, "Silicone MEMS for fluidics," Ph. D. thesis, California Institute of Technology, Pasadena, CA 2001

[7] F. Jiang, "Silicon-micromachined flow sensors," Ph. D. thesis, California Institute of Technology, Pasadena 1998

[8] L. Chang and T. Yu-Chong, "Sealing of micromachined cavities using chemical vapor deposition methods: characterization and optimization," *Journal of Microelectromechanical Systems*, vol. 8, pp. 135-145, 1999.

[9] G. Harbeke, L. Krausbauer, E. F. Steigmeier, A. E. Widmer, H. F. Kappert, and G. Neugebauer, "Growth and physical properties of LPCVD polycrystalline silicon films," *Journal of the Electrochemical Society*, vol. 131, pp. 675-682, 1984.

[10] "MICRO-TECH: flip chip under bump metallization," Stapleton Technologies Inc., Technical Notes, 1997.

Chapter 3

Underwater Flexible Shear-Stress Sensor Skin

3.1 Introduction

Wall shear-stress measurement is of crucial importance for a lot of fluid dynamic monitoring/diagnostics applications. For example, we have developed shear-stress sensors for flow separation detection for an unmanned aerial vehicle (Chapter 2) and for active drag reduction [1, 2]. As we noticed, almost all the MEMS effort has been spent on developing sensors in air, rather than in liquid (e.g., water) [3-6]. Nevertheless, there are a lot of applications that require underwater shear-stress sensors. Examples include the flow patterns measurement of radio controlled submarines, the study of safety and arming mechanisms of torpedoes, to name a few. However, there is a lack of underwater shear-stress sensors on the market.

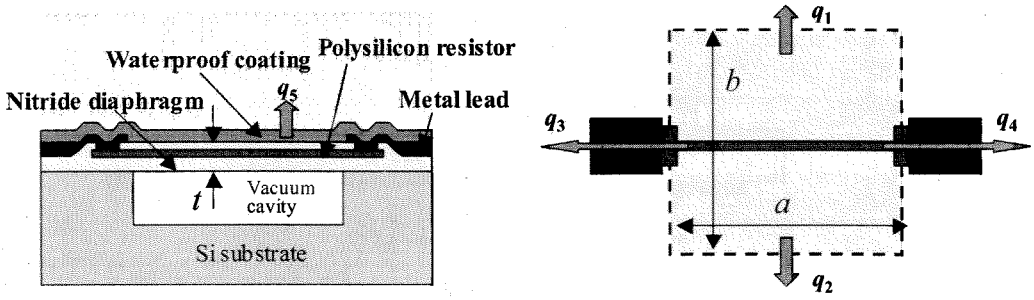

Figure 3.1 Cross section and top view of the underwater shear-stress sensor.

It is then the purpose of this work to develop a vacuum-cavity insulated thermal shear-stress sensor for underwater applications. The cross section and top view of the underwater shear-stress sensor is illustrated in Figure 3.1. Although the basic structure is very similar to aerial shear-stress sensors [3, 4], there are several challenges for the development of the underwater devices. The first challenge is to develop a compatible waterproof coating to enable the sensors to operate underwater for a certain amount of time, e.g., one month. The second challenge is to minimize the sensors' pressure crosstalk. This is not a very serious problem for aerial applications since the air pressure does not vary a lot in most cases. However, the water pressure exerted on the sensor can change significantly, e.g., as during a submarine dive. Another big concern is the packaging, which is the bottleneck for most MEMS applications. Wire bonding on the front side has been ruled out since this is not reliable and will introduce the flow disturbance. We proposed a novel package scheme based on the flexible skin structure as shown in Figure 3.2. By this method, the metal leads can get to the backside of the plug through the slit. Then we can do wire bonding or soldering on the backside conveniently. Therefore, the MEMS skin technology not only makes it possible for the sensors to be mounted on nonplanar surfaces for distributed sensing, but also provides a novel packaging approach.

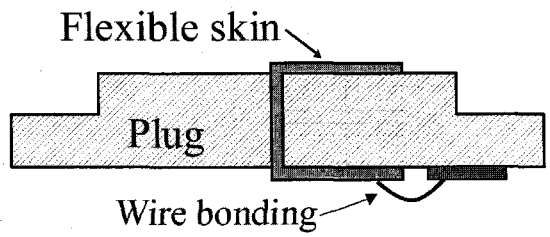

Figure 3.2 Schematic of the package scheme based on the skin structure.

3.2 Waterproof coating

For waterproof coating, low temperature oxide (LTO) was originally investigated, but then abandoned because the sensors will be integrated onto flexible skins eventually for packaging purpose and tests show that LTO cracks easily breaking metal wires on it when the skin undergoes bending. Then, Parylene was investigated and proved to be a satisfactory waterproof material. Parylene is the generic name for members of unique family of thermoplastic polymers that are CVD-deposited by sublimating a dimer of para-xylylene (di-para-xylylene, or DPXN). It is flexible, resistant to water transmittance, and easily CVD-deposited at room temperature [7]. Table 1 compares the moisture vapor transmission rates of Parylene N, C, D (which are the three most frequently used Parylenes) and other polymers [7]. For other properties of Parylene, please refer to next chapter and [7, 8].

Polymer	Moisture Vapor Transmission at 90% RH, 37°C, (g•mil/100 in^2•day)
Parylene N	1.5
Parylene C	0.21
Parylene D	0.25
Epoxides	1.79 - 2.38
Silicones	4.4 - 7.9
Urethanes	2.4 – 8.7

Table 3.1 Moisture vapor transmission rates of different polymers[7].

Underwater tests show that, when operated at 55°C, sensors coated with 2 μm Parylene N can survive in water at least for one month. Longer surviving time is expected with Parylene C, which has even smaller moisture vapor transmission rate.

3.3 Pressure sensitivity analysis

The vacuum cavity underneath provides excellent thermal isolation. However, pressure crosstalk is also introduced. When the pressure of the ambient fluid varies, it changes the strain on the nitride diaphragm. The polysilicon resistor (Figure 3.1) is also well known as a strain gauge. If there is strain change on the diaphragm, the relative resistance change can be expressed as

$$\Delta R / R = G_l < \varepsilon_l > + G_t < \varepsilon_t > \tag{3.1}$$

$<\varepsilon_l>$: average longitudinal strain

$<\varepsilon_t>$: average transverse strain

G_l: longitudinal gauge factor of polysilicon

G_t: transverse gauge factor of polysilicon

The longitudinal and transverse gauge factors of polysilicon are already known [9]. To calculate the resistance change, we need to know the average longitudinal and transverse strains. The calculation of strain distribution on the nitride diaphragm is a challenging problem due to the step-up anchor and bird's beak of the diaphragm as shown in Figure 3.3 [10]. The step-up anchor is formed by the boundary of the PSG and the bird's beak is caused by the lateral oxidation during LOCOS process. In addition, the intrinsic stress of SiN makes the problem even more challenging.

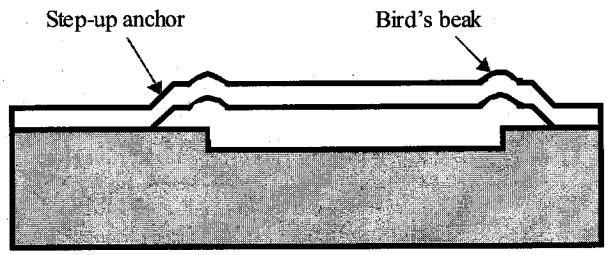

Figure 3.3 Cross section of the real diaphragm (not to scale).

A first-order approximation can be obtained using a flat rectangular diaphragm with clamped edges and zero initial stress as an analytical model.

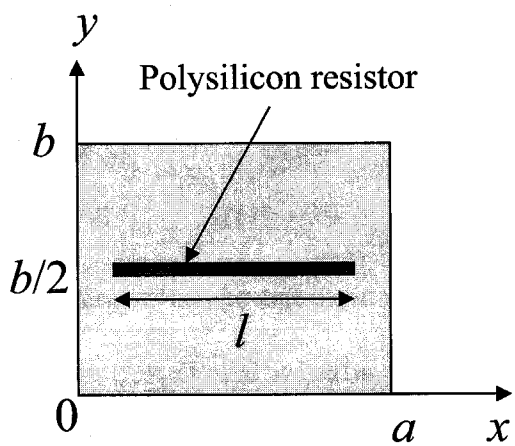

Figure 3.4 The coordinate system.

The deflection of the diaphragm can be found by solving the following fourth-order differential equation taking the coordinate axes as shown in Figure 3.4 [11]:

$$\frac{\partial^4 w}{\partial x^4}+2\frac{\partial^4 w}{\partial x^2 \partial y^2}+\frac{\partial^4 w}{\partial y^4}=\frac{p}{D}, \tag{3.2}$$

where $w(x,y)$ is the displacement of the middle plane; p is the pressure applied; and D denotes $Eh^3/12(1-\nu^2)$ and is called the flexural rigidity of the plate. The boundary conditions are as follow

$$w\big|_{x=0,a}=0 \qquad \left.\frac{\partial w}{\partial x}\right|_{x=0,a}=0$$
$$w\big|_{y=0,b}=0 \qquad \left.\frac{\partial w}{\partial y}\right|_{y=0,b}=0 \tag{3.3}$$

These boundary conditions are satisfied if we assume w in the following form:

$$w=\sum_{m=1}^{\infty}\sum_{n=1}^{\infty}A_{mn}(1-\cos\frac{2m\pi x}{a})(1-\cos\frac{2n\pi y}{b}), \tag{3.4}$$

where the parameters A_{mn} are to be determined by means of Rayleigh-Ritz methods, i.e., the potential energy of the system

$$\Pi=U-W \tag{3.5}$$

is a minimum with respect to these parameters. Namely, we have the following conditions for various m and n:

$$\partial\Pi/\partial A_{mn}=0 \tag{3.6}$$

The bending-strain energy U can be expressed as

$$U=\frac{D}{2}\iint_{A}(\frac{\partial^2 w}{\partial x^2}+\frac{\partial^2 w}{\partial y^2})^2\,dxdy \tag{3.7}$$

and the potential energy of the external force is

$$W=\iint_{A}pw dxdy \tag{3.8}$$

Then by using Eq.(3.6) for various values of m and n, we can obtain same number of equations for A_{mn} as the number of parameters taken. Once w is know, the strain distribution on the top surface can be calculated by

$$\varepsilon_x(x,y)=\frac{h}{2}\frac{\partial^2 w}{\partial x^2}=\frac{2\pi^2 h}{a^2}\sum_{m=1}^{\infty}\sum_{n=1}^{\infty}A_{mn}m^2\cos\frac{2m\pi x}{a}(1-\cos\frac{2n\pi y}{b}) \tag{3.9}$$

$$\varepsilon_y(x,y) = \frac{h}{2}\frac{\partial^2 w}{\partial y^2} = \frac{2\pi^2 h}{b^2}\sum_{m=1}^{\infty}\sum_{n=1}^{\infty} A_{mn} n^2 \cos\frac{2n\pi x}{b}(1-\cos\frac{2m\pi y}{a}), \qquad (3.10)$$

where h is the thickness of the diaphragm. The average strains can be calculated with

$$<\varepsilon_l> = \frac{1}{l}\int_{(a-l)/2}^{(a+l)/2} \varepsilon_x(x,y)\Big|_{y=0.5b} dx \qquad (3.11)$$

$$<\varepsilon_t> = \frac{1}{l}\int_{(a-l)/2}^{(a+l)/2} \varepsilon_y(x,y)\Big|_{y=0.5b} dx \qquad (3.12)$$

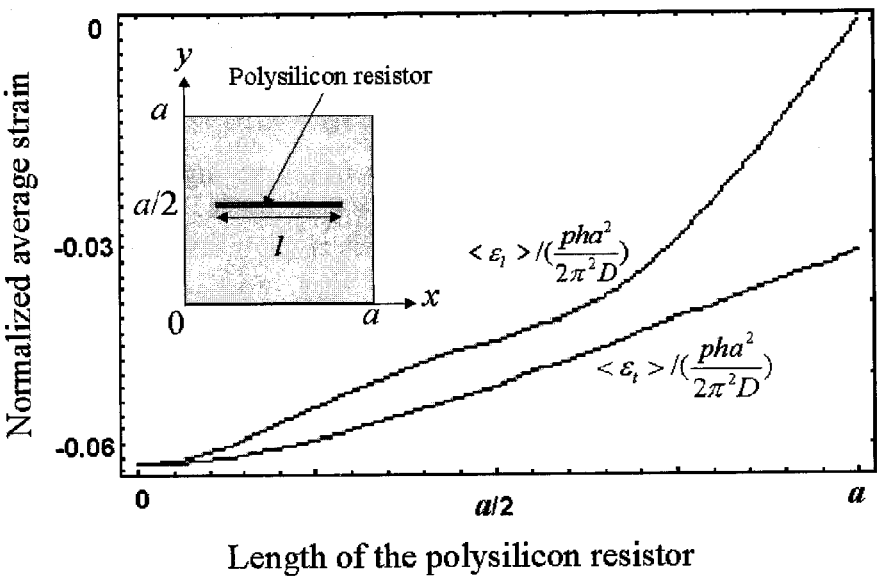

Figure 3.5 Normalized average longitudinal and transverse strains.

If the parameters A_{mn} are known, $<\varepsilon_l>$ and $<\varepsilon_t>$ can be readily calculated. Let's examine the case of a square diaphragm (a=b). It would be accurate enough to only consider A_{11}, A_{12}, A_{21}, A_{22}, A_{13}, A_3, and A_{33} with which seven equations can be generated based on Eq.(3.6). The solution of the equations gives the following results:

A_{11}=0.11774p' A_{12}=A_{21}=0.01184p'

A_{22}=0.00189p' A_{13}=A_{31}=0.00268p'

A_{33}=0.00020p'

where $p' = pa^4 / 4D\pi^4$. Based on these values, Figure 3.5 illustrates the normalized average strain for a square diaphragm. It is found that $<\varepsilon_t>$ is always negative and $<\varepsilon_l>$ approaches zero when the resistor length approaches a. At the same time, the longitudinal gauge factor G_l of polysilicon is positive while the transverse gauge factor G_t is negative [9]. Therefore the longitudinal and transverse terms of Eq.(3.1) can cancel with each other by varying the length of the polysilicon resistor. Theoretically, the pressure sensitivity could be completely eliminated using the same diaphragm dimensions as the aerial design. Figure 3.6 shows the calculated resistance change as a function of the polysilicon resistor length on a 210 × 210 × 4 μm^3 diaphragm with 10 psi pressure change. The pressure sensitivity is zero when l=190.6 μm. Shown in Table 3.2 are the parameters used in the calculation. Note that the length which achieves zero pressure sensitivity is also a function of the ratio between G_l and G_t.

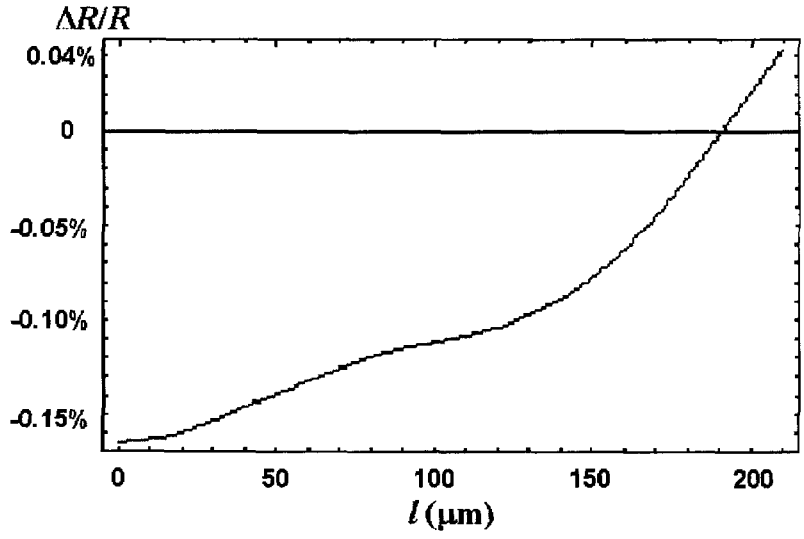

Figure 3.6 Theoretical relative resistance change as a function of polysilicon resistor length.

Parameters	Values
Pressure change Δp	10 psi
Square diaphragm length a	210 μm
Diaphragm thickness h	4 μm
Young's modulus of diaphragm G	260 Gpa
Poisson's ratio ν	0.25
Longitudinal gauge factor G_l	30
Transverse gauge factor G_t	-10

Table 3.2 Parameters used in the calculation of Figure 3.6

However, the actual situation is much more complicated than the analytical model. Figure 3.7 shows the measured pressure sensitivity data of 4 identical aerial shear-stress sensors with square diaphragms ($210 \times 210 \times 1.6\ \mu m^3$). These four sensors, which have identical parameters such as diaphragm dimension and resistor length, were expected to have same behaviors. However, as shown in Figure 3.7, their pressure sensitivities vary considerably. There are a lot of factors contributing to the large fluctuation of pressure sensitivity. Among them, the dimension of the diaphragm is believed to play a key role.

For the underwater shear-stress sensor, we decided to use smaller and thicker diaphragms. The biggest benefit is that the uncompensated strain, due to the model error or imperfect process control (e.g., the resistor position offset), will be significantly reduced with a stiffer diaphragm. Moreover, the touchdown pressure of the diaphragm will be much higher so that the operation range of the shear-stress sensor can be extended

considerably. The disadvantages, however, are more conductive heat loss to substrate and smaller shear-stress sensitivity.

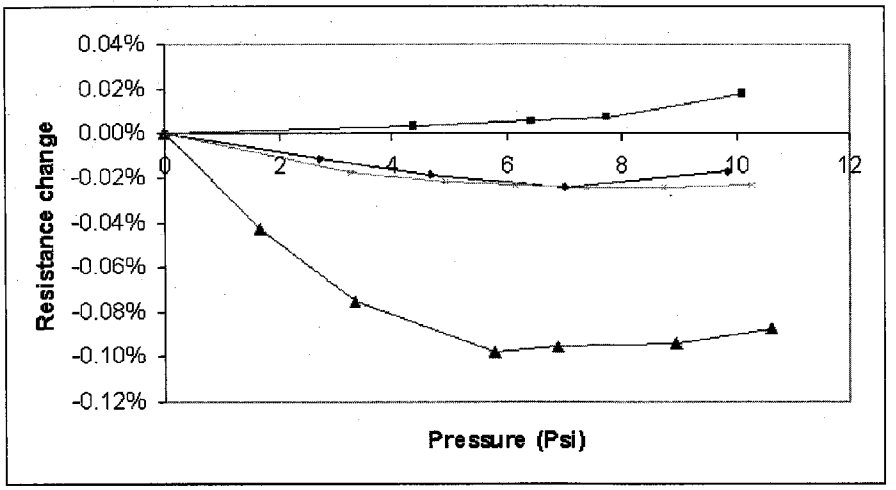

Figure 3.7 Measured resistance change of four identical shear-stress sensors (a=b=210 μm, t=1.6 μm).

3.5 Design and fabrication

Based on the experimental results of the aerial shear-stress sensors, we conclude that the diaphragm size has to be decreased and that the thickness has to be increased for underwater applications. Table 3.3 lists various sensor designs implemented in the underwater shear-stress sensor skin. There are mainly two groups of sensors. The first group (#1, #2, #3) has various resistor lengths across the diaphragm. The second group (#3 ~ #7) has various diaphragm widths from 210 μm to 45 μm. For all the designs, the thickness is chosen as 4 μm in order to make the diaphragm rigid enough but not to cause too much trouble during the fabrication process. For comparison, a = b = 210 μm and h=1.6 μm for the aerial sensor. This, however, leads to more heat loss to substrate, and decreases the shear-stress sensitivity. A comparative study of the effect of diaphragm

dimensions will be presented in the following sections, which has not been addressed systematically before. A temperature sensor is integrated for temperature compensation while a pressure sensor is also included in case pressure compensation is needed.

Sensors	a (μm)	b (μm)	l (μm)
#1	210	210	210
#2	210	210	196
#3	210	210	180
#4	210	150	180
#5	210	100	180
#6	210	75	180
#7	210	45	180

Table 3.3 Different sensor designs implemented.

The fabrication process consists of two parts, namely, the fabrication of shear-stress sensors and the fabrication of skin structures. As shown in Figure 3.8, the process starts with the deposition and patterning of low stress silicon nitride on silicon wafers. Windows are then etched further into silicon to obtain the desired depth. Thermal oxide is grown locally (LOCOS) on the trenches then the wafer is planarized by HF dip. After 0.4 μm phosphosilicate glass (PSG) is deposited, densified, patterned and annealed to form the etching channels for the cavity, about 1.5 μm of low stress nitride is deposited and patterned to open the etch holes. The PSG and thermal oxide are etched away by 48% HF to release the nitride diaphragms. After this, another nitride layer is deposited to reach the desired diaphragm thickness and the cavity is sealed as well. Next, 0.5 μm

polysilicon films are deposited, doped, annealed, and patterned to form the sensing resistors. The polysilicon films are actually doped twice. The first doping is a global boron ion implantation with a dose of $1 \times 10^{15}/cm^2$ to obtain a nearly zero temperature coefficient of resistance (TCR) for pressure sensors. The second doping is a selective high dose boron ion implantation ($1 \times 10^{16}/cm^2$) on the shear-stress and temperature sensors. The TCR of this heavily doped polysilicon is about 0.081%/°C. Next, another 0.2 μm nitride is deposited as a passivation layer. Note that now the total nitride thickness is approximately 4 μm and that it has to be thinned down before metalization. The reason and exact process are explained in the next paragraph. After this, the contact holes are opened and a 1.5 μm thick aluminum layer is sputtered, patterned, and sintered. At this point, the fabrication of the sensors is completed. Figure 3.9 shows the SEM picture of one shear-stress sensor and Figure 3.10 illustrates two rows of the seven different sensors. Note that the sensors are placed normal to each other in order to measure the direction as well as the shear stress of the flow.

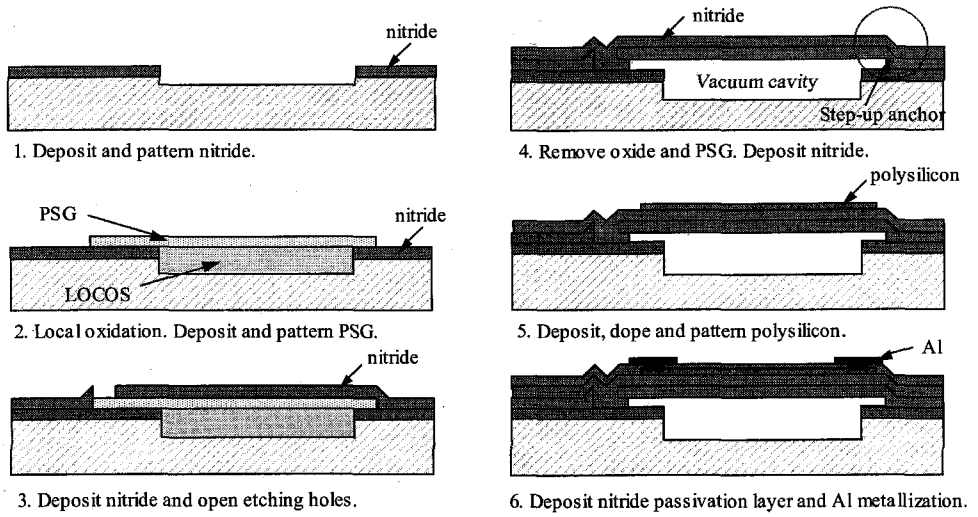

Figure 3.8 Simplified fabrication process of the shear-stress sensor.

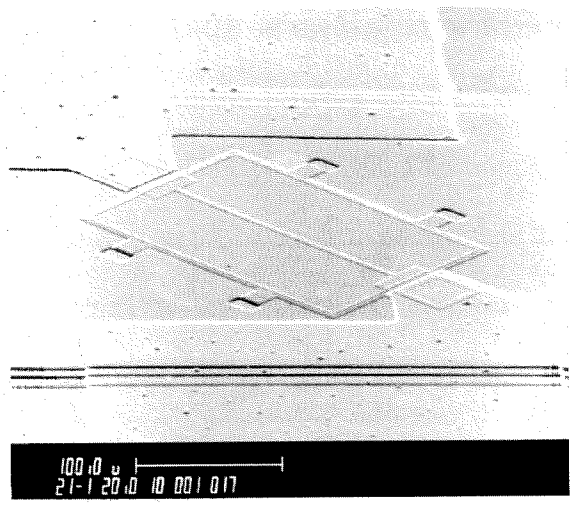

Figure 3.9 SEM picture of one shear-stress sensor (design #4 in Table 3.3).

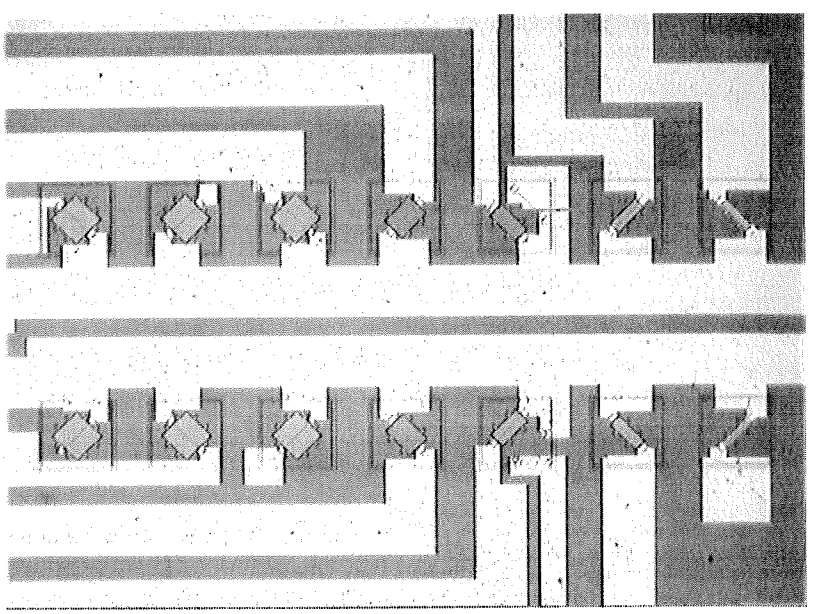

Figure 3.10 Two rows of sensors with different parameters.

The fabrication of skin structures begins with the coating of 6 μm polyimide on the front side. The polyimide is cured at 350°C and then patterned by oxygen plasma to expose the sensors. Next, the backside nitride is patterned and the bulk silicon is thinned

down to ~70 μm using DRIE. DRIE is used again to form the silicon islands by anisotropically etching away the silicon between islands. Note that further backside etching is needed to remove the nitride layer deposited on front side. After this, another layer of polyimide is spin-coated on the backside to encapsulate the silicon islands. Then the polyimide is wet-patterned by the photoresist developer (AZ 351) to expose the bonding pads. The last step is the curing of polyimide at 350°C. The detail of the skin structure is illustrated in Figure 3.11.

The fabrication process of underwater shear-stress sensor skin is very similar to the one of the aerial sensor skin described in Chapter 2. However, since very thick nitride is used, there are several modifications and some unique challenges. The first difference is that nitride is used to seal the cavity in vacuum instead of LTO (step 4 in Figure 3.8) and that there is no etch back. Due to the huge tensile stress, the nitride has to be thinned down before releasing from backside. Otherwise, the nitride will easily crack and break the aluminum wires on top of it. In this run, the front side nitride is thinned down to ~1 μm. However, nitride already cracks somewhere before the thinning down as shown in Figure 3.12. The cracked nitride, although thinned down, still breaks the aluminum wires after it is freed from backside. Therefore, considering the fact that the aluminum can not be deposited on silicon to avoid any short circuits, the following improved process is proposed: after patterning the polysilicon, nitride is completely etched away at areas where will be free standing; next, the 0.2 μm passivation nitride layer is deposited and serves as insulating layer between aluminum and silicon substrate as well; the remaining process keeps unchanged. When etching back the nitride, the step coverage issue during the aluminum metalization has to be considered. Namely, the

etching back cannot be carried out with one single mask. As shown in Figure 3.13, the three squares surrounding the sensor are the steps made by three consecutive etching backs.

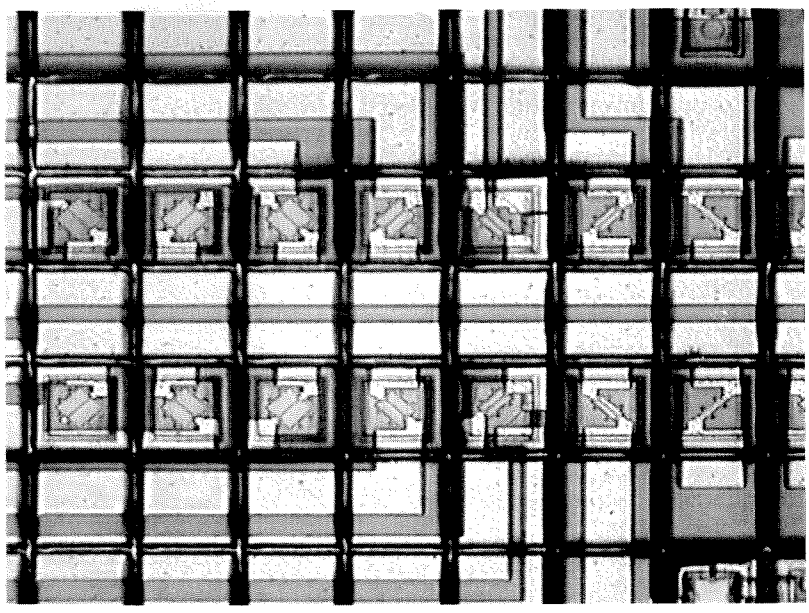

Figure 3.11 Two rows of shear-stress sensors on silicon islands.

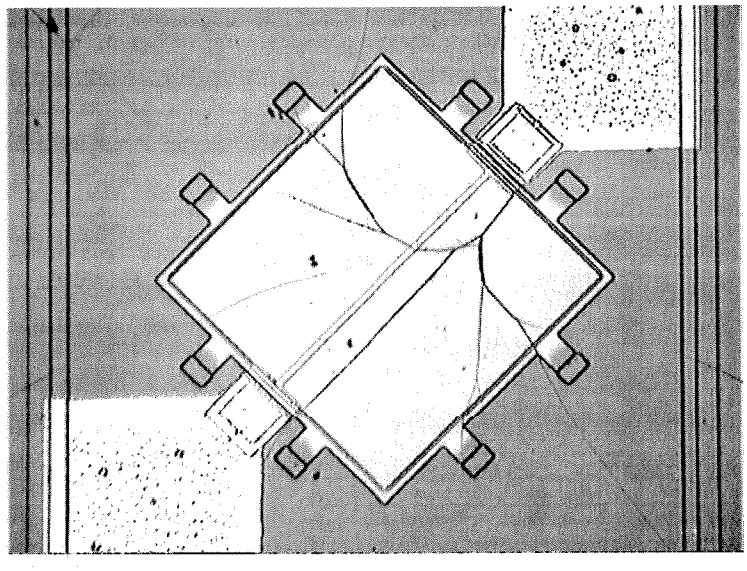

Figure 3.12 Cracked nitride diaphragm

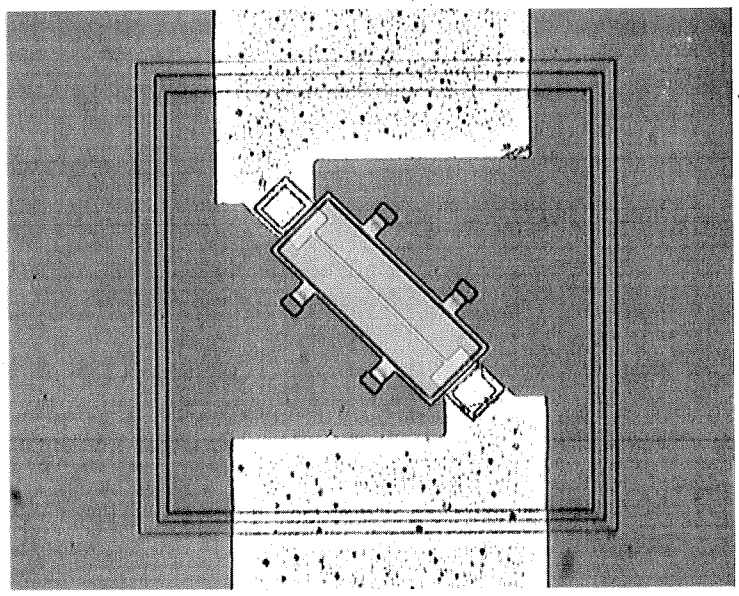

Figure 3.13 A sensor on the mesa formed by three nitride thinning-downs.

3.6 Testing and discussion

3.6.1 Static thermal characteristic

To characterize the performance of the underwater shear-stress sensor, we can perform the shear-stress calibration in a well-characterized water tunnel. On the other hand, we can obtain the temperature vs. power relationship at zero shear stress easily by performing an I-V curve measurement, provided the TCR of the sensing element. This static thermal characteristic measurement is very simple but provides valuable information on the performance of the shear-stress sensor.

For our sensors, the total heat loss includes conduction loss to substrate (q_1, q_2, q_3, and q_4) and convection loss to fluid (q_5) as shown in Figure 3.1. To achieve a high sensitivity, a larger q_5 is desired. A simple way to measure q5 is to perform the static temperature-power measurements in vacuum and fluid (air or water), respectively.

Assume that with and without fluids, the conduction loss (q_1, q_2, q_3, and q_4) remains unchanged[1], q_5 can be estimated by comparing the two curves. Figure 3.14 shows the static thermal characteristics of sensor #3 in vacuum, air and water respectively. In air, q_5 only accounts for ~5% of the total heat loss. In water, q_5 has much larger percentage (>45%), as expected. Figure 3.15 illustrates the static thermal characteristics of the five sensors (sensor #3~#7) in vacuum and water. It is observed that, as the diaphragm gets smaller, more power is needed to achieve the same temperature increase but that less heat is transferred to water (q_5). However, even for a 45 μm wide sensor, there is still more than 15% of the power transferred to water.

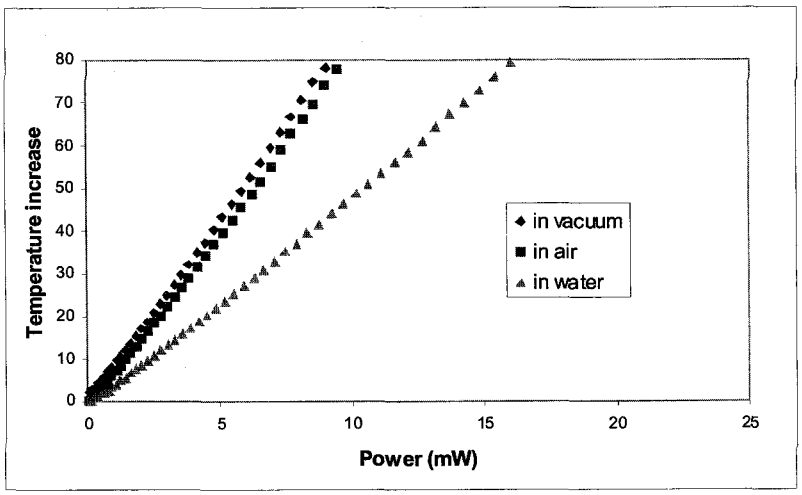

Figure 3.14 The static thermal characteristics of sensor #3 in vacuum, air, and water, respectively.

[1]The conduction loss to substrate when the sensor is in fluid actually will be smaller than the one in vacuum. There is some error to calculate q_5 by this method especially for water. More accurate value can be obtained by numerical simulation.

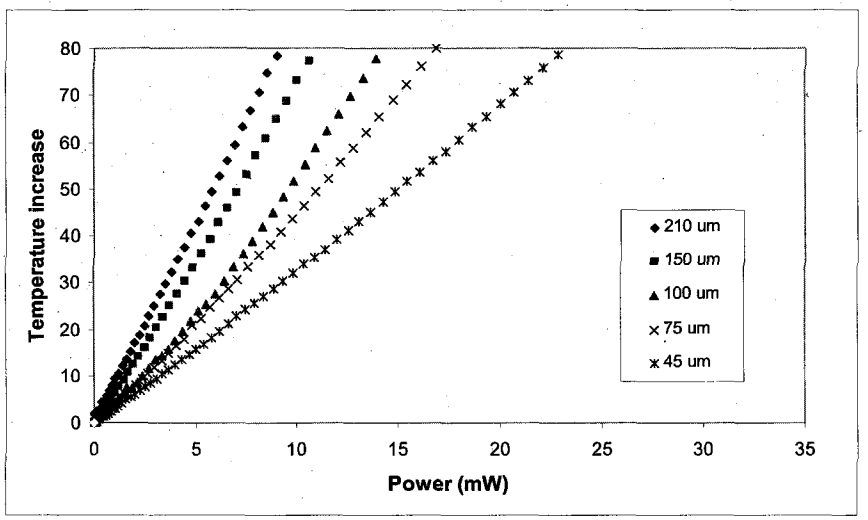

(a) Static thermal characteristics in vacuum.

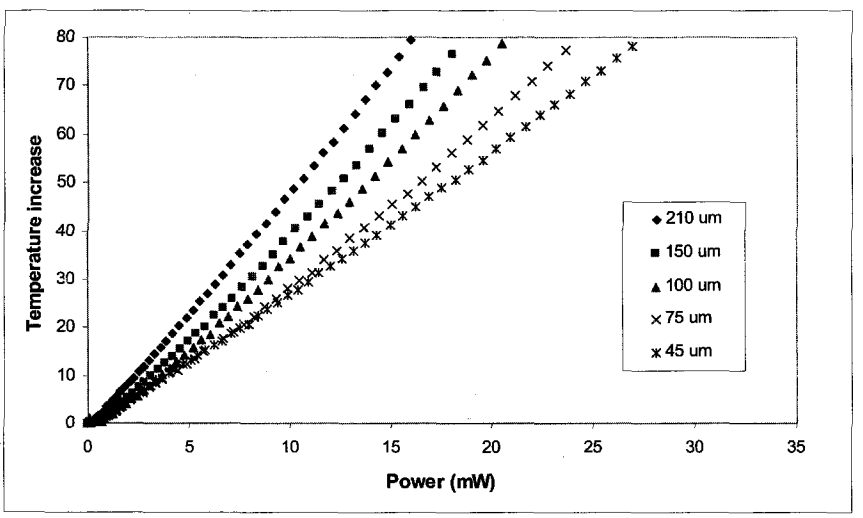

(b) Static thermal characteristics in water.

Figure 3.15 Static thermal characteristics of five sensors with different diaphragm widths.

3.6.2 Temperature sensitivity

The output of thermal shear-stress sensor is very sensitive to ambient temperature. The following figure shows the temperature sensitivities of four sensors with different diaphragm widths in CT mode. It is worth noting that in CT mode, we usually measure

the voltage of the operational amplifier. This is the amplified voltage (Figure 1.14) and in Figure 3.16, it is converted to the voltage across the sensing element. In the following discussions on shear-stress sensitivity, pressure sensitivity, the unamplified voltage will be used as well unless specified. It is observed that the temperature sensitivity is independent on the diaphragm width. A temperature sensitivity of 0.1V/°C is observed with 3% over-heat ratio.

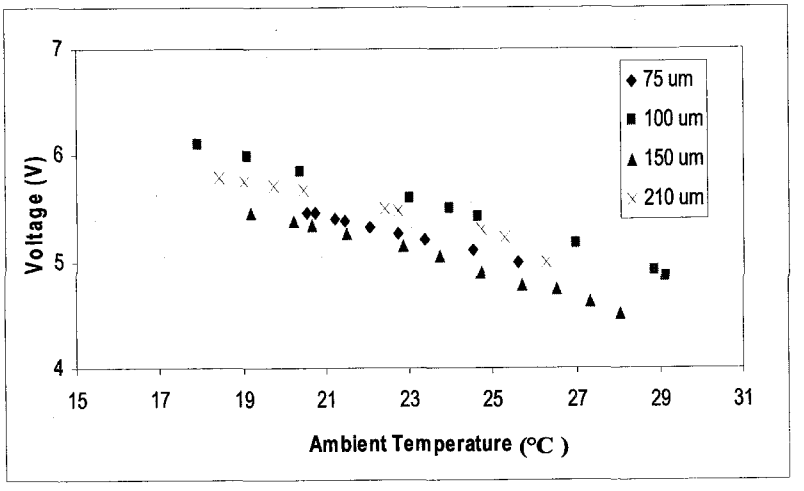

Figure 3.16 Measured temperature sensitivity of four different sensors in CT mode. An over-heat ratio of 3% is used and the voltage is the one across the sensing element.

3.6.3 Shear-stress calibration

The shear-tress calibration can be conducted in a well-characterized water tunnel. Here a simple alternative method is presented. As shown in Figure 3.17, the sensor chip is first bonded to a printed circuit board and then another channel chip (with the width w of 2.5 mm, height h of 0.3mm and length l of 18-mm) is flip-bonded on top of the sensor chip.

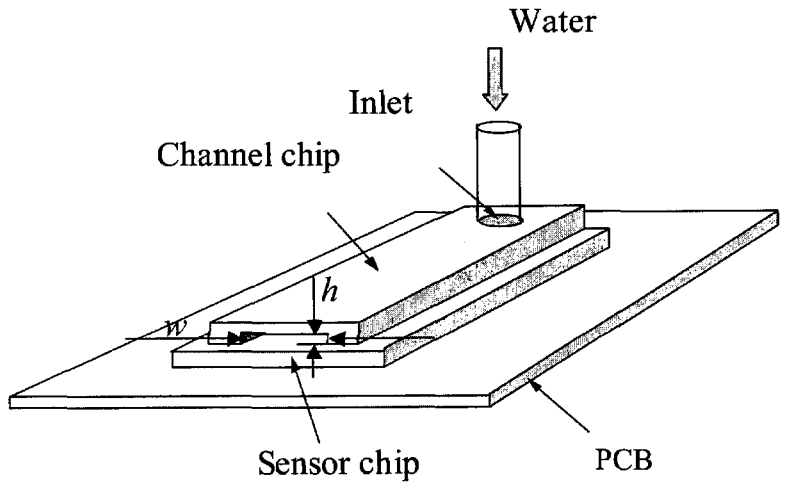

Figure 3.17 A simple setup for shear stress calibration.

For the fully developed rectangular channel flow, if the height h is much smaller than the width w, we can assume that the velocity profile is only a function of vertical position (y) and has a parabolic distribution (Figure 3.18)

$$u(y) = -\frac{4u_0}{h^2}(y - h/2)^2 + u_0, \tag{3.13}$$

where u_0 is the maximum velocity in the center of the channel.

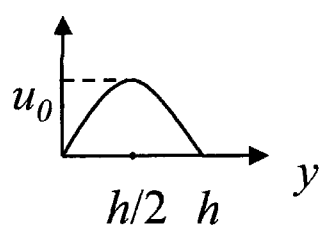

Figure 3.18 Velocity profile in the channel.

Based on this velocity profile, we have the flow rate

$$Q = \int_0^h u(y)wdy = \int_0^h (-\frac{4u_0}{h^2}(y - h/2)^2 + u_0)wdy = \frac{2}{3}wu_0h \tag{3.14}$$

According to the definition of shear stress

$$\tau = \mu \frac{du}{dy}|_{y=0} = \mu \frac{4u_0}{h} \tag{3.15}$$

Combining (3.14) and (3.15), we acquire the relationship between τ and Q:

$$\tau = \frac{6\mu}{h^2 w} Q \tag{3.16}$$

Therefore, the wall shear stress is readily known by measuring the flow rate Q. The above equation is for a channel with infinite large width. A more accurate solution for a rectangular channel with finite width can be obtained using the Fanning friction factor f [12]:

$$\tau' = \frac{1}{2} f \rho u_m^2, \tag{3.17}$$

where u_m is the average velocity and is defined as flow rate divided by area of cross section

$$u_m = Q/(h \times w) \tag{3.18}$$

The Fanning friction factor f can be expressed as

$$f = 16\phi(n)/\mathrm{Re}_h, \tag{3.19}$$

where Re_h is the Reynolds number based on the hydraulic diameter D_h

$$\mathrm{Re}_h = \frac{\rho u_m D_h}{\mu} \tag{3.20}$$

and $\phi(n)$ is a correcting factor based on the ratio of h/w as shown in Figure 3.19.

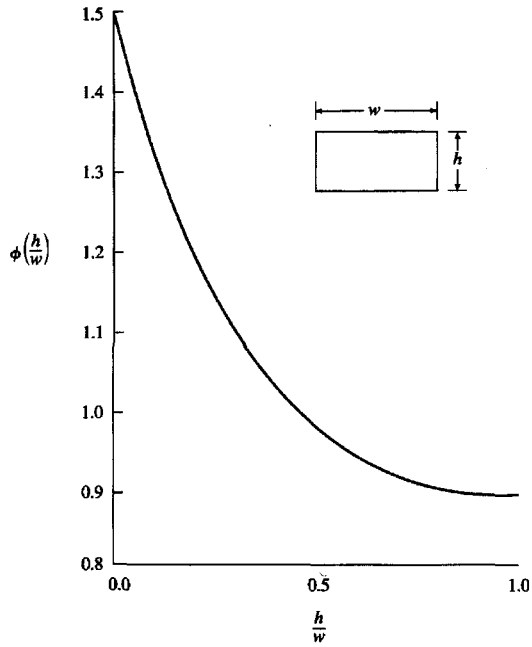

Figure 3.19 $\phi(h/w)$ for rectangular channels [12]

The hydraulic diameter is defined as

$$D_h = 4 \times \text{cross-section area / wetted perimeter} = 4(h \times w)/(2h + 2w) \tag{3.21}$$

Finally, we have

$$\tau' = \frac{1}{2} 16\phi(n)\rho u_m^2 \frac{\mu}{\rho u_m D_h} = 8\phi(n)\frac{\mu Q}{D_h A} \tag{3.22}$$

For our channel, h=0.3mm, w=2.5mm, $\phi(n) \approx 1.31$. Dividing Equation (3.22) by (3.16), we have

$$\frac{\tau'}{\tau} = \frac{2}{3}\phi(n)\frac{h+w}{w} \tag{3.23}$$

Plugging in all the numbers, we find that $\tau' = 0.978\tau$. Therefore, there is no big difference using Equation (3.22) or (3.16) in our case.

In order to calculate the wall shear stress based on the flow rate, the sensor has to be in the fully developed regime. The length of the channel from the inlet to the point where the flow reaches the fully developed velocity profile is generally known as the entrance length. Therefore the distance between sensors and channel inlet should be larger than the entrance length. The entrance length for rectangular channel can be estimated from the following expression [12]

$$x_e / D_h \approx 0.25 + 0.015 \mathrm{Re}_h, \text{ for aspect ratio} \geq 2. \tag{3.24}$$

The maximum flow rate used in the calibration is 12.0 ccm. Table 3.4 lists some parameters calculated at the maximum flow rate. The density ρ and viscosity μ of water at 20°C are 998.2 kg/m^3 and 9.93×10^{-4} Pa·s, respectively. For our setup, the distance between the first sensor and the inlet is ~6 mm, which is much larger than the entrance length of 1.29 mm. In addition, the Reynolds number is only 144. We conclude that all the sensors being tested are in the fully developed laminar flow region.

U_m	0.267 m/second
D_h	0.5357 mm
Re_h	144
x_e	1.29 mm

Table 3.4 Some parameters at maximum flow rate (12 ccm).

Another factor which affects the calibration is the thermal boundary layer thickness. It should be less than the channel height in order to avoid the disturbance of the channel. The thermal boundary layer is given by [13]

$$\delta / (W/2) = 0.34 \bar{\tau}^{-1/3} \tag{3.25}$$

In the above expression, $\bar{\tau} = \tau(W/2)^2 / \mu\alpha$ and α is the thermal diffusivity of water. Figure 3.20 plots the relationship between $\delta(W/2)$ and τ. Note that W/2 for the largest diaphragm is only 105 μm and the channel height is 300 μm. Therefore, in most cases, the thermal boundary layer thickness is less than channel height. There might be some slight disturbance when τ approaches zero.

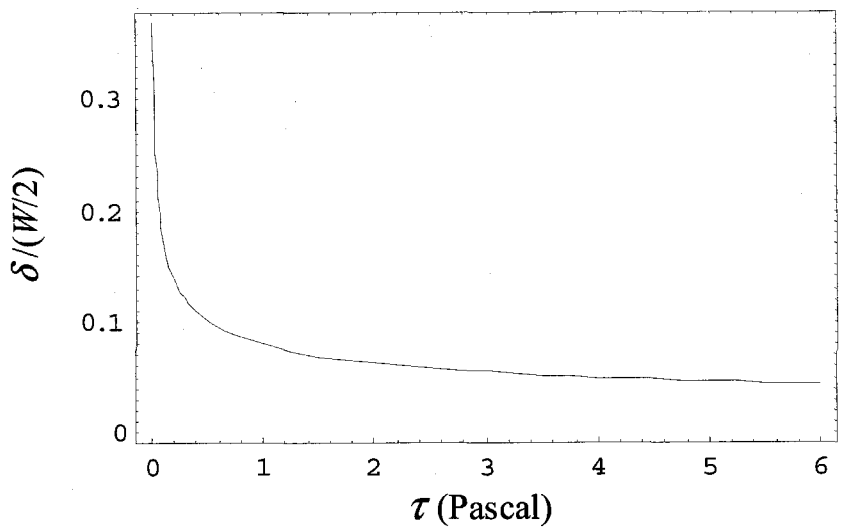

Figure 3.20 The relationship between thermal boundary layer thickness and shear stress.

Shown in Figure 3.21 are the shear-stress calibration data of four sensors (#3, #4, #5 and #6) with various diaphragm widths (75μm, 100μm, 150μm and 210μm). All the sensors operate in constant temperature mode with a working temperature 35°C above ambient water (about 3% over-heat ratio). As expected, the sensors with larger diaphragm have higher shear-stress sensitivity. Note that the sensors are 45 ° to the flow direction during the calibration. If we assume the sensors' directional sensitivity follows a cosine law [14], then the maximum sensitivity, when the sensing element is normal to the flow, will be $\sqrt{2}$ times larger than what we achieved now.

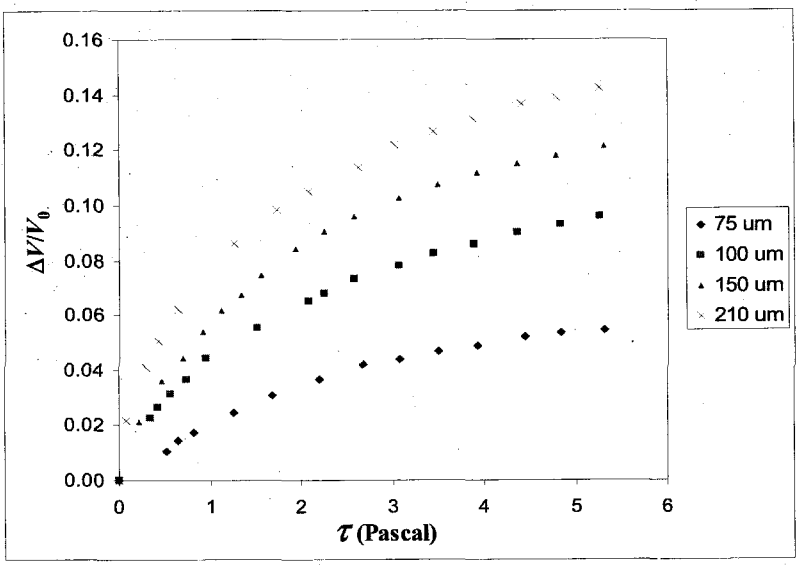

Figure 3.21 Normalized output voltage changes of four different sensors as functions of shear stress (sensors are 45° to the flow direction).

Sensors	75 μm	100 μm	150 μm	210 μm
Sensitivity (mV/Pascal)	110	273	252	395

Table 3.5 Average sensitivity between 0 and 1 Pascal in terms of mV/Pascal. The sensitivity is based on the nonamplified voltage output across the sensing element[2]. Also note that this sensitivity is obtained when the angle between sensing element and flow is 45 °.

Table 3.5 lists the average shear-stress sensitivity between 0 and 1 Pascal in terms of Volts/Pascal. Note that 150 μm sensor's sensitivity is lower than that of 100 μm sensor. This is not surprising after considering the fact that the sensitivity in terms of Volts/Pascal is also affected by the resistance of the sensing element as illustrated in Eq. (1.2). It is possible that the sensor with small diaphragm has higher voltage sensitivity

[2] In terms of the operational amplifier output, the sensitivity is $(R_2 + R_3)/R_3$ times higher. Refer to the CT circuit shown in Figure 1.14 in Chapter 1 for details.

simply because it has larger resistance. This problem can be solved by normalizing the output voltage change (ΔV) to the voltage with zero shear stress (V_0) (Appendix). When comparing sensors with different thermal characteristics, it is more generic to use power instead of voltage as output. The power data solely reflect the sensor's performance based on the thermal characteristics. While the voltage data reflect combination effects of thermal and electrical characteristics. Figure 3.22 re-plots the calibration curves converting output from voltage to power. Table 3.6 lists the average shear-stress sensitivity between 0 and 1 Pascal in terms of Watts/Pascal. The resistance of the shear-stress sensor is another independent degree of freedom to adjust the sensitivity[3].

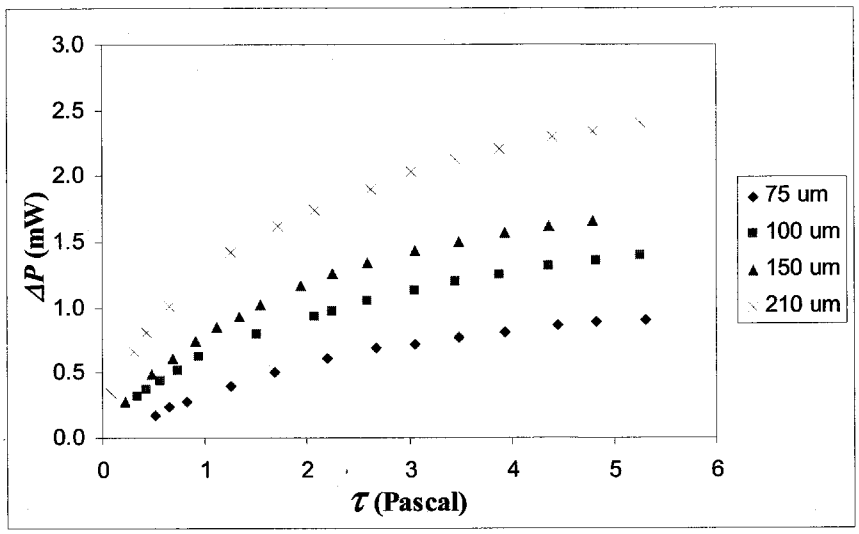

Figure 3.22 The power change vs. shear stress.

[3] When changing the resistance of the sensing element, the physical dimension of the sensor will change slightly. However this is a second-order effect which is negligible. Therefore it is valid to assume that the heat transfer characteristic will not change when varying the resistance of the sensing element.

Sensors	75 μm	100 μm	150 μm	210 μm
Sensitivity (mW/Pascal)	0.32	0.66	0.76	1.13

Table 3.6 Average sensitivity between 0 and 1 Pascal in term of mW/Pascal.

3.6.4 Pressure sensitivity

The results of pressure sensitivity measurement of sensors in group two (#3 ~ #7 in Table 3.3) are illustrated in Figure 3.23. It is observed that the resistance change of the 210 μm sensor is negative and as the diaphragm width decreases, the slope gets closer to zero. The 75 μm sensor exhibits minimum pressure sensitivity. The 45 μm sensor shows positive resistance change, which is due to the dominance of the transverse strain when b is much smaller than a.

Figure 3.23 only depicts the effect of diaphragm dimension on pressure sensitivity. There is another independent degree of freedom that we can adjust to minimize the pressure sensitivity, which is the resistor length across the diaphragm. Figure 3.24 shows the pressure sensitivity of three sensors with same diaphragm dimensions (210 × 210 ×4 μm^3) but various resistor lengths (180 μm, 196 μm and 210 μm). It is very interesting to notice that the resistance change is almost zero when the resistor length is 210 μm. Based on Figure 3.24, the theoretical curve illustrated in Figure 3.6 should be shifted downward. This could be caused by the nonideal boundary condition, bird's beak, the intrinsic stress of nitride, or the inaccuracy of the gauge factors we used.

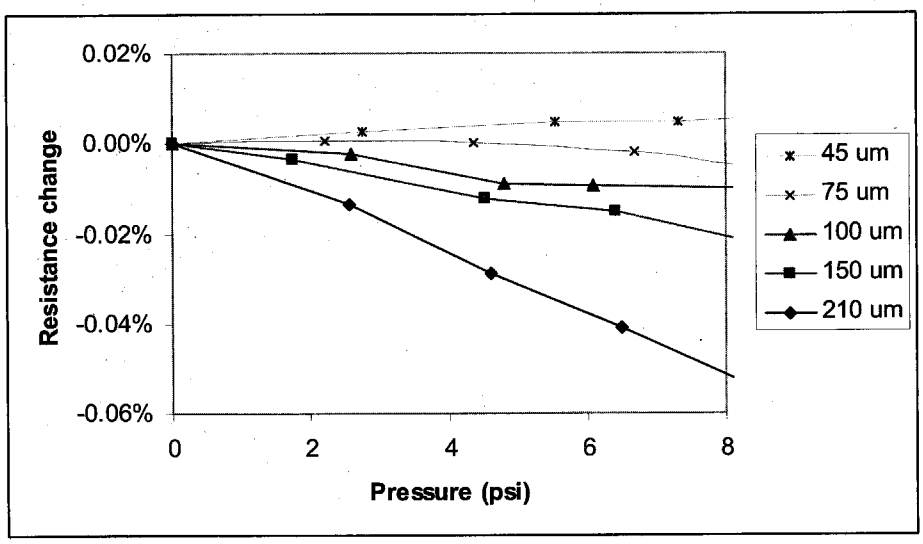

Figure 3.23 Resistance changes of sensors with different diaphragm widths.

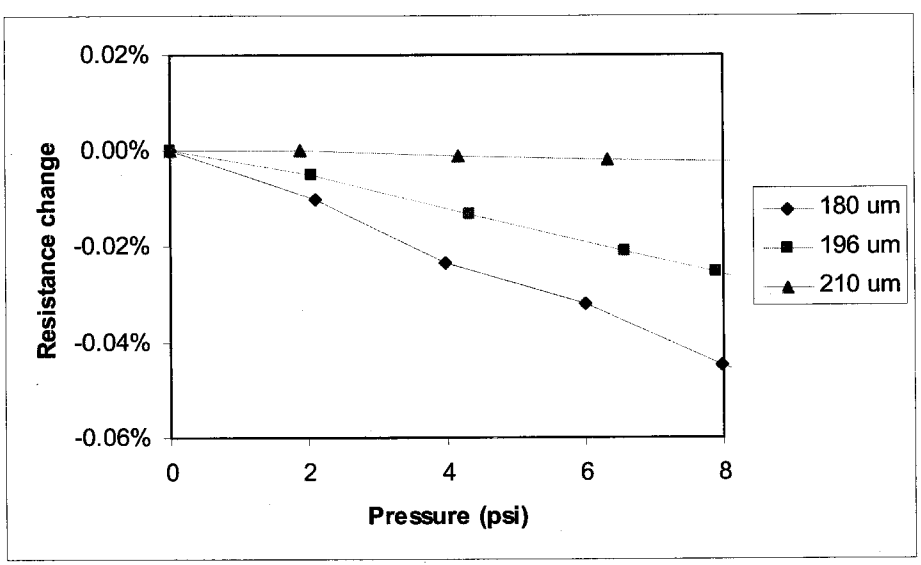

Figure 3.24 Resistance changes of sensors with different sensing element lengths.

The pressure sensitivities shown in above figures are expressed in terms of resistance change. But during the real operation, the pressure sensitivity exhibits in the form of voltage change. Like the TCR, we can also define pressure coefficient of

resistance (PCR). Therefore, we have the following expression for the resistance of the sensing element:

$$R = R_0(1+\alpha_T \Delta T + \alpha_P \Delta P), \tag{3.26}$$

where α_P is the PCR. When operating at CT mode, the negative feedback circuit actually keeps the resistance of sensing element constant[4]. When there is ΔR caused by pressure change, the temperature must change in opposite direction to compensate this change, i.e.,

$$\Delta T' = -\frac{\alpha_P}{\alpha_T}\Delta P \tag{3.27}$$

We use $\Delta T'$ to denote this temperature change to distinguish it from the temperature difference between sensor and ambient fluid. The input power of the sensor can be expressed as

$$\frac{V^2}{R} = (A(\rho\tau)^{1/n} + B)\Delta T = C\Delta T, \tag{3.28}$$

where C is a constant in this case. When there is temperature change induced by pressure change, we have

$$\frac{(V+\Delta V)^2}{R} = C(\Delta T + \Delta T') \tag{3.29}$$

Neglecting the ΔV^2 term, we have

$$\frac{2V\Delta V}{R} = C\Delta T' = -C\frac{\alpha_P}{\alpha_T}\Delta P \tag{3.30}$$

We have $C = V^2/R\Delta T$ from Eq. (3.28), therefore

---

[4] In this sense, the CT mode is more appropriately named as constant resistance (CR) mode.

$$\Delta V = -\frac{V}{2\alpha_T \Delta T}\alpha_P \Delta P \tag{3.31}$$

The above expression can be further simplified since $\alpha_T \Delta T$ is the resistance over-heat ratio A_R (Eq. (1.4) in Chapter 1) and $\alpha_P \Delta P$ is the resistance change introduced by pressure $(\Delta R/R)_P$

$$\Delta V = -\frac{V}{2A_R}(\Delta R/R)_P \tag{3.32}$$

The over-heat ratio turns out to be a crucial operation parameter. From Eq. (3.32), we can see that the pressure sensitivity is inversely proportional to the over-heat ratio. The over-heat ratio can be increased so that the shear-stress sensitivity increases while the pressure sensitivity decreases. However, the operating temperature cannot be too high in order to avoid the bubble generation in the water. For underwater applications, an over-heat ratio of 3% is usually used. This is another reason that the pressure crosstalk for aerial applications is not so serious as underwater ones since the over-heat ratio for aerial applications could be relatively large, e.g., 20%.

We measured one sensor (design #3, 210 μm wide diaphragm, 180 μm long sensing element) with a resistance change rate of 0.0051%/psi. When operating at 3% over-heat ratio in CT mode, the output voltage (across sensing element) is 5.2 V and the sensor should exhibit a pressure sensitivity of 4.4 mV/psi theoretically according to Eq. (3.32). The actual experiment shows a sensitivity of 5.1 mV/psi, which is very close to the theoretical value.

In the case of CC mode, the voltage change is simply

$$\Delta V = V(\Delta R/R)_p \tag{3.33}$$

In the CC mode, the pressure sensitivity is independent of over-heat ratio[5].

The ratio between the pressure sensitivities at CT mode and CC mode is

$$\frac{\Delta V_{CT}}{\Delta V_{CC}} = 1/2A_T \tag{3.34}$$

We know that the shear-stress sensitivity in CT mode is much higher than that in CC mode. However, what matters is the signal-to-noise ratio. Therefore Eq. (3.34) can be used as a criterion to decide whether CT mode or CC mode should be used at certain over-heat ratio. For example, assume the shear-stress sensitivity of CT mode is 10 times higher than that of CC mode. If the over-heat ratio is 3%, then the pressure sensitivity of CT mode is 16.7 times higher than that of CC mode. Therefore the signal-to-noise ratio of CC mode is higher than that of CT mode in this case.

There are many other possible ways to improve the sensor accuracy besides using the on-chip pressure sensor to perform pressure compensation. For example, we can increase the operating temperature of the sensor so that the shear-stress sensitivity will increase while the pressure sensitivity will decrease in CT mode. In terms of fabrication, the sensing element (polysilicon resistor) can be buried in the middle plane of the nitride diaphragm in the cost of making the contact-hole opening process more complicated. Examining Eq. (1), it is clear that the gauge factor of polysilicon contributes considerably to the pressure sensitivity. Therefore, it is of great interest to use metal (e.g., platinum), whose gauge factor is much smaller, as the heating element. However, one disadvantage is the low resistivity of metal, which can lead to small output voltage.

---

[5] The gauge factor of polysilicon is a function of temperature. But this is negligible if the temperature change is not very large.

3.6.5 Time constant measurement

The time constant reflects the dynamic behavior of the shear-stress sensors, which is very important to turbulent flow measurement. The time constant can be measured using the circuit shown in following figure. Basically, a square wave signal is superimposed on the shear-stress sensor biased with current source. Following the input voltage step, there is transient increase or decrease of the output voltage. The time constant is estimated as the time required for the output to reach 63% ($\approx 1-e^{-1}$) of its total change as shown schematically in Figure 3.25. Table 3.7 summarizes the time constants measured of sensors with different diaphragm widths. There are two trends that can be clearly observed. First, the time constant decreases as the diaphragm width decreases. Second, the time constant in water is smaller than the one in air.

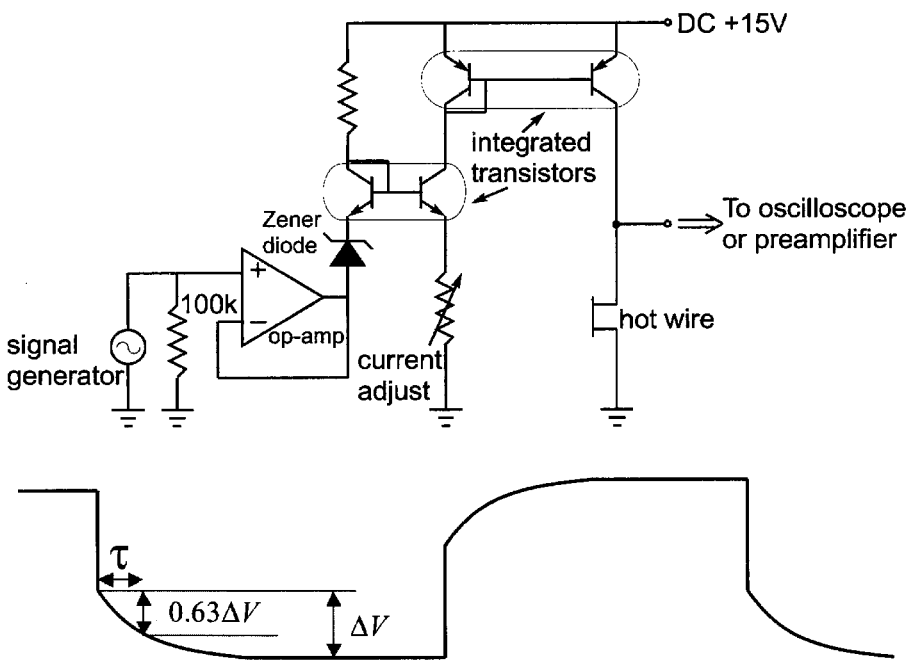

Figure 3.25 The circuits for time constant measurement and the square wave response of the output voltage [15].

Sensors	τ in air (ms)	τ in water (ms)
210 μm	1.2	0.30
100 μm	0.43	0.21
45 μm	0.17	0.10

Table 3.7 Time constants of sensors with different diaphragm widths.

3.7 Selective Parylene coating

For this underwater shear-stress sensor, Parylene is vapor phased deposited on the surface as waterproof coatings. This waterproof layer, on the other hand, retards the convective heat transfer from the sensor to water and therefore reduces the shear-stress sensitivity. Shown in the figure below are the static thermal characteristics of the same sensor coated with Parylene layers with different thickness. It can be observed that for thicker Parylene, less power is dissipated to water.

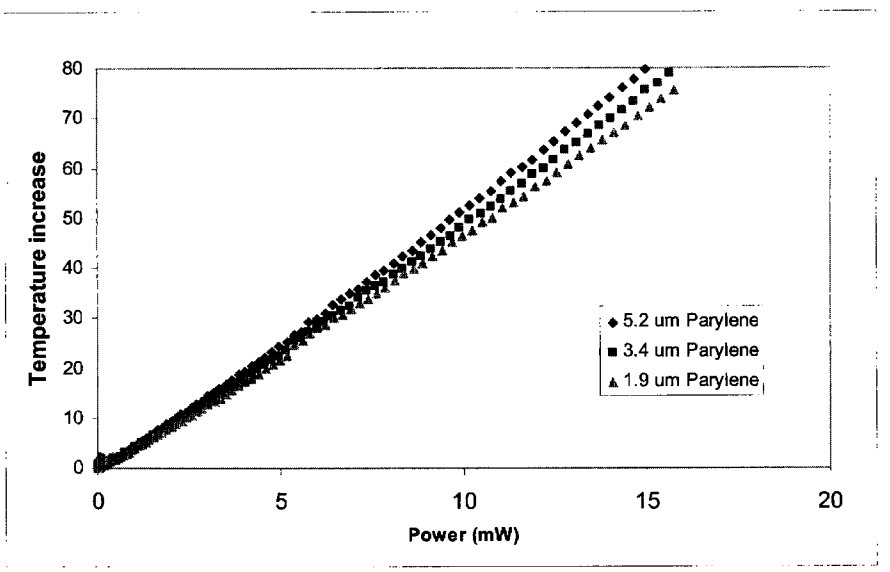

Figure 3.26 Static thermal characteristics of sensor coated with different thick Parylene.

Therefore, there exists a trade-off here. For waterproof purpose, this Parylene layer should be relatively thick. But for high shear-stress sensitivity, it should be as thin as possible. Nevertheless, if we observe the cross section of the sensor in Figure 3.1 carefully, we can find out that the sensing element itself has already been encapsulated by silicon nitride, which is a superior barrier material. Therefore, there is no need to deposit Parylene on the sensing element. Windows can be opened on the diaphragm to achieve a better interaction between sensor and water just like what we do with the polyimide layer. However, it is always a headache to pattern thick Parylene. More importantly, in this case Parylene coating needs to be done after the packaging. Therefore, the conventional photolithography and oxygen plasma process is not applicable. Here, a method to selectively deposit Parylene C (the most widely used member of Parylene family) on the underwater shear-stress sensor is studied.

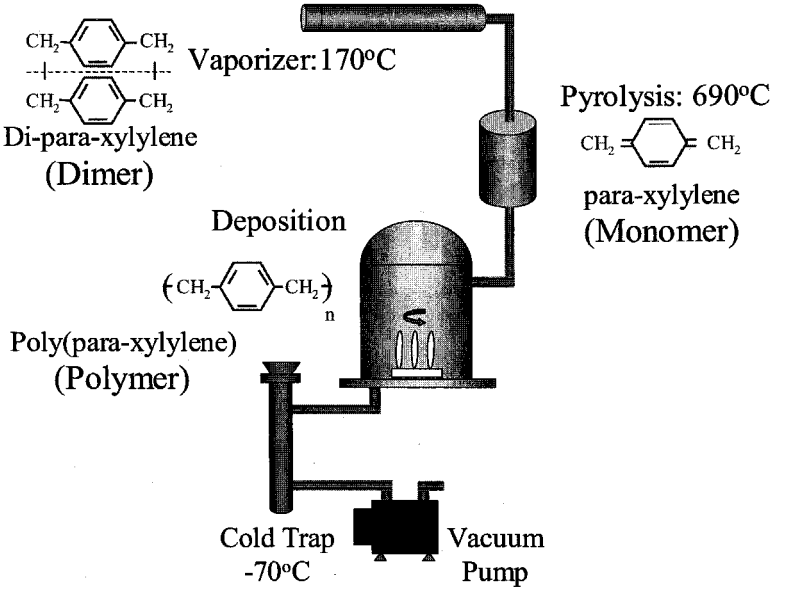

Figure 3.27 Simplified Parylene deposition process [8].

The deposition process of Parylene is illustrated in Figure 3.27. First, the solid dimer is vaporized at about 170°C and then followed by the pyrolysis of the dimer at about 690°C to yield the monomer. Next, the monomer enters the deposition chamber and deposits on any surfaces exposed. However, the deposition will only occur at surfaces where temperatures are below the ceiling temperature of polymerization, which is about 90°C for Parylene C. Therefore the selective Parylene deposition can be simply achieved by passing a current to the sensing element during the deposition. In 1992, E. M. Charlson et al. have explored the temperature selective deposition of Parylene C [16]. They used a metal resistor on silicon substrate as a heat source. In order to heat up locally but not the whole chip, a heat sink with temperature of -20°C had to be attached to the backside of the chip. The power required to maintain a hot spot of 80°C is as huge as 0.8 W based on their simulation.

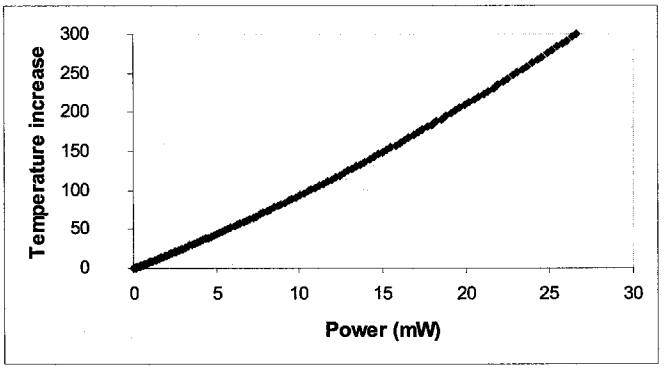

Figure 3.28 Temperature vs. power in vacuum of sensor with 210 μm wide diaphragm.

With vacuum cavity underneath, very small power is needed to heat up the shear-stress sensor as shown in Figure 3.28. In the experiment, the supply voltage is chosen as 12 V to achieve an average temperature of 210°C above ambient temperature, and the power is only 20 mW which can easily be provided by batteries. Moreover, during the

deposition, the temperature increase of substrate is less than 3°C as shown in Figure 3.29. So the selective Parylene deposition can be carried out using a regular deposition system without any modification.

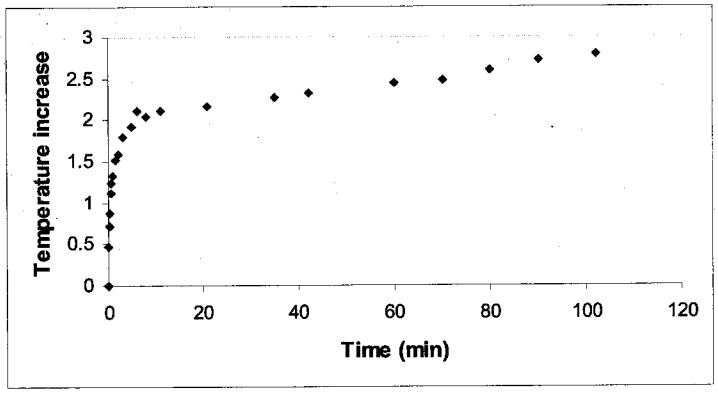

Figure 3.29 Temperature increase of the substrate in vacuum after turning on the power.

Figure 3.30 shows the picture of the sensor selectively coated with 5.2 μm Parylene C. The interference rings can be clearly observed. Very interestingly, these rings also represent the isothermal curves on the diaphragm, which was never obtained before. Figures 3.31 (a) and (b) show the surface profiles before and after 5.2 μm Parylene C selective deposition. Outside the cavity, the Parylene thickness is 5.2 μm, and starting from the edge of the cavity, the thickness decreases sharply. Figure (c) shows the thickness as a function of position after selectively deposited 5.2 μm Parylene C by subtracting (a) from (b). Figure 3.32 compares the static thermal characteristics of two sensors, one uniformly coated with 5.2 μm Parylene C (S1) and the other selectively coated with 5.2 μm Parylene C (S2). As mentioned previously, the heat transfer to water can be estimated by the horizontal difference between sensor's two curves measured in vacuum and water. It is clearly observed that the sensor with selectively coated Parylene

(S2) has more heat transferred to water, namely it has higher sensitivity. We conclude that with selective Parylene deposition, excellent waterproof and high shear-stress sensitivity can be achieved at the same time.

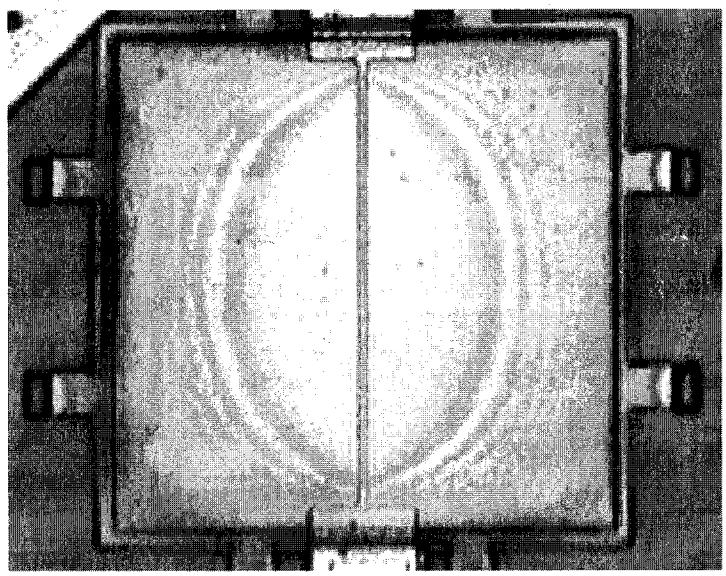

Figure 3.30 Picture of the shear-stress sensor selectively coated with 5.2 μm Parylene C. The interference ring caused by the variation of Parylene C thickness can be clearly observed.

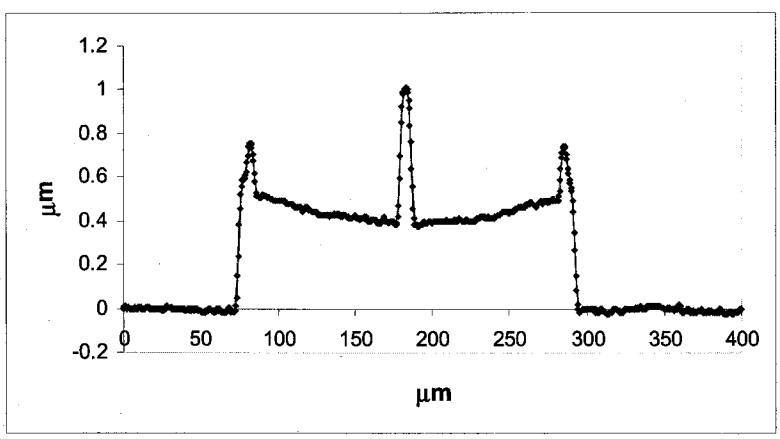

(a)

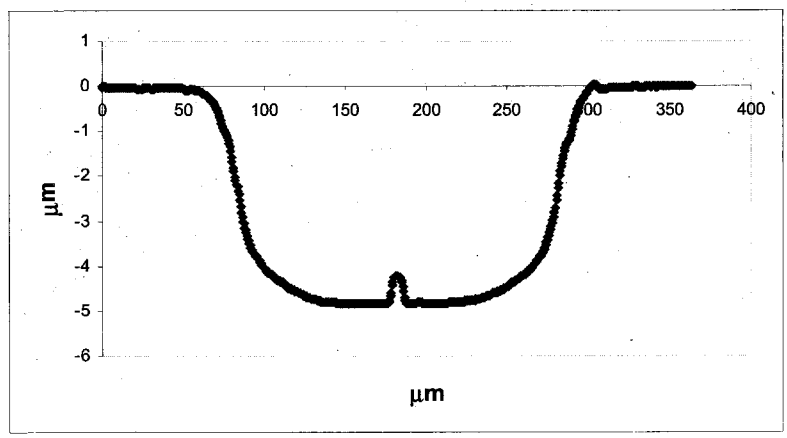

(b)

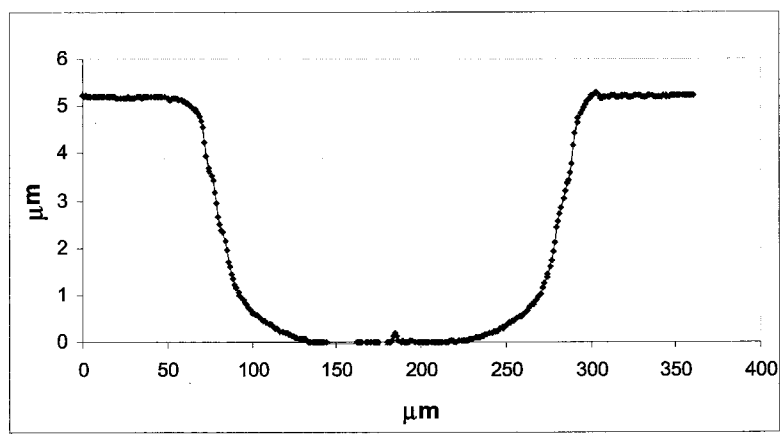

(c)

Figure 3.31 Surface profiles of the underwater shear-stress sensor (a) before Parylene deposition and (b) after 5.2 µm selective Parylene deposition; (c) thickness of Parylene across the diaphragm.

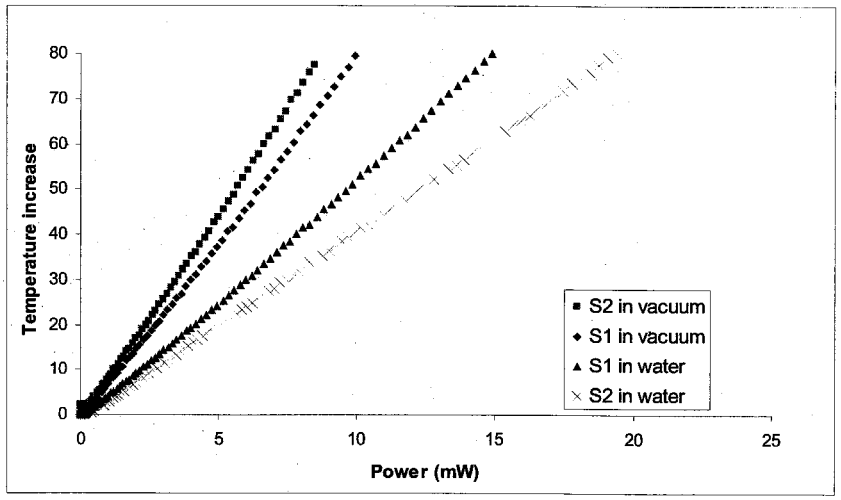

Figure 3.32 Static thermal characteristics of S1, S2 in vacuum and water. S1: uniformly coated with 5.2 μm Parylene C; S2: selectively coated with 5.2 μm Parylene C.

3.7 Packaging

As mentioned in the beginning of this chapter, with the skin structure, the metal leads can be wrapped to the backside of the plug through a thin slit as show in Figure 3.2. We can carry out wire bonding, soldering, or whatever we like on the backside easily. Following picture shows a sensor skin packaged on an aluminum plug using this scheme. We can see the electrical wires coming from the backside of the plug. This whole package is then put in the Parylene deposition chamber and coated with 2 μm Parylene C as waterproof coating. If desired, selectively Parylene deposition can also be employed. After this, the plug can be installed in the water tunnel for shear-stress calibration and then for real underwater applications such as the flow patterns measurement of radio controlled submarines, the study of safety, and arming mechanisms of torpedoes.

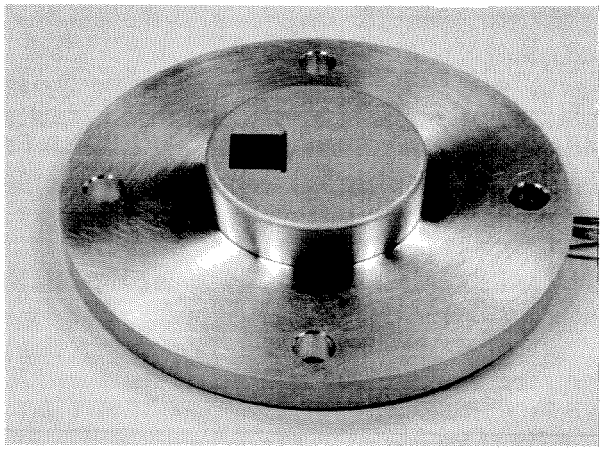

Figure 3.33 A sensor skin packaged on an aluminum plug.

3.8 Summary

Micromachined thermal shear-stress sensors for underwater application were successfully fabricated and tested. Furthermore, the underwater shear-stress sensors have been fabricated onto flexible skins, which not only make it possible for the sensors to be mounted on nonplanar surfaces, but also provide a novel package approach. Parylene is used as the waterproof material and sensors coated with 2 μm Parylene N can survive in water for at least one month when operated at 55°C. Adjusting either the diaphragm width or the polysilicon resistor length can minimize the pressure sensitivity. Although it is possible to have zero pressure sensitivity using a large and thin diaphragm, a small and thick diaphragm is preferred to achieve a better controllability, higher yield and wider operation range. There are several ways to further reduce the pressure sensitivity. For example, the operating temperature can be increased, the sensing element can be buried in the middle plane of the nitride diaphragm, or platinum can be used due to its small gauge factor. A selective Parylene deposition method was developed as well, which can be useful to many other applications.

References

[1] T. Tsao, F. Jiang, C. Liu, R. Miller, S. Tung, J.-B. Huang, B. Gupta, D. Babcock, C. Lee, Y.-C. Tai, C.-M. Ho, J. Kim, and R. Goodman, "MEMS-based active drag reduction in turbulent boundary layers," in *Microengineering Aerospace Systems*, H. Helvajian, Ed.: The Aerospace Press, 1999, pp. 553-580.

[2] X. Q. Wang, Z. Han, F. Jiang, T. Tsao, Q. Lin, Y. C. Tai, and C. M. Ho, "A fully integrated shear-stress sensor," presented at International Conference on Solid-State Sensors and Actuators (Transducer), 1999.

[3] C. Liu, Y. C. Tai, J. B. Huang, and C. M. Ho, "Surface micromachined thermal shear-stress sensor," presented at ASME International Mechanical Engineering Congress and Exposition, Chicago, IL, 1994.

[4] F. Jiang, Y. C. Tai, B. Gupta, R. Goodman, S. Tung, J. B. Huang, and C. M. Ho, "A surface-micromachined shear-stress imager," presented at IEEE International Conference on Micro Electro Mechanical Systems (MEMS), San Diego, CA, 1996.

[5] M. A. Schmidt, R. T. Howe, S. D. Senturia, and J. H. Haritonidis, "Design and calibration of a microfabricated floating-element shear-stress sensor," *IEEE Transactions on Electron Devices*, vol. 35, pp. 750-757, 1988.

[6] A. Cain, V. Chandrasekaran, T. Nishida, and M. Sheplak, "Development of a wafer-bonded, silicon-nitride membrane thermal shear-stress sensor with platinum sensing element," presented at Solid-State Sensor and Actuator Workshop, Hilton Head Island, South Carolina, 2000.

[7] "Parylene data sheet," Specialty Coating System, Indianapolis.

[8] X. Q. Wang, "Integrated Parylene Micro Electro Mechanical Systems," Ph. D. thesis, California Institute of Technology 2000

[9] V. Mosser, J. Suski, J. Goss, and E. Obermeier, "Piezoresistive pressure sensors based on polycrystalline silicon," *Sensors and Actuators A-Physical*, vol. 28, pp. 113-132, 1991.

[10] Y. Xu, F. Jiang, Y.-C. Tai, E. Donzier, W. Loomis, and A. Liberman, "A surface micromachined nitride-diaphragm high-pressure sensor for oil well application," presented at ASME International Mechanical Engineering Congress and Exposition, Orlando, Florida, 2000.

[11] C.-T. Wang, *Applied elasticity*: McGraw-Hill, 1953.

[12] J. A. Schetz and A. E. Fuhs, *Handbook of Fluid Dynamics and Fluid Machinery*, vol. I: John Wiley & Sons, Inc, 1996.

[13] Q. Lin, F. Jiang, X. Wang, Z. Han, Y. C. Tai, J. Lew, and C. M. Ho, "MEMS thermal shear-stress sensors: experiments, theory and modeling," presented at Solid-State Sensor and Actuator Workshop, Hilton Head Island, South Carolina, 2000.

[14] J. B. Huang, F. K. Jiang, Y. C. Tai, and C. M. Ho, "A micro-electro-mechanical-system-based thermal shear-stress sensor with self-frequency compensation," *Measurement Science & Technology*, vol. 10, pp. 687-696, 1999.

[15] F. Jiang, "Silicon-micromachined flow sensors," Ph. D. thesis, California Institute of Technology, Pasadena 1998

[16] E. M. Charlson, E. J. Charlson, and R. Sabeti, "Temperature selective deposition of Parylene-C," *IEEE Transactions on Biomedical Engineering*, vol. 39, pp. 202-206, 1992.

Chapter 4

IC-Integrated Flexible Shear-Stress Sensor Skin

4.1 Introduction

While talking about the advantages of MEMS, the possibility of integration with signal processing and control circuitry is one of the most frequently mentioned. This integration promises to simplify packaging, reduce noise, and improve the overall performance of the system.

In Chapter 2, the successful development of the flexible shear-stress sensor skin and its application on UAV was presented. The complete flow separation detection system consists of the packaged sensor skins, bias board, and data acquisition board. In addition, a large number of cables are needed for interconnection. A lot of work has been done to simplify the implementation process of the sensor skins as described in Chapter 2. However, it is highly desirable to develop IC-integrated shear-stress sensor skins with on-skin bias circuits, amplifiers, and multiplexers. By making an IC-integrated skin, we can eliminate the bias board and interconnection cables, reduce the pin numbers, simplify the design of the data acquisition board, and improve system reliability as well. Potentially, the whole data acquisition board, including the DSP, can

be integrated so that this will be a genuine intelligent flexible skin system. Nevertheless, MEMS-IC integration is not an easy task at all. The integration of MEMS and ICs on flexible substrate presents a unique challenge.

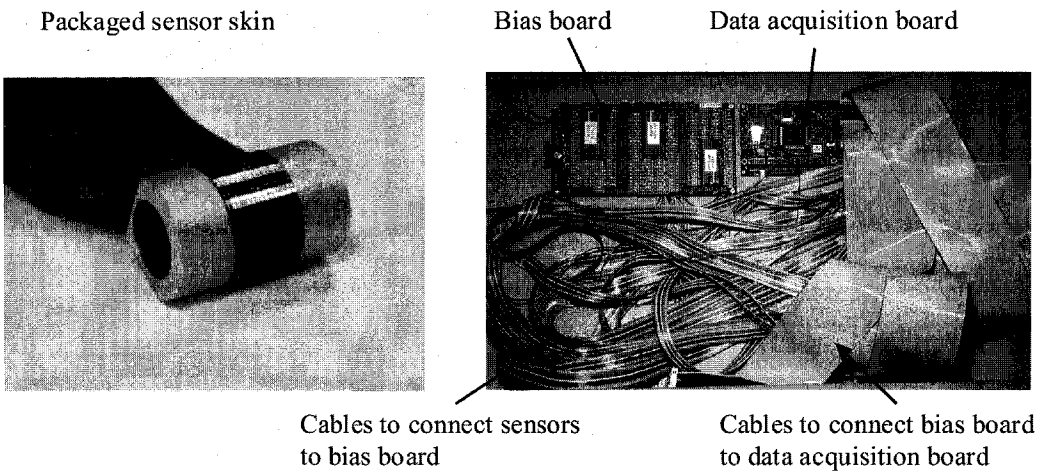

Figure 4.1 The flow separation detection system based on the nonintegrated sensor skin.

Ever since the emergence of MEMS, a great deal of interest has been attracted in MEMS-IC integration technologies [1]. A brief review will be given first. If the circuits are fabricated by CMOS technology, MEMS-CMOS integration is achieved.

4.1.1 MEMS-IC integration

Generally speaking, MEMS-IC integration can be categorized into two groups: hybrid integration and monolithic integration. In the case of hybrid integration, MEMS parts and circuit parts are fabricated separately and then are packaged together by flip-chip bonding or other packaging technologies. Some people may argue that hybrid integration does not fit the definition of integration strictly. Nevertheless, this does not imply that hybrid integration is always the secondary choice compared to monolithic

integration. Hybrid integration does have its advantages. For example, MEMS and IC parts can be optimized separately.

With regard to the flexible shear-stress sensor skin, monolithic integration is preferred since hybrid integration does not simplify the packaging process. Based on when MEMS parts are fabricated, monolithic integration can be classified as mixed MEMS-IC process, MEMS-first process (pre-IC or pre-CMOS) and IC-first process (post-IC or post-CMOS). The first approach is best exemplified by Analog Devices' accelerometer which is fabricated by interleaving, and customizing the MEMS manufacturing steps with the IC process [2]. J. H. Smith et al. at Sandia National Laboratories developed a unique MEMS-first process [3]. In this approach, MEMS devices are fabricated in a trench on the surface of the wafer. Next the wafer is planarized and the trench is sealed. The wafer with MEMS is then processed using conventional IC process. However, it would be highly impossible for any IC foundry service to modify their IC fabrication process or take your pre-processed wafers. Therefore the first two options are only available to some companies or laboratories such as Analog Devices Inc., and Sandia National Laboratories, who have their own IC fabrication facilities.

Most of the monolithic integration is done following the post-IC approach by taking advantages of the widely available IC foundry services. However, the aluminum metalization of ICs demands that the temperature of post-IC process should not exceed 450°C. This limitation precludes a lot of high temperature deposition processes such as LPCVD nitride and polysilicon in post-IC process. To construct MEMS structures on the IC processed wafers, one reasonable way is to use the existing materials of IC process such as polysilicon, metal, dielectric, and substrate silicon. Nevertheless, the IC materials

are optimized for electronics, and the sequence and thickness of the IC layers are fixed. Therefore, the scope of the MEMS structures that can be made is limited. When searching the literature, it is found that the majority of the post-IC processes only involve etching. On one hand, this shows that successful MEMS devices can be made with some simple post-IC releasing steps. On the other hand, this also illustrates the limitation. As you can expect, a number of low temperature post-IC deposition processes have been practiced. For example, in order to enhance the sensitivity of magnetic field sensor, M. Schneider et al. electroplated permalloy (NiFe) on finished CMOS wafers to form magnetic flux concentrator [4]. The simplified fabrication process is as follows: First, a metal-silicon sandwich is sputtered on the wafer. Next, photosensitive polyimide is spun on and patterned with standard UV photolithography. This patterned polyimide serves as electroplating mold. After the permalloy is electroplated, the polyimide and metal-silicon sandwich are etched away. This work illustrates the three most frequently used post-IC deposition processes: sputtering, spin coating, and electroplating. The materials sputtered usually could be metal, Si and SiO_2.

4.1.2 Parylene post-IC technology

In the micromachining group at Caltech, a unique post-IC process was developed based on BrF_3 gas phase silicon etching [5] and room temperature Parylene deposition [6]. Parylene is the generic name for members of a unique family of thermoplastic polymers that are deposited by using the dimer of para-xylylene (di-para-xylylene, or DPXN). There are three types of Parylene commonly used: Parylene N, C, and D. Their

chemical structures are shown in Figure 4.2. Table 4.1 lists their electrical, mechanical, optical, and other properties.

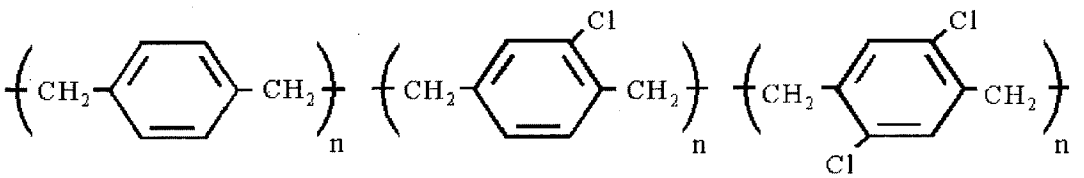

Parylene N Parylene C Parylene D

Figure 4.2 Chemical structures of Parylene.

There are a lot of advantages of using Parylene as a post-IC material. For example, Parylene deposition is a room temperature process. The wafer temperature remains near ambient during the deposition. In addition, Parylene deposition is highly conformal, so that any exposed surfaces are coated at the same rate. Parylene also has good mechanical properties, can be patterned by oxygen plasma, and is chemically inert. For more detailed information on Parylene, please refer to the data sheet from Specialty Coating System [6] and [7].

	Parylene N	Parylene C	Parylene D
Dielectric Strength (V/μm)	275	220	220
Dielectric Constant	2.6	3.1	2.8
Young's Modulus (GPa)	2.5	2.8	2.7
Yield Strength (MPa)	42	55	62
Elongation to Break (%)	20-250	200	10
Density (g/cm3)	1.10-1.12	1.29	1.42
Index of Refraction	1.66	1.64	1.67
Melting Point (°C)	420	290	380
Glass Transition (°C)	>300	240	240
Linear Coef. Of Expan. /°C	$6.9x10^{-5}$	$3.5x10^{-5}$	$3\text{-}8x10^{-5}$
Specific Heat at 20°C (cal/g°C)	0.20	0.17	-
Thermal Conductivity at 20°C (cal/cm°Cs)	$3.0x10^{-4}$	$2.0x10^{-4}$	-

Table 4.1 Properties of Parylene N, C, and D [7].

An integrated shear-stress sensor has been successfully demonstrated using this post-IC parylene technology [8]. The cross section of this post-IC shear-stress sensor is shown in Figure 4.3. The electronic parts are fabricated by Mitel's 2 μm double-poly double-metal CMOS technology [9] and the first poly layer, namely gate poly, is used as the sensing element. The Mitel process will be explained briefly in section 4.3. Parylene-N is used as the membrane material instead of LPCVD nitride. The cavity underneath the sensing element is achieved by BrF_3 gas-phase etching.

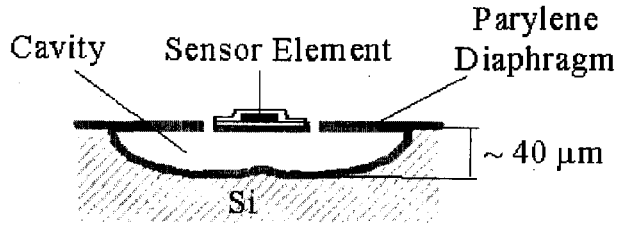

Figure 4.3 Cross section of the post-IC shear-stress sensor [7].

4.1.3 Post-IC flexible skin technology

As we state in the beginning of this chapter, it is highly desirable to integrate circuits into the flexible shear-stress sensor skins. Combining the flexible skin technology we already have and the process of rigid-chip integrated shear-stress sensor, an IC-integrated flexible shear-stress sensor skin is proposed. Figure 4.4 illustrates the cross section of the integrated flexible skin. Conceptually speaking, there are three major steps to manufacture the integrated flexible shear stress-sensor skin:

1. fabrication of the circuits;
2. fabrication of the shear-stress sensors;
3. fabrication of the skin structure.

However, these three steps are correlated with each other closely. In particular, the steps of sensors and skin fabrications cannot be separated. So from the perspective of the actual process, there are two steps: IC fabrication and post-IC MEMS process. Each one has already been proven. Nevertheless, to integrate them together is still a big challenge and has never been demonstrated before. The design, layout, and process have to be considered carefully to insure good compatibility. Some of the major concerns are the sequence of the processing steps, effect of high temperature post-IC process, and

protection of existing devices. All these technical challenges will be described in the following sections.

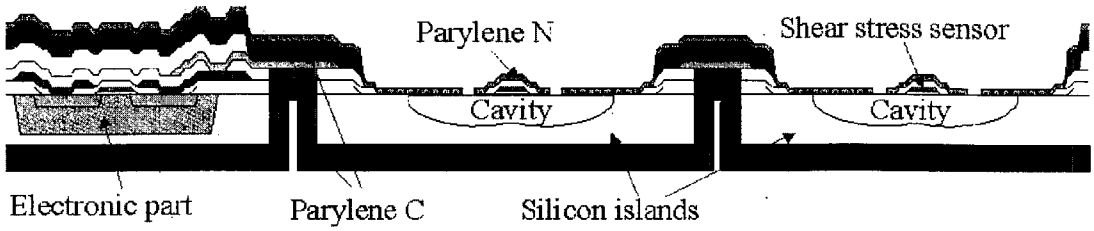

Figure 4.4 Cross section of the integrated flexible shear stress sensor skin.

4.2 Design of the IC-integrated flexible shear-stress sensor skin

Figure 4.5 shows the schematic of the integrated flexible shear-stress sensor skin. The shear-stress sensors, which utilize the gate polysilicon of the CMOS process as the sensing elements, operate in CC mode and are biased by the cascode current mirrors. The output voltage is multiplexed by PMOS switches and addressing circuitry. There are a total of 16 shear-stress sensors, which can be exactly accessed by a 4-bit address. An operational amplifier is also implemented to perform on-chip amplification. The following sections briefly describe the design of each subunit.

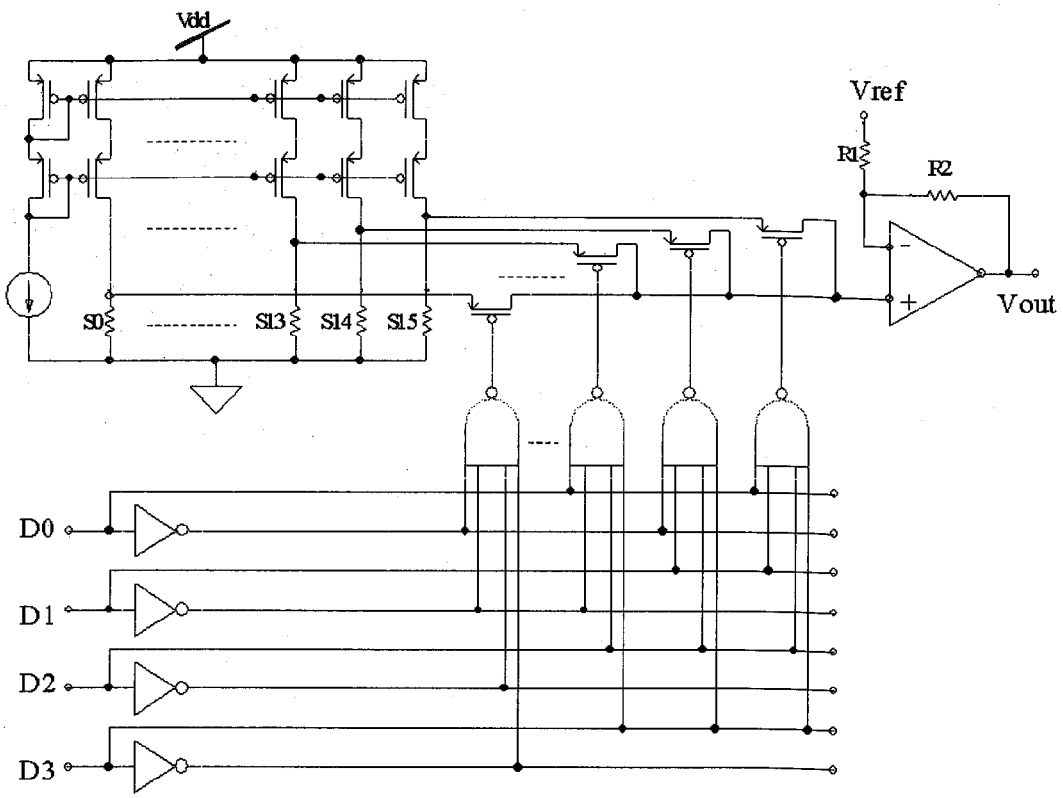

Figure 4.5 Schematic of the integrated flexible shear-stress sensor skin.

4.2.1 Shear Stress Sensor

As mentioned above, the sensing element of shear-stress sensor utilizes the gate poly of the Mitel 2 μm double-poly, double-metal CMOS process. This poly is 0.32 μm thick, with a temperature coefficient of resistance (TCR) of 0.1%, and a sheet resistance of 20Ω/□. According to the work of X. Q. Wang *et al* [8], with 1.3V voltage across the suspended 380 Ω polysilicon resistor, 10% over-heat ratio is achieved. The power consumption is about 4.5 mW. In order to achieve a high sensitivity, the shear-stress sensor needs to be operated in a higher over-heat ratio which requires more power

consumption. The simple equation $P=I^2R$ tells us that there are two ways to increase power. First one is to increase the current, but this will cause large voltage drop across the current mirror and limit the dynamic range of output voltage of the shear stress sensor. So we use the approach of increasing resistance. The resistance of the shear-stress sensor is chosen as 1.2 kΩ. With 2.7mA bias current, the output voltage is 3.8V and over-heat ratio is 20% to a first order approximation. The above calculation assumes the heat transfer condition does not change compared to Wang's sensor. However, the polysilicon resistor width shrinks from 10 μm to 4 μm. This reduction in width results in a better thermal isolation of the sensing element so that 20% over-heat ratio can be achieved at a much lower power.

4.2.2 Cascode current mirror

The purpose of the cascode configuration of current mirror is to increase the output resistance. For a simple current mirror, we have the following equation for output resistance

$$r_{out} = r_{ds} = \frac{1}{\lambda I_D}, \tag{4.1}$$

where I_D is the drain current in the saturation region and λ is the channel length modulation parameter. As shown in Figure 4.6, the output resistance of the cascode configuration is increase to

$$r_0 = r_{ds1} + r_{ds2} + (g_{m2} + g_{mb2}) r_{ds1} r_{ds2}, \tag{4.2}$$

where g_m and g_{mb} are the top-gate and body-effect transconductance of the p-channel MOSFET.

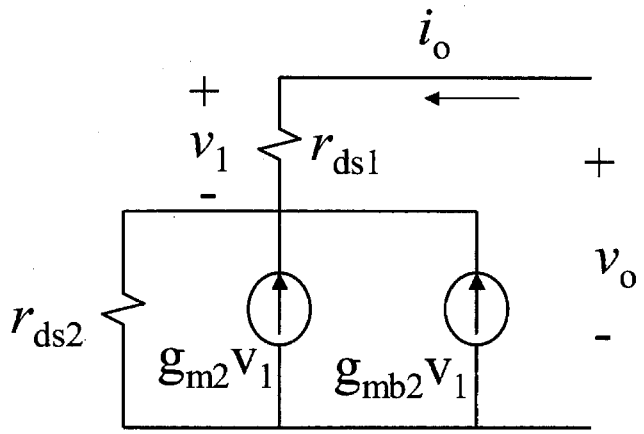

Figure 4.6 The small signal model to calculate the output resistance of the cascode current mirror.

We also use a very large *W/L* ratio, which is 5957/2, to reduce the voltage drop across the source and drain. With this large *W/L* ratio, the minimum V_{DS} is about 0.29V for I_D=2.7mA, which provides enough voltage swing for the shear-stress sensor.

4.2.3 Multiplexer

The multiplexer is composed of 16 PMOS switches and the logic circuitry turning on/off the switches. One important parameter is the on-resistance of the PMOS switch, which can be expressed as

$$R_{on} = \frac{L}{\mu_p C_{ox} W |V_{GS} - V_T|} \tag{4.3}$$

With *W/L* = 5, the on-resistance is about 8kΩ with V_{GS} = 2V. There are 16 4-input NAND gates which decode the 4-bit address to control the 16 PMOS switches. For example, when the address is 0000, the leftmost NAND (Figure 4.5) outputs low voltage,

turning on the corresponding switch. All the other NAND gates output high voltage, turning off the remaining switches.

4.2.4 Operational amplifier

Figure 4.7 shows the schematic of the operational amplifier. M1 and M2 consist of differential input pair. The offset can be adjusted by M5, M6 and M8. M9 is a common source amplifier with M10 as its active load. Rc and Cc serve a compensation purpose. M11 is a common drain output stage. This operational amplifier is connected in a negative feedback configuration as shown in Figure 4.5. And the output is

$$V_{out} = (1 + \frac{R2}{R1})V_{in+} - \frac{R2}{R1}V_{ref} \tag{4.4}$$

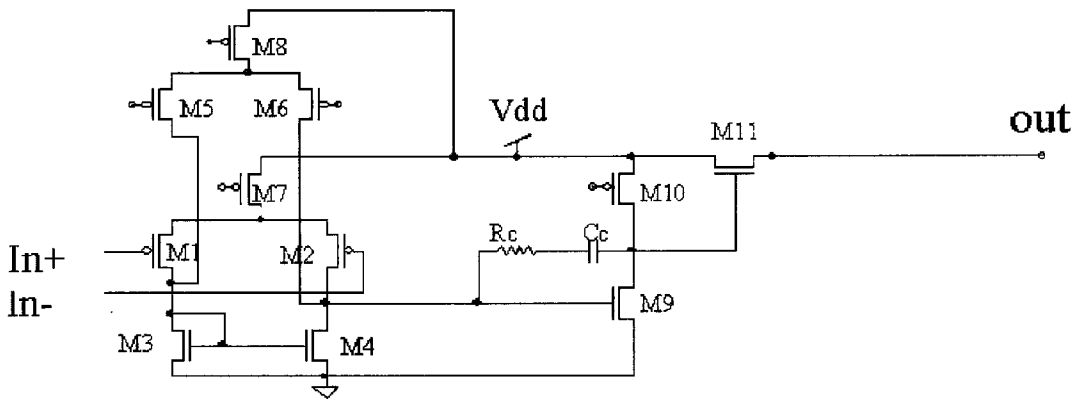

Figure 4.7 Schematic of the operational amplifier.

4.2.5 Layout of the skin

The layout should be carefully designed, not only for patterns in horizontal dimension, but also for layers in vertical dimension. As shown in Figure 4.8, the

dimension of the skin is $20 \times 10 mm^2$. The distance between the first and the last sensors is 15 mm so that it could completely cover a semicylinder with a diameter of 9.55 mm. The array of small gray squares represent the 0.4×0.4 mm^2 silicon islands. All the electronic parts are placed on the left side of the skin on a big silicon island. If necessary, the electronic parts can also be distributed on the small silicon islands. Between the big silicon island on the left side and the small silicon islands on the right side, there is an area where silicon underneath is completely etched away and these two parts are mechanically connected by Parylene film. This allows very sharp folding angle when packaging the flexible skin, which is very desirable in some specific applications. The blue wires are the first metal layer while the gray ones represent the second metal layer. The 16 shear-stress sensors are connected to the current mirrors by the second metal layer. The multiplexer and operational amplifier are placed in the lower-left corner. All the pads are on the left-side edge. Since the thermal shear-stress sensor is very sensitive to the ambient temperature, a temperature sensor is also included for temperature compensation. There are also some testing structures placed on the skin. For example, a coil structure, which can be a flap, is put in the lower-right corner.

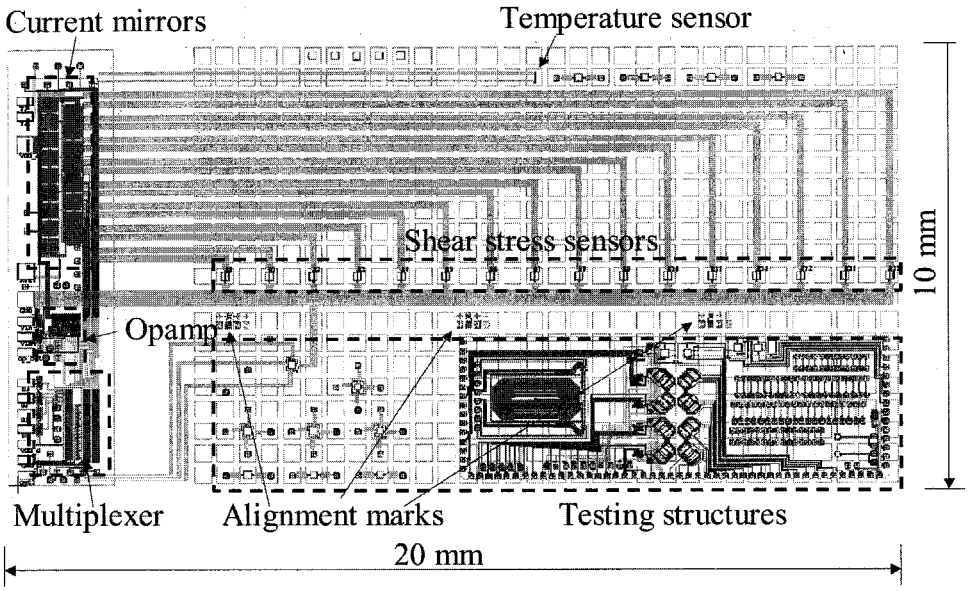

Figure 4.8 The layout of the integrated shear-stress sensor skin.

One other thing needs to be considered carefully is the arrangement of the dies on the wafer. This will affect the alignment of the post-IC process. Our lab's GCA stepper uses two alignment marks which are 76.2 mm apart. As shown in Figure 4.9, there are three alignment marks spaced 5.442855 mm apart. The step size of dies in x direction is 21.77142 mm (Figure 4.9) so that there are two alignment marks which are exactly 76.2 mm apart. The y step size is chosen as 15 mm to leave enough silicon as mechanical support when etching through wafer from the backside.

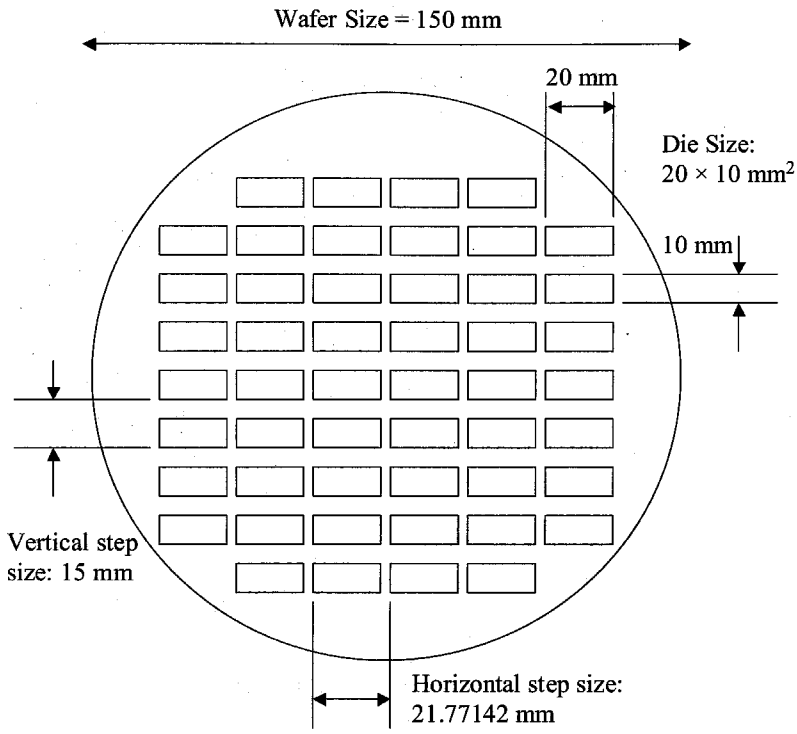

Figure 4.9 Arrangement of dies on the six-inch wafer.

4.3 Fabrication

As mentioned in 4.1.3, the fabrication of the integrated flexible shear-stress sensor skin consists of two stages. First, the CMOS circuits are fabricated by foundry service, which is Mitel Semiconductor in this case. Then the post-CMOS MEMS process is conducted in the Caltech Micromachining Lab.

4.3.1 IC fabrication

The silicon foundry we used to fabricate the electronic circuits is Mitel Semiconductor and the process is 2 μm p-well double poly/double metal CMOS process

[9]. Figure 4.10 shows the six-inch wafer received from Mitel and the cross section is illustrated in Figure 4.11(a). The sensing element of shear-stress sensor utilizes the gate poly, which is 320 nm thick, with a temperature coefficient of resistance (TCR) of 0.1% and a sheet resistance of 20Ω/□.

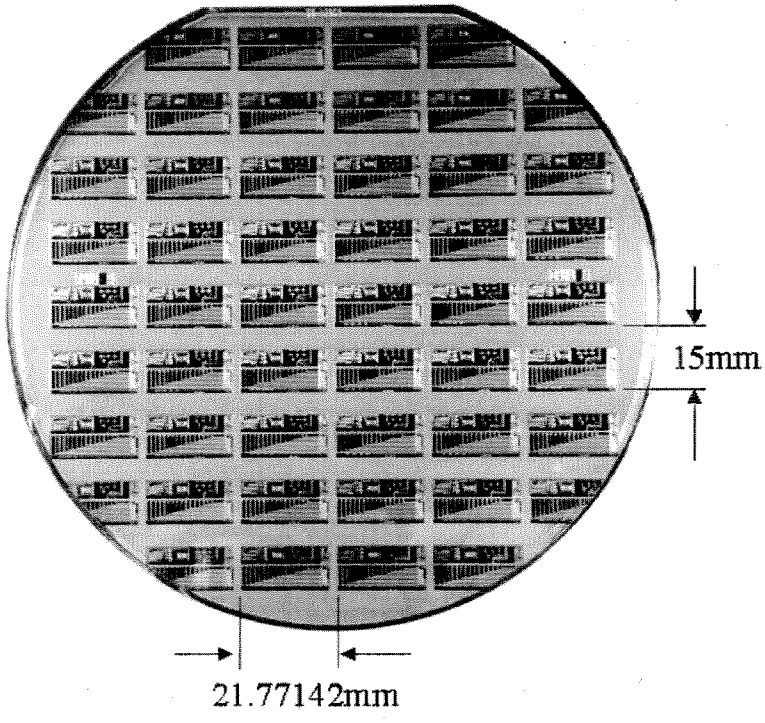

Figure 4.10 Six-inch wafer received from Mitel.

4.3.2 Post-IC process

The simplified post-IC process is illustrated in Figure 4.12. As shown in (a), the sensing elements are covered by dielectric and metal layers when the wafer comes back from Mitel. The post-CMOS MEMS process begins with patterning the metal and dielectric layer at the sensor area. This is supposed to be a very straightforward step. However, we can see in (a) that metal 1 is supposed to protect the dielectric layer. Since

the glass on top of metal1 is removed in via-opening step, metal 2 is directly deposited on metal 1. Therefore metal 1 is also attacked when etching metal 2. As a matter of fact, we observed that metal 1 is completely etched away. In most dies, the Ti/TiNC diffusion barrier layer underneath is partially attacked. As a consequence, the dielectric layer is partially attacked during the pad opening step and therefore some part of the polysilicon resistor is exposed. This causes a lot of trouble during the step of patterning Ti/TiNC with SF_6 plasma because the exposed polysilicon is attacked too. The Ti/TiNC layer exhibits a relatively low resistivity. So it actually shorts the polysilicon sensing element and has to be removed. By measuring the resistance of the polysilicon resistor, we are able to tell if there still exists Ti/TiNC layer. Fortunately, in most cases, the continuous Ti/TiNC layer only exists along the perimeter of the square as shown in the following figure. Therefore it only needs to etch the four corners of the square.

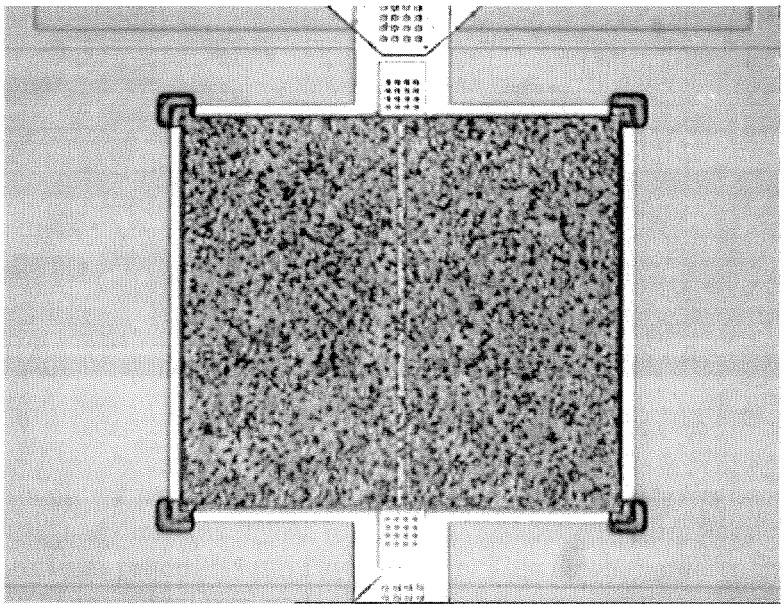

Figure 4.11 Partially attacked dielectric layer.

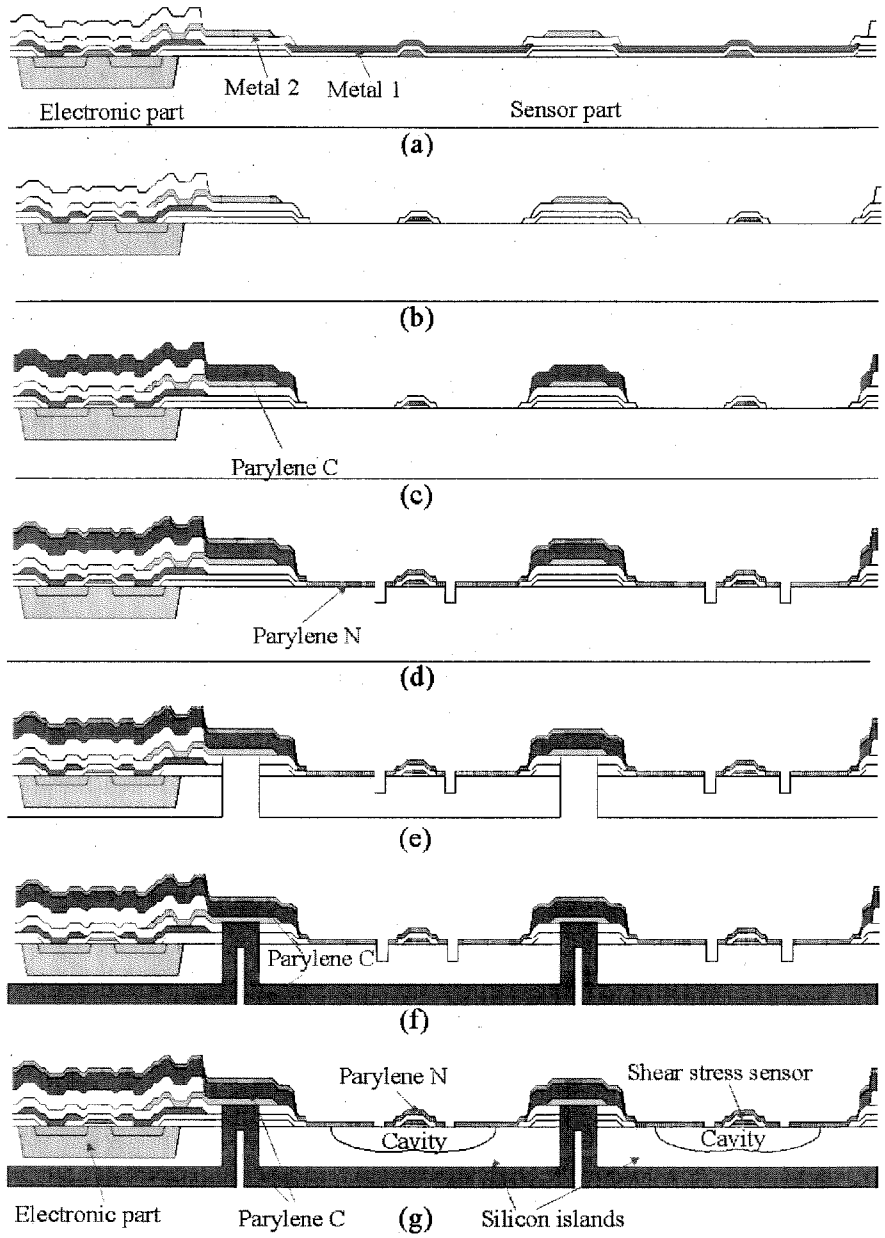

Figure 4.12 Simplified post-CMOS process: (a) Cross section of wafer back from Mitel; (b) Pattern metal and dielectric layers; (c) Deposit and pattern10 μm Parylene C on front side; (d) Deposit and pattern 1.5 μm Paylene N; (e) Thin down the wafer from back side, form the silicon islands by DRIE and remove the dielectric layer; (f) Deposit another 10 μm Parylene C from on back side; (g) Release the shear-stress sensor by BrF_3.

The next step is to pattern the dielectric layer, which is brittle and has to be removed from the diaphragm areas. The passivation layer on the metal wires, which will undergo bending after the formation of skin structure, should also be stripped. Next, the first 10 μm layer of Parylene C is deposited on the front side of the wafer. A small trick here is that the backside of the wafer can be protected by dicing tape. This avoids the step to strip the backside Parylene. Windows are opened on sensors and pads by oxygen plasma. To pattern 10 μm Parylene safely, the photoresist mask has to be thicker than 15 μm. Special caution must be taken to prevent the thick photoresist from cracking during the plasma etching.

There is one very crucial step not shown in Figure 4.12, which is the step to make double side alignment marks since our stepper does not have such capability. It is impossible for a commercial IC foundry to make double side alignment marks while fabricating the ICs. A simple method is to etch square holes all the way through the six-inch wafer by DRIE. This method is very straightforward, sometimes even seems a little bit stupid, but it works. The walls of the holes etched by DRIE may not be vertical to the surface. Therefore, there might be some errors by using the backside holes to align to the frontside patterns. However, after the photolithography step on backside, we always can use the infrared camera to measure the front-back offset. Then we can re-do the photolithography to compensate for the offset.

After this, 1.5 μm Parylene N is deposited. Please note that both Parylene C and N are used in this project. Parylene C serves as the mechanical support sandwiching the silicon islands while Parylene N serves as the diaphragm material to support the sensing elements. There are two major differences between Parylene C and N which lead to their

different roles in this project. The first difference lies in the melting temperature. Parylene N has a much higher melting temperature (420°C) than that of Parylene C (290°C). Since the polysilicon resistor will be heated up during operation, Parylene N is chosen as the membrane material. The second difference lies in the deposition rate. Parylene C has a much higher deposition rate than Parylene N. To provide enough mechanical support, we need approximately 10μm Parylene on both front and back sides. It is impractical to deposit such a thick layer of Parylene N. Please note that the thermal conductivity of Parylene N is much smaller than silicon nitride. So the Parylene N cannot be too thick, otherwise the sensitivity of shear-stress sensor will be very low. As opposed to the shear-stress sensors in previous chapters, here Parylene N is used as the membrane material instead the silicon nitride. The following table compares some important parameters of Parylene N and silicon nitride.

	Young's Modulus (GPa)	*Intrinsic Stress (MPa)*	*Thermal Conductivity (W/cmK)*	*Thermal Expansion ($1/^oC$)*	*Melting Point (^oC)*
PA-N	*3*	*20*	*0.0013*	*7×10^{-5}*	*420*
Si_xN_y	*200-300*	*200-400*	*0.032*	*8×10^{-7}*	*$>10^3$*

Table 4.2 Comparison of mechanical properties of silicon nitride and Parylene N (PA-N) [7].

The releasing holes for the shear-stress sensor are then formed by patterning Parylen N as shown in step (c). These holes are further etched into the silicon substrate to facilitate the BrF_3 releasing process.

The process at the backside begins with the thinning down of the wafer. Next, the silicon islands are formed by etching away the silicon in between. DRIE is used in these two steps. After etching away the silicon down to the dielectric layer on the front side, pad etchant is used to remove the dielectric layer. This step is crucial because the dielectric layer, if not removed, will break the aluminum wires when the skin undergoes bending. Therefore, to assure that it is completely etched away, over etching is preferred. As shown in the Figure 4.13, the undercuts on the edge of the islands can be observed. The metal wires may touch the silicon substrate due to these undercuts. In order to solve this problem, back-to-back pn junction isolation is used at the places where the metal wires cross the silicon islands.

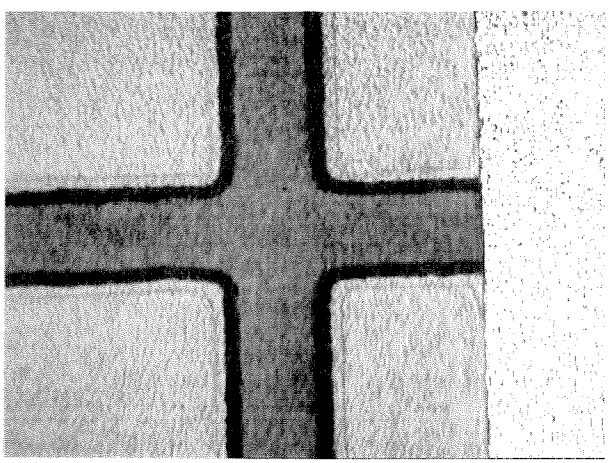

Figure 4.13 The undercuts of the dielectric layer on the edge of silicon islands observed from the front side

Now it comes to the step to deposit 10 μm Parylene C on the back side to sandwich the silicon islands. However, we do not want Parylene deposited on the front side. The dicing tape does not work here since it may peel off the Parylene already

deposited. Here a different technique is employed. First, photoresist is spin-coated on the front side. Then a dummy wafer is attached after baking the photoresist. Therefore there may exist a very thin gap between the dummy wafer and photoresist since they do not stick to each other. Parylene may go through the gap and deposit on photoresist. However, the amount of Parylene deposited is significantly reduced. After deposition, oxygen plasma can be used to etch away the very thin layer of Parylene on photoresist and the photoresist can be easily stripped.

The final step is to release the polysilicon resistor by BrF_3, which is a gas phase silicon etchant. The purpose of this step is to suspend the sensing element so that good thermal isolation can be achieved. This step is very risky. Therefore the sensor skins are cut off from the wafer by razor blade and released one by one. After several trials, it can be concluded that for successful releasing, higher pressure (e.g., 6 torr) and short time (< 10 seconds) should be used. Low pressure BrF_3 tends to attack the silicon and Parylene interface. A successfully released shear-stress sensor is shown in Figure 4.14. There are two columns of releasing holes on each side of the polysilicon resistor. The particulates surrounding the sensor were generated during the deposition of 1.5 μm Parylene N and are possibly due to a contaminated surface. The integrated skin cut from the wafer is shown in the following Figure 4.15. The silicon islands are emphasized by shining light from the backside. The metal wires across the islands can also be clearly observed.

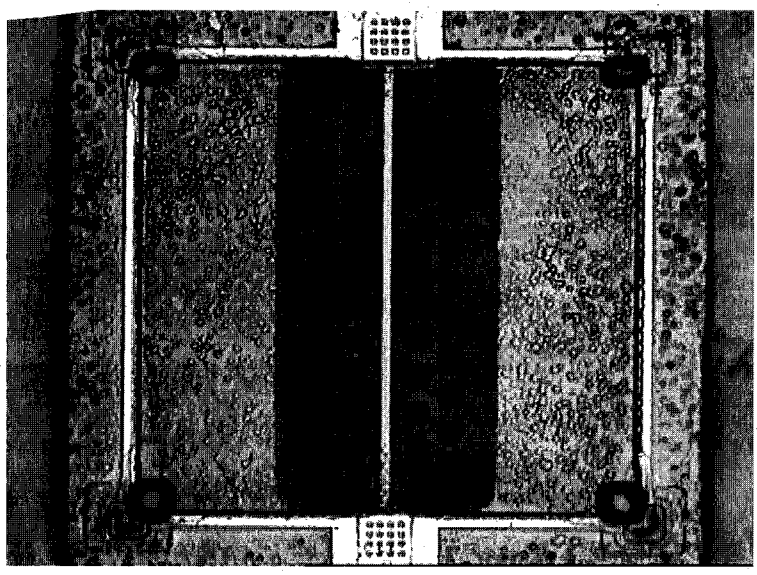

Figure 4.14 A shear-stress sensor released by BrF_3.

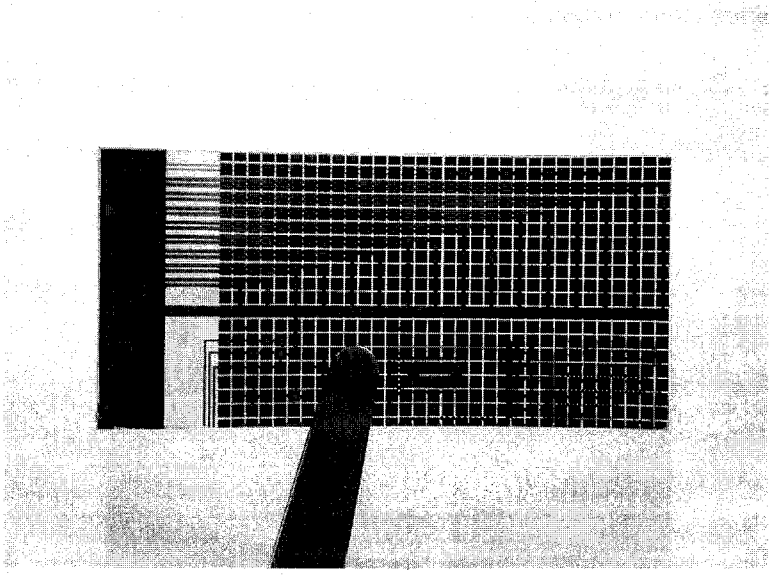

Figure 4.15 An integrated skin cut from the wafer with the silicon islands highlighted by shining light from backside.

The sequence of the process has to be considered carefully. For example, the releasing of the shear-stress sensor has to be the last step to prevent it from breaking. But

the opening of the releasing holes has to be done before the formation of the silicon islands. Once the rigid silicon becomes islands, lateral deformation occurs and accurate alignment is not possible anymore.

4. 4 Packaging of the skin

The sensor skin can be readily mounted on a nonplanar surface. Figure 4.16 (a) shows two skins packaged on a semicylindrical surface of an aluminum block. The diameter is chosen for the 16 shear-stress sensors to exactly cover the semicylinder. So the angle between the adjacent two sensors is 12°. For this first run, the main purpose is to demonstrate the technology and we do not want the process to be too complicated. Therefore, as shown in Figure 4.16 (b), wire-bonding and conventional soldering are used to connect out sensors from the sensor skin. The solder-bonding technique presented in Chapter 2 can be introduced in a future run. The packaged sensor skin shown in (b) was also tested in the wind tunnel at UCLA.

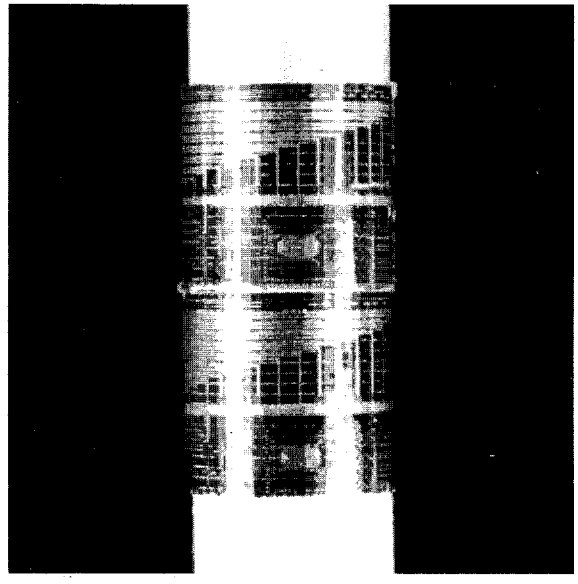

(a)

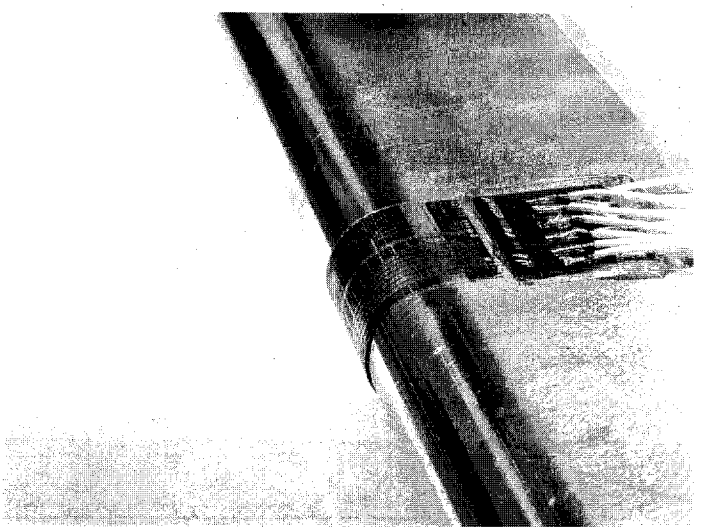

(b)

Figure 4.16 Sensor skins mounted on semicylindrical aluminum block.

4.5 Testing and Discussion

4.5.1 Testing of circuits

The circuit part is first briefly characterized. Shown in Figure 4.17 is the output characteristic of the current mirror. The output range is from 0 to 3.8 V for 2.2 mA current which is good enough for our application. Another important parameter of current mirror is the output resistance which is illustrated in Figure 4.18. The measured on-resistance of the PMOS switch is illustrated in Figure 4.19.

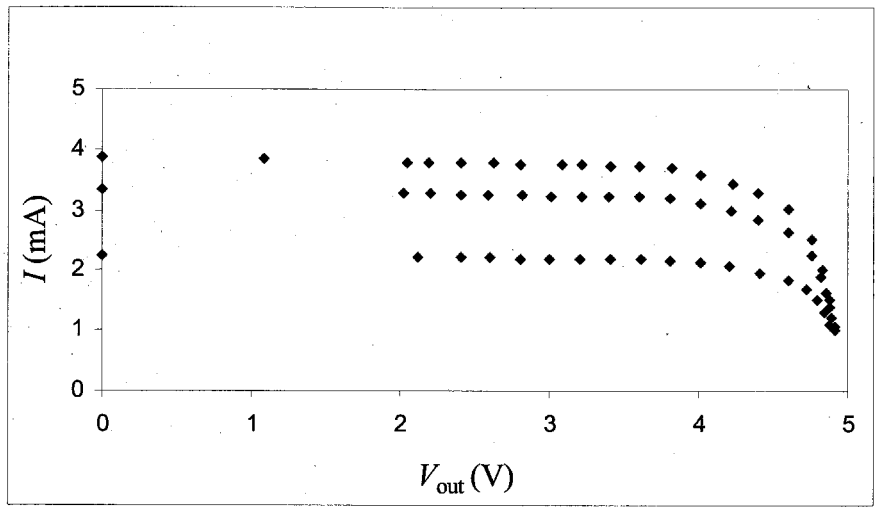

Figure 4.17 Output characteristic of the current mirror. 5 V supply voltage is used.

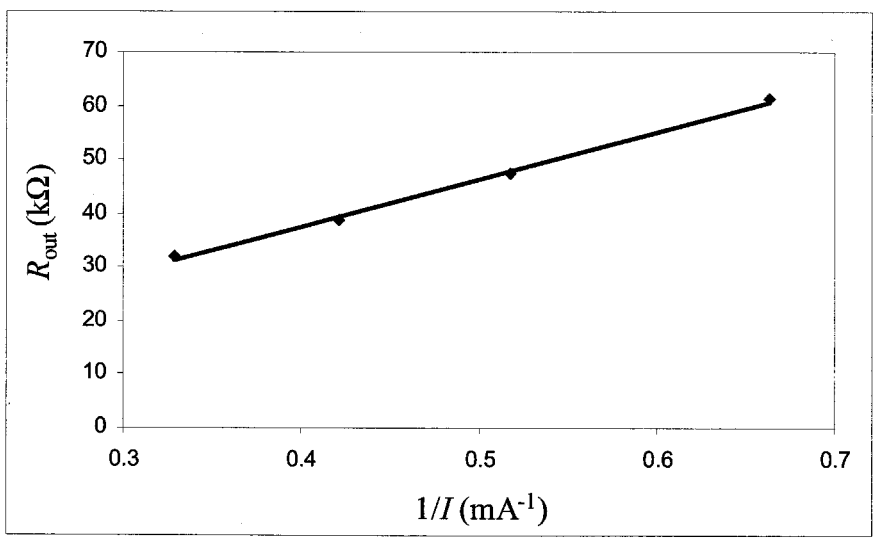

Figure 4.18 Output resistance of the cascode current mirror.

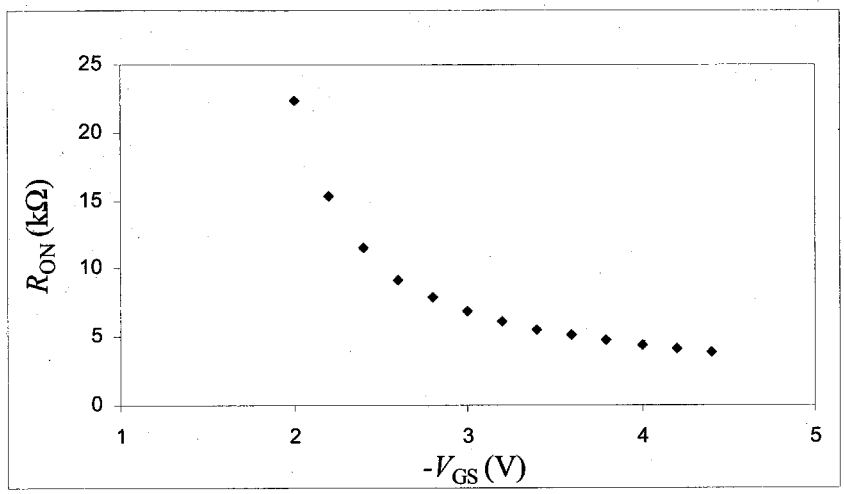

Figure 4.19 Measured on-resistance of PMOS switch as a function of V_{GS}.

4.5.2 I-V curve measurement of the released shear-stress sensor

From the I-V curve measurement, we can derive the temperature vs. power relationship as shown in Figure 4.20. Therefore the over-heat ratio can be set based on these results.

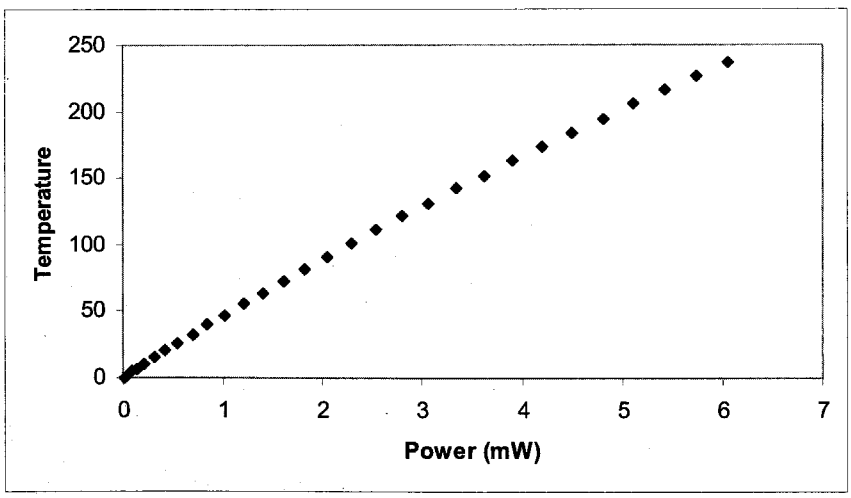

Figure 4.20 Measured static thermal characteristics of the shear-stress sensor (temperature-power relationship)

4.5.3 Wind tunnel test

The wind tunnel test is carried out in UCLA's wind tunnel lab. The testing setup is shown in Figure 4.21. The integrated sensor skin is mounted on the semicylindrical surface of the aluminum block. Shear stress distributions along the semicylinder are measured at different angles of attack and different flow speeds as shown in Figure. The definition of angle of attack α and sensor location θ can also be found in Figure 4.21. Sensor 0 is at the top surface and sensor 15 is at the bottom surface of the aluminum block. The angle between the adjacent two sensors is 12° and the 16 sensors exactly span 180°. Unfortunately sensor 15 is broken during handling and there are no data collected. The data collected by the sensor skins at different conditions are illustrated in Figure 4.22. It is worth noting that the vertical axis is the normalized output change $\Delta V / V_0$, where V_0 is the output voltage at zero shear stress. The purpose of this normalization is to minimize the nonuniformity of the sensors' shear-stress sensitivity caused by the process variation. For CT mode, it can be proved that the output change can be just normalized to V_0 (Appendix). For sensors operated in CC mode, the situation is more complicated. However, to a first-order approximation, we still can employ $\Delta V / V_0$ normalization. The separation point, which is characterized as the place where the shear stress has a sharp jump, can be clearly observed. Interestingly, the stagnation point, where the shear stress has a minimum value in the middle can also be identified. In the case of 0° AOA, the stagnant point is at the sensor 7, which is exactly what we expect. While the separation points may be at sensor 0 and sensor 15 or beyond. In the case of 15° AOA, the separation point is at sensor 2 while the stagnant point is at sensor 9. For 30° AOA, the

separation point moves to sensor 3 while the stagnant point moves to sensor 13. From Figure 4.23, which puts together the normalized output change of the sensors at 0°, 15°, 25° and 30° angles of attack with flow velocity of 30 m/second, the shift of separation points and stagnant points can be clearly observed.

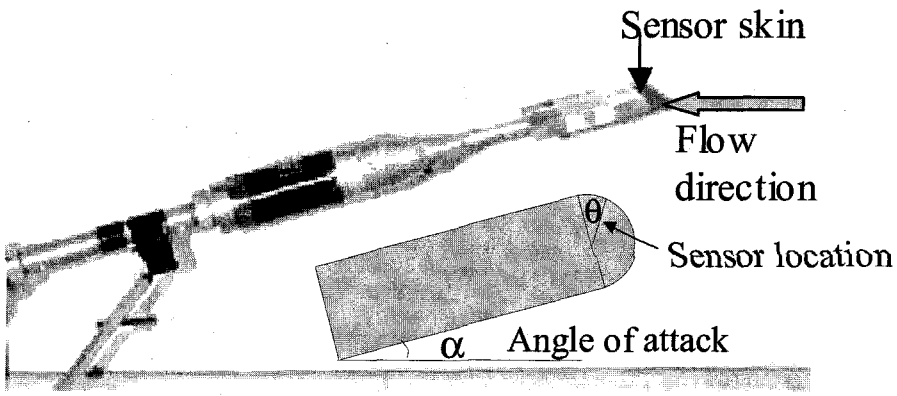

Figure 4.21 Testing setup in wind tunnel.

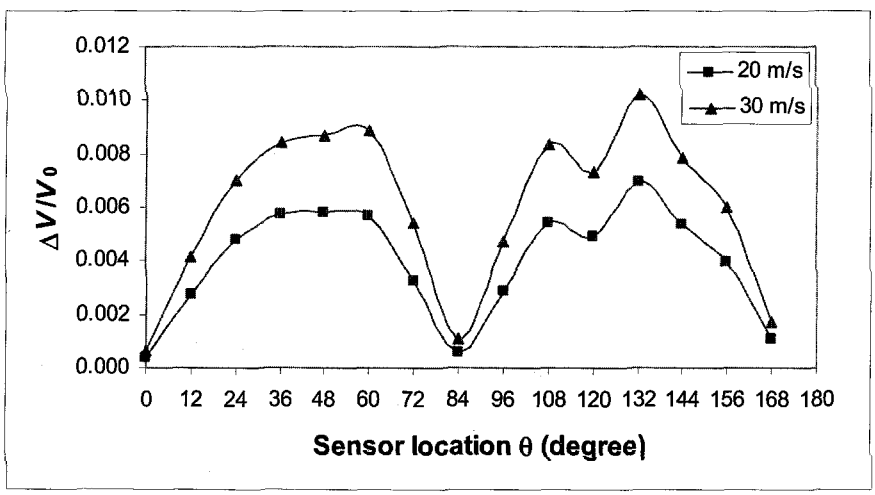

(a) 0° angle of attack

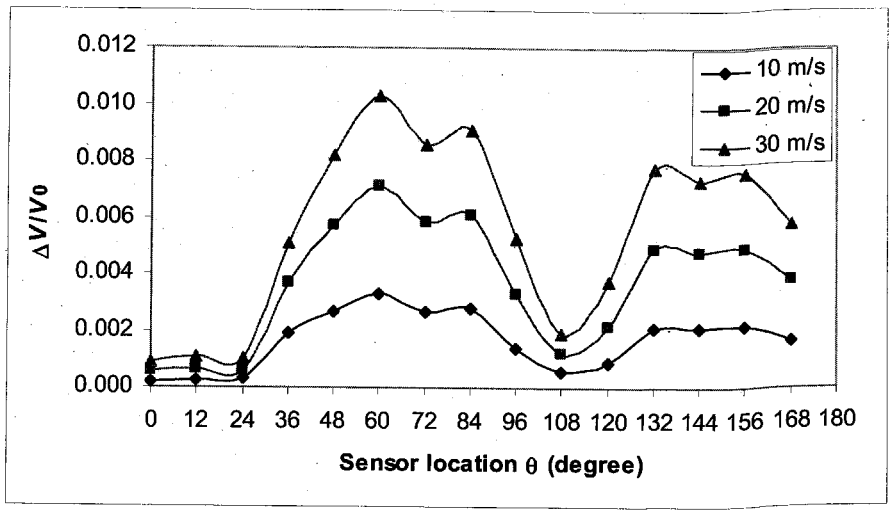

(b) 15° angle of attack

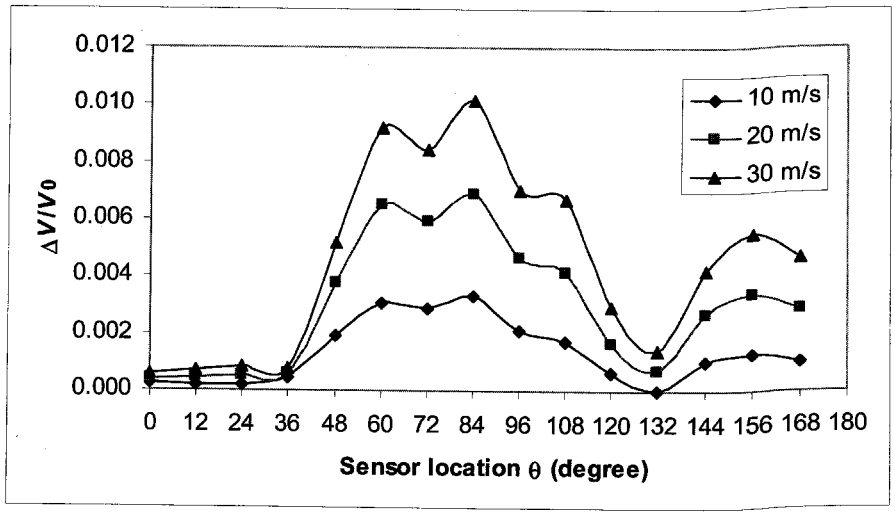

(c) 25° angle of attack

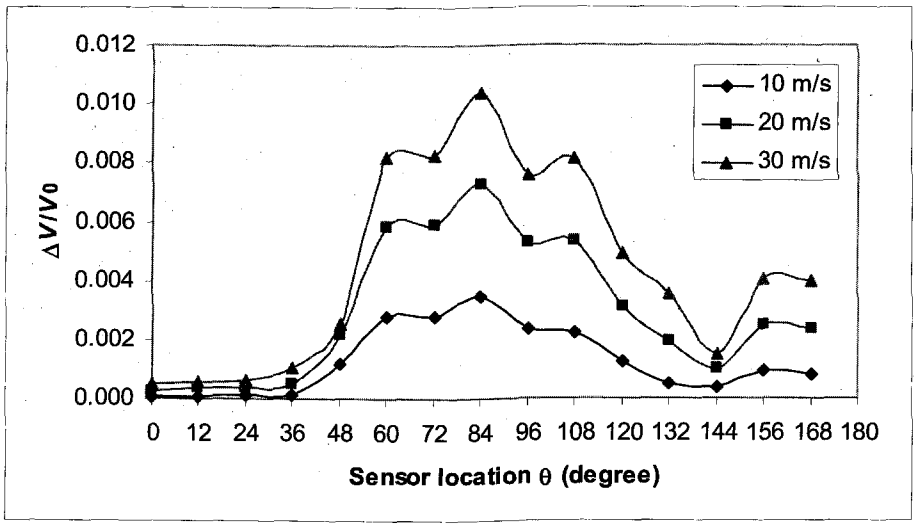

(d) 30° angle of attack

Figure 4.22 Normalized sensor output change at different angles of attack and different flow velocities. The angle between the adjacent two sensors is 12°.

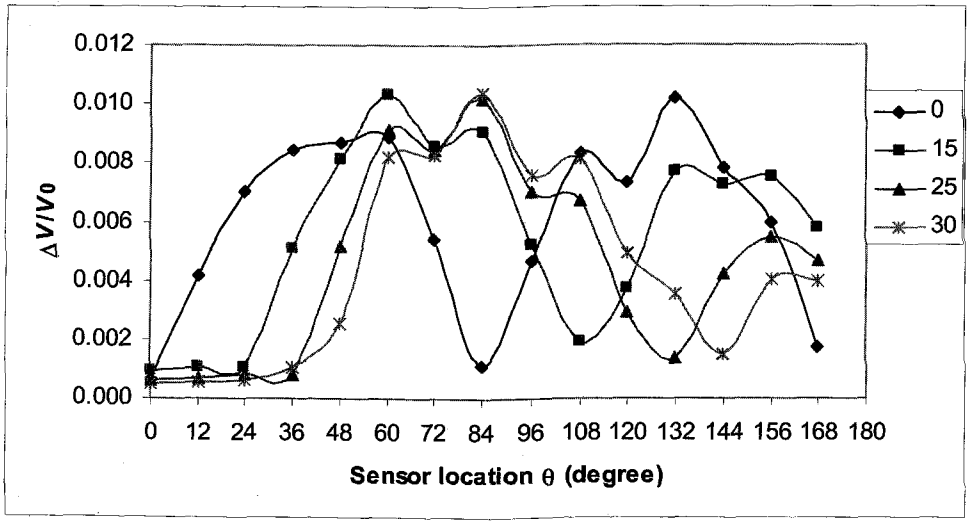

Figure 4.23 Movement of separation points and stagnant points as the angle of attack varies. All the data are measured when the flow velocity is 30 m/s. The legends denote the angles of attack.

4.6 Summary

With room temperature conformal Parylene deposition, gas phase BrF_3 silicon etching and DRIE, an IC-integrated flexible shear-stress sensor skin was successfully fabricated. The circuit parts were first made by a commercial IC foundry (i.e., Mitel) and the post-CMOS MEMS process was carried out on the CMOS wafers to form the sensors and skin structures. By integrating both bias and signal-conditioning circuitry on-chip, the deployment of the skin is significantly simplified and reliability is improved. We further demonstrated the use of the sensor skin by packaging it on a semicylindrical aluminum block and tested it in a wind tunnel. In our experiment, the skin has successfully identified both the flow separation and stagnation points.

References

[1] H. Baltes and A. Haberli, "CMOS MEMS," presented at IEEE International Symposium on Circuits and Systems. Circuits and Systems in the Information Age. ISCAS '97 vol.4, 1997.

[2] W. Kuehnel and S. Sherman, "A surface micromachined silicon accelerometer with on-chip detection circuitry," *Sensors and Actuators A-Physical*, vol. 45, pp. 7-16, 1994.

[3] J. H. Smith, S. Montague, J. J. Sniegowski, J. R. Murray, and P. J. McWhorter, "Embedded micromechanical devices for the monolithic integration of MEMS with CMOS," presented at International Electron Devices Meeting, 1995.

[4] M. Schneider, R. Castagnetti, M. G. Allen, and H. Baltes, "Integrated flux concentrator improves CMOS magnetotransistors," presented at IEEE International Conference on Micro Electro Mechanical Systems (MEMS), Amsterdam, Netherlands, 1995.

[5] X. Q. Wang, X. Yang, K. Walsh, and Y.-C. Tai, "Gas-phase silicon etching with bromine trifluoride," presented at International Conference on Solid-State Sensors and Actuators (Transducer), Chicago, IL, USA, 1997.

[6] "Parylene data sheet," Specialty Coating System, Indianapolis.

[7] X. Q. Wang, "Integrated Parylene micro electro mechanical systems," Ph. D. thesis, California Institute of Technology 2000

[8] X. Q. Wang, Z. Han, F. Jiang, T. Tsao, Q. Lin, Y. C. Tai, and C. M. Ho, "A fully Integrated Shear Stress Sensor," presented at International Conference on Solid-State Sensors and Actuators (Transducer), 1999.

[9] http://www.mitelsemi.com

Chapter 5

Future Applications of MEMS Skin Technology

In my Ph.D. research, the MEMS skin technology was mainly used for the fluid dynamic monitoring/diagnostics applications. As a generic method to fabricate MEMS devices on flexible substrates, the smart skin technology can also enable many other applications. With the demonstrated capability of being integrated with ICs, much more complicated functionality can be realized. The promising applications are listed below.

Biomedical applications

MEMS is particularly beneficial for a great deal of biomedical applications because it lends itself very naturally to the fabrication of miniaturized sensors, actuators and other microstructures. With the MEMS skin technology, we are provided with another level of functionality. As shown in the Figure 5.1, the sensor skin can be attached to human body like a Band-Aid^{TM}. Examples of future applications include sensor skins with sensors capable of monitoring physiological parameters, such as glucose and insulin levels. For implantable applications, sensors can be built on flexible substrates to conform to the organ shape or to minimize tissue trauma during patient movement. MEMS skins incorporate arrays of tactile, temperature, and other sensors are

very helpful to surgical instruments for minimally invasive surgery. As we can imagine, the IC-integrated sensor skin would also be of great interest for research in prosthetics, ergonomics.

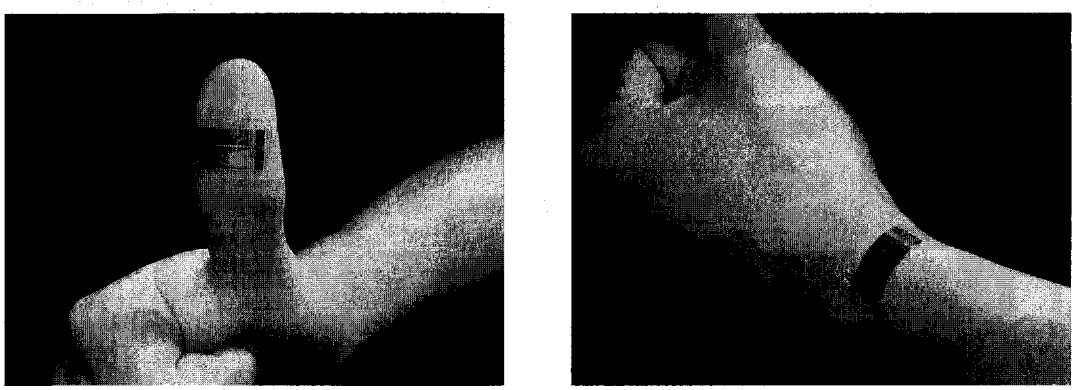

Figure 5.1 Pictures illustrating the concept of attaching sensor skins to human body like a Band-Aid™.

Wearable microsystems

It will open up a whole new domain of applications if we can take our electronics and roll and crumple them up. For example, DARPA recently started a wearable computer initiative based on e-textiles [1]. The goal is to develop technologies that will enable the economic fabrication of large-area, flexible, conformable electronic systems in a way similar to weaving textiles. With e-textiles, we can develop novel applications such as an intelligent fabric (uniform) worn by the Land Warrior that would perform health monitoring, mission communications, mission monitoring, and weight distribution as shown in Figure 5.2 [1].

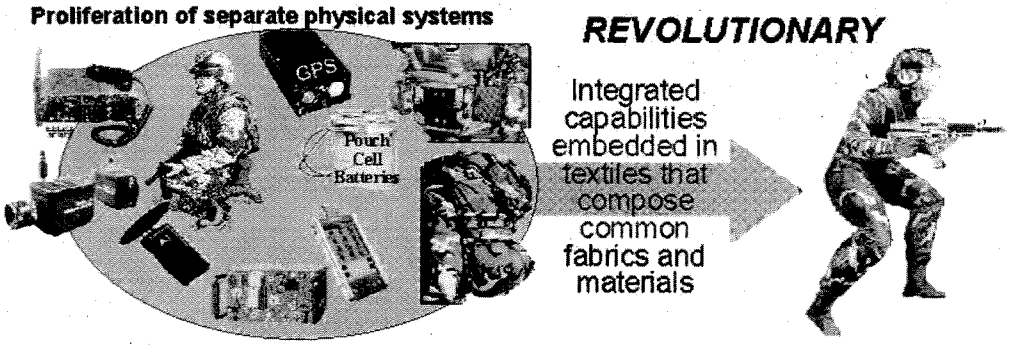

Figure 5.2 The concept of an intelligent uniform could be worn by the Land Warrior [1]

While the silicon-based flexible skin technology is not suitable for large-area systems, it is advantageous for the high-end, small-area wearable systems. As mentioned previously, the most important advantage of our technology is its compatibility with the current IC and MEMS fabrication technology. Therefore, tremendous investment and development time can be saved by leveraging the IC and MEMS fabrication technologies. Applications include wearable gadgets with sensors that can detect toxic gases or biological agents for antibioterrorism or military purpose. Many wearable consumer products can also be developed based on the MEMS skin technology. To make practical wearable systems, key issues such as data transmission and power sources need to be addressed. One solution I envision now is to develop a hybrid approach that combines the e-textiles and our MEMS skins. The MEMS skins can provide ICs (even CPUs) and sensors, while the e-textiles will provide the power source and the platform for data transmission. It is very interesting to note that the technologies of e-textiles and the MEMS skin technology are complementary and the combination will bring the advantages of both technologies.

RF applications

Conformal antenna arrays mounted on nonplanar surfaces are attractive for certain applications requiring wide-angle coverage. With our technology, which can be used to fabricate skins from MMIC wafers, not only the antenna arrays, but also other RF circuits can be integrated together. Therefore, it will be a totally integrated flexible RF system. The dielectric loss of the RF components can be alleviated by removing the underneath substrate. This can be conveniently done, since removal of substrate from backside is an integral step during skin fabrication. MEMS RF devices such as MEMS switches, MEMS resonators can also be incorporated.

Robotics

Sensors that measure elements such as touch, position, image, temperature, pressure, chemical presence, and so on, are crucial for robots to interact with the environment. Smart skins incorporating all kinds of sensors and the control electronics (even CPU) can ultimately lead to the authentic intelligent robots.

Package

Packaging is a key issue for both MEMS and ICs. The MEMS skin is essentially a packaging technology. Novel packaging method like folded packaging, which can save a significant amount of space and is very beneficial for further miniaturization of portable devices, can be realized as shown in Figure 5.3.

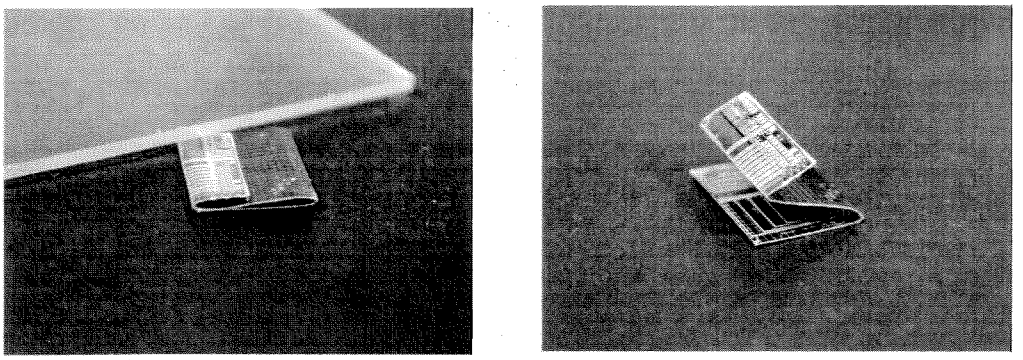

Figure 5.3 Folded packaging based on MEMS skin technology.

In conclusion, the MEMS skin technology will enable many important applications far beyond what we have already demonstrated.

References

[1] http://www.darpa.mil/ipto/research/e-textile/background.html.

Appendix

The Normalization of Shear-Stress Sensors

As mentioned in Chapter 1, the relationship between shear stress τ and the input power P to the sensor is typically described by:

$$P = \frac{V^2}{R_S} = \Delta T(A_t(\rho\tau)^{1/n} + B_t), \quad (1)$$

where V and R_S are respectively the voltage and resistance of shear-stress sensor, ΔT is the average temperature difference between the heated resistor and ambient, A_t and B_t are coefficients determined by geometry and thermal parameters. There are many factors which affect the sensor's sensitivity as shown in Eq. (1). However, it is reasonable to assume that the thermal characteristics of the diaphragm material (e.g., silicon nitride) and the ambient fluid are identical for all sensors. Then A_t and B_t are only determined by the diaphragm dimensions. Usually, good uniformity of the diaphragm dimension can be achieved for the sensors on the same chip. Therefore, we can assume that A_t and B_t are constants and the variables are the sensing element resistance R_S. and temperature difference ΔT.

Let's first examine the CT mode, where ΔT is constant when shear stress varies. We use V_0 to represent the output voltage when the shear stress is zero and ΔV the output voltage change at a nonzero shear stress. Substituting $V = V_0 + \Delta V$ into Eq. (1) and neglecting the second order term $(\Delta V)^2$ (assuming $\Delta V/V_0 << 1$), we have

$$\frac{V_0^2 + 2\Delta V V_0}{R_S} = \Delta T A_t(\rho\tau)^{1/n} + \Delta T B_t \quad (2)$$

At zero shear stress, we have

$$V_0^2 / R_S = \Delta T B_t \tag{3}$$

Substituting Eq. (3) into Eq. (2), we obtain

$$\frac{2\Delta V V_0}{R_S} = \Delta T A_t (\rho\tau)^{1/n} \tag{4}$$

Multiplying both sides of Eq. (4) by V_0, and using Eq. (3) again, we finally have

$$\frac{\Delta V}{V_0} = \frac{A_t}{2B_t} (\rho\tau)^{1/n} \tag{5}$$

Eq. (5) clearly states that $\Delta V/V_0$ is same for all sensors with different resistances and different over-heat ratios when they experience same shear stress. Through similar process, we can prove that $\Delta V/V_0$ works for CC mode as well when sensors have same over-heat ratios.